UNIVERSITY OF CALIFORNIA, MERCED

Active Colloidal Self-Assembly With Optical Binding Forces

A dissertation submitted in partial satisfaction of the
requirements for the degree
Doctor of Philosophy

in

Physics

by

Dominique Davenport

Committee in charge:

Professor Linda Hirst, Chair
Assistant Professor Dustin Kleckner
Professor Arnold Kim

2022

The dissertation of Dominique Davenport is approved, and it is acceptable in quality and form for publication on microfilm and electronically:

(Assistant Professor Dustin Kleckner)

(Professor Arnold Kim)

(Professor Linda Hirst, Chair)

University of California, Merced

2022

DEDICATION

To my wife and parents.

TABLE OF CONTENTS

LIST OF FIGURES

ACKNOWLEDGEMENTS

There are many people to acknowledge who have provided contributions to the work presented in this thesis. The concept of the initial experimental designs for studying optical binding was developed by my advisor Dustin Kleckner. At the beginning of the project, I was joined with Julian Cuevas who helped with the original damage testing of various optical components in the experiment. The rest of the Kleckner Lab group provided many discussions which aided in troubleshooting the majority of research hurdles. Specifically, I would like to acknowledge the work of Nicholas St. Clair, whose computational study on acoustic binding guided how we approached and understood optical binding. To that end, I also acknowledge Arnold D. Kim for the development of the computational code used in acoustic binding. In the development of computational methods for my project, I would like to thank Kinjal Dasbiswas and Daniel Beller for the discussions regarding molecular dynamics simulations. Finally, I would like to acknowledge my committee chair, Linda Hirst for giving me new ways to think about active matter systems.

VITA

2014	B. S. in Physics, California State University Stanislaus, Turlock
2016-2020	Graduate Teaching Assistant, University of California, Merced
2022	Ph. D. in Physics, University of California, Merced

PUBLICATIONS

Dominique Davenport, Dustin Kleckner, "Formation of Colloidal Chains and Driven Clusters with Optical Binding", *Soft Matter*, 18, 2022.

Nicholas St. Clair, Dominique Davenport, Arnold Kim, Dustin Kleckner "Dynamics of Acoustically Bound Particles", *ArXiv*, 2022.

HONORS AND AWARDS

NSF Alliance for Graduate Education and the Professoriate (AGEP) Fellow, UC Merced, 2019

NSF Interdisciplinary Computational Graduate Education (ICGE), UC Merced, 2018

STEM Teacher and Researcher (STAR) Fellow, Cal-Poly, 2014

McNair Scholar, UC Merced, 2012

Dean's Award for Academic Excellence in Physics, CSU Stanislaus

ABSTRACT OF THE DISSERTATION

Active Colloidal Self-Assembly With Optical Binding Forces

by

Dominique Davenport

Doctor of Philosophy in Physics

University of California Merced, 2022

Assistant Professor Dustin Kleckner

The motivation of this dissertation was to develop methods to analyze optical binding as a self-organization tool for colloidal matter. Since the initial experimental validation of optical binding achieved by [1], the application of interest was to eventually realize the self-organization of many-particle systems using light. The original findings by Burns, Fournier and Golovchenko, which were inspired by the experimental work of [2] on optical forces and theoretical work of [3] on intermolecular radiation forces, illustrated unique features of optical binding. One major finding was that the interaction featured multiple stable points between two interacting dielectric spheres. The second finding was that the stable displacements corresponded to the wavelength of the applied field [1]. With these two features, a new force was introduced which could be applied externally to colloidal systems. This interaction could be tuned to set the strength and inter-particle distances. The current work presented is an extension of this primary work onto many-body systems. Specifically, we aimed to provide a pathway towards determining how one might practically design self-organization behaviors using optical binding forces.

There have been numerous studies in the past focused on using optical binding for the self-organization of multiple particles. Partially because of its wide applicability and high specificity, it remains difficult to piece together a coherent link between the various optical binding experiments achieved in the past. For

example, it is common to describe distinct optical binding setups based on relative particle size, orientation of the beam axis, beam-type, and damping conditions of the surrounding medium to name a few. In some cases, experiments have described vast differences in behaviors by subtle changes in particle size [4, 5]. Likewise, in this dissertation, I describe how subtle changes in relative refractive index can also strongly alter the behavior in optically bound systems. While these examples illustrate tunability, which is generally ideal for designing self-organized systems, the non-linearity of optical binding makes it extremely difficult to predict.

Some of the primary behaviors that are addressed in this dissertation include: non-conservative, non-pairwise, and non-reciprocal interactions and how they interface with the stability and activity of the system. Non-conservative forces are generally present in optical forces [6]. It is common even to separate the conservative gradient and non-conservative scattering force in the discussion of optically induced forces. In application, optical tweezers and optical traps in fact utilize a fine tuned balance of these two forces [2]. Because optical binding is ultimately a second-order effect derived from these optical forces, non-conservative optical binding is expected. However, because optical scattering and absorption is dependent on polarizability, a complex variable which is tied to a number of physical properties of the material, the field, and the surrounding medium [7], the strength and relevance of non-conservative effects can range. For instance, conservative gradient forces dominate for particles that are relatively small compared to the field wavelength. In this dissertation, I discuss these effects with respect to the complex part of the polarizability. For application of optical binding on large colloidal systems, non-conservative forces are important. [8] showed, for instance, that the strong presence of non-conservative forces can play a role in stability of large optically bound systems. This is an extremely important detail because if the goal is to generate a large ordered structure, you would not want the emergence of instabilities. On the other-hand, instabilities could be desirable if you are indeed interested in active material properties. In either case, it would be beneficial to know exactly when non-conservative forces will disrupt stability.

Less studied are the presence non-pairwise forces in optical binding systems.

Non-pairwise forces in this system can ultimately arise from multiple scattering effects. While multiple scattering and non-pairwise interactions are not new to discussions of optical scattering, they are usually discussed at the molecular sub-particle scale [7]. In this dissertation work, I discuss the potential effect of N-body forces between particles in close proximity. In the past, these effects have been generally ignored. For small particles, it is found that non-pairwise forces are negligible [9]. There aren't however clear guidelines for when this remains true for larger particles. In this dissertation, I present numerical approaches which help us discern the strength of non-pairwise contributions for a number of configurations. We studied for instance the dependence on particle size along with alternative parameters such as relative refractive index and orientation. Furthermore, I present experimental evidence of collective action.

Finally, I address the presence of non-reciprocity in optical binding. Non-reciprocal interactions are closely related to non-conservative interactions but are more specific to multiple species in which one species exerts a force on another without experiencing the equal and opposite effect. We have yet to observe optical binding experiments which include multiple species of scatterers; however, we do explore the presence of non-reciprocal forces in single species systems. I address these non-reciprocal forces with numerical approaches. The numerical studies are inspired by our experimental work which shows the formation of small semi-stable clusters from a system of identical spheres. In other words, we found an emergence of a two-species system from a single species system. More so, the findings strongly suggest that the interactions can be non-reciprocal. These results and their implications are discussed in Chapter 2.

As much as this dissertation attempts to answer about optical binding, it is also a description of new approaches of studying optical binding itself. Generating self-organization with optical binding can require extremely strong optical fields [1]. Even more difficult is the integration of imaging optics which can accommodate a high powered laser. For the reader, I include the experimental techniques that worked best along with a few alternative methods. The hope is that these methods provide an easier pathway towards the study of optical binding or other light-

matter phenomena. For instance, in Chapter 2 you will find the description of a custom built microscope system which allowed us to capture 3-dimensional images of a sample subjected to a high powered laser source while I also describe an entirely alternative system which geometry offers more control of the field propagation angle.

In Chapter 3, I present our work in integrating optical binding forces into a molecular dynamics simulation framework. While various simulations of optical binding forces have been made by researchers in the past, the most relevant to this dissertation being the work in [10], our goals were guided by finding approaches which can handle a larger assortment of particles and be easily integrated to include the effects of Brownian motion and additional forces. To that end, this dissertation required the development of several scattering simulations. The first is a scattering code based mainly on the Coupled Dipole Method (CDM), also known as the Discrete Dipole Approximation (DDA) [11, 12]. While work remains to be done to increase computational speed for larger simulations, I share results of small scale simulations which include thermal fluctuations and additional interactions. Unlike Mie scattering theory methods, CDM is generally easier to extend for many particles that may be non-spherical or non-homogeneous.

The second scattering code presented briefly in this dissertation utilizes the method of fundamental solutions (MFS) to obtain scattering results. The major difference between CDM and MFS is that CDM requires that an object be approximated by scattering bodies that fill the volume whereas MFS can be used with scattering bodies that fill on the surface area saving computational cost. The computational development of this method was prepared by collaborator Arnold D. Kim. The method was developed specifically for acoustic binding, with which Nicholas St. Clair explored the dynamics of particle clusters driven by acoustic field scattering interactions. This dissertation explores those results in terms of optical fields, particularly how these systems can be approached numerically in a similar manner.

Chapter 1

Unique Properties of Optical Binding

1.1 Introduction

The story of optical forces might very well have begun with the observation of comet tails, a phenomenon which provided observable effects, shown in **Fig. 1.1**, of solar radiation pressure on dust particles [13]. It wasn't until Maxwell that the phenomenon of light-pressure was described in classical electromagnetic theory; in which he stated plainly, in *A Treatise on Electricity and Magnetism*, that in any "medium in which waves are propagated, there is a pressure in the direction normal to the waves" [14]. In the early 1900's, Nichols and Hull provided the first measurements of radiation pressure [15] . The development of the laser allowed Ashkin in 1970 to accelerate and trap dielectric microspheres [16]. Ashkin described the spheres being "simultaneously drawn in to the beam axis and accelerated in the direction of the light". While the second statement indeed fits the description for the radiation pressure force as previously described, this was the first experiment in which we observe the ability of light to act as a trapping mechanism. In later experiments, Ashkin described the new effect as an optical gradient force which "is proportional to the gradient of intensity and points in the direction of the intensity gradient" [2]. Thus, we have a description of two distinct optical forces: a force

Figure 1.1: comet gas and dust tail

which follows the intensity and direction of the light field and a force which follows the gradient of the field intensity. These two forces are most widely referred to as the optical scattering force and optical gradient force.

We have since then seen optical forces utilized in a number of applications in optics and biophysics [17, 18]. Belonging to the first wave of researchers studying optical traps using optical forces, in an attempt to trap multiple particles, Burns et. al. experimentally observed the phenomenon of optical binding [1]. By placing two micro-spheres displaced perpendicularly to the light propagation of a single laser, it was found that the two particles would interact with each other such that they tended to separate at distances corresponding to multiples of the light wavelength. The best way to understand this interaction is that scattering particles modify the light field around them; this light field then places optical forces on neighboring objects. The wavelength dependent displacements are a consequence of interference features that arise in optical scattering.

Understanding the optical binding force more generally has been an interest in the field since the original optical binding experiments. In this Chapter, I outline a few areas which we believe characterize the key aspects of the optical binding

interaction: How strong are these forces? Are they pairwise? How much can these effects be tuned? All of these characterizations are ultimately important for directing self-assembly. They can tell you when self-assembly will occur and what type of structures one can expect to find. The driving motivation of this work is to realize the design of optically bound materials.

In this chapter, I will begin with describing single-body optical forces. Primarily, the focus is on distinguishing the scattering and gradient forces. While these forces are pretty well understood in terms of optical traps for single particle systems, it is important to describe in this thesis as the differences between scattering and gradient forces manifest in a new way for multi-particle systems. The subsequent sections will cover in detail how two particles interact though optical binding forces. An analytical form of the binding force derived from a small particle approximation will be presented for two distinct geometries. The final sections of the chapter are intended to address additional phenomena which can arise for many-particle systems of strongly scattering bodies.

1.2 Optical forces

The optical binding force can be understood as a second-order optical force. Where optical forces can be applied directly to an object from an external field, optical binding forces arise from the field scattered by another object, thus requiring at least a two-particle system. Fortunately, we can use what we know about single-body optical forces and relate it to optical binding as they share the same underlying mechanisms.

Considering a single object placed in an optical field, we understand that the object can be subject to optical forces which can pushed, trapped, or rotated. Ultimately what that force *is*, can be determined by integrating Maxwell's stress tensor, $\overleftrightarrow{\boldsymbol{T}}$, given by

$$\overleftrightarrow{\boldsymbol{T}} = \epsilon_0[\boldsymbol{E}\boldsymbol{E} + c^2\boldsymbol{B}\boldsymbol{B} - \frac{1}{2}\overleftrightarrow{\boldsymbol{I}}(\boldsymbol{E}\cdot\boldsymbol{E} + c^2\boldsymbol{B}\cdot\boldsymbol{B})] \tag{1.1}$$

over the surface of the entire object:

$$\boldsymbol{F} = \oint_s \hat{\boldsymbol{n}} \cdot \langle \overleftrightarrow{\boldsymbol{T}} \rangle d\sigma \tag{1.2}$$

($\boldsymbol{E}$ is the total electric field, $\boldsymbol{B}$ is the magnetic flux density, ϵ_0 the vacuum permittivity, c the speed of light in a vacuum, and $\hat{\boldsymbol{n}}$ the vector normal to the surface) [19]. $\overleftrightarrow{\boldsymbol{T}}$ can be thought of as a representation of the flux of light momentum through the object.

The total force on an object in a field can be obtained by **Eq. 1.1** provided that we know the total field $\boldsymbol{E}$, Numerically, there are a few methods which can be used to calculate the optical forces on objects; however, the rest of the thesis will depend on total fields which involve electromagnetic scattering. For consistency it is useful to utilize a scattering code such as those developed for Mie scattering theory [7] or the Coupled Dipole Method (CDM) [20]. We utilize CDM for the rest of the discussion when numerical data is required. Because CDM is an approximation in which a single object is reduced to N dipoles, instead of using **Eq. 1.2** to compute the force, we find it is more straightforward to store force on each dipole, F_i and obtain the total force by:

$$\boldsymbol{F} = \sum_{i=1}^{N} \boldsymbol{F}_i \tag{1.3}$$

1.2.1 Optical forces from the Coupled Dipole Method

The CDM was the tool of choice that we used to compute optical binding forces. CDM is already a well studied method for optical scattering [11] It has well documented methods for computing radiation pressure forces [12] as well as previous use in computing optical binding forces [5]. This method is optimized for the study of dielectric particles of arbitrary shape. While our main focus is spheres in this work which could be handled by Mie scattering code, the freedom to study arbitrarily shaped particles is an increasingly attractive feature as researchers are pushing the boundaries on the development of non-spherical colloids [21].

CDM utilizes a finite array of polarizable points in a volume to approximate an object. Starting with the incident field and assigning each dipole a complex

polarizability, α, one can calculate the polarization at each dipole,

$$\boldsymbol{p}_0(r) = \alpha \boldsymbol{E}_{inc}(r) \tag{1.4}$$

with,

$$\boldsymbol{E}_{inc}(r) = \boldsymbol{E}_0(r) + \sum_i \overleftrightarrow{\boldsymbol{G}}_i(r, r_i) \cdot \boldsymbol{p}_i(r_i) \tag{1.5}$$

where $\boldsymbol{E}_0(r)$ is the initial external field and $\boldsymbol{E}_{inc}(r)$ is the total incident field at r. $\overleftrightarrow{\boldsymbol{G}}$ is the dyadic Green's function which can be defined by [22]:

$$\overleftrightarrow{\boldsymbol{G}} = \frac{e^{ikR}}{4\pi\epsilon_0\epsilon_m R^3}[(3 - 3ikR - k^2R^2)\frac{\boldsymbol{R} \otimes \boldsymbol{R}}{R^2} + (k^2R^2 + ikR - 1)\overleftrightarrow{\boldsymbol{I}}] \tag{1.6}$$

ϵ_0 and ϵ_m are the dielectric constants of free space and the medium respectively, k is the wave-number defined by $\frac{2\pi}{\lambda}$, $\boldsymbol{R} = \boldsymbol{r} - \boldsymbol{r}_i$, and $\overleftrightarrow{\boldsymbol{I}}$ is the identity tensor. The dot-product of $\overleftrightarrow{\boldsymbol{G}}$ with each dipole-moment, $\boldsymbol{p}_i$ returns the scattering contribution of the ith dipole. From **Eq. 1.4** and **Eq. 1.5** each subsequent polarization and and scattered field can be iteratively solved.

Once convergence is achieved, the force on each dipole is obtained from the known polarizations of each dipole and the initial external field [12]:

$$\boldsymbol{F}_i = \boldsymbol{F}_{inc,i} + \boldsymbol{F}_{scatter,i} \tag{1.7}$$

where,

$$\boldsymbol{F}_{inc,i} = \sum_i^N \frac{1}{2}\mathrm{Re}\left[i\boldsymbol{k}(\boldsymbol{p}_{i,0}^* \cdot \boldsymbol{\nabla})\boldsymbol{E}_0 e^{i\boldsymbol{k}\cdot\boldsymbol{r}_i}\right] \tag{1.8}$$

and

$$\boldsymbol{F}_{scatter,i} = \sum_i^N \sum_{j\neq i}^N \frac{1}{2}\mathrm{Re}\left[\boldsymbol{F}_{i,j}\right] \tag{1.9}$$

with,

$$\begin{aligned} F_{i,j} =& e^{ikr_{i,j}}\{[(\boldsymbol{p}_{i,0}^* \cdot \boldsymbol{p}_{j,0})\hat{\boldsymbol{n}}_{i,j} + \boldsymbol{p}_{i,0}^*(\hat{\boldsymbol{n}}_{i,j} \cdot \boldsymbol{p}_{j,0}) + (\boldsymbol{p}_{i,0}^* \cdot \hat{\boldsymbol{n}}_{i,j})\boldsymbol{p}_{j,0} - \\ & 5(\boldsymbol{p}_{i,0}^* \cdot \hat{\boldsymbol{n}}_{i,j})\hat{\boldsymbol{n}}_{i,j}(\hat{\boldsymbol{n}}_{i,j} \cdot \boldsymbol{p}_{j,0})] \times \left(-\frac{k^2}{r_{i,j}^2} - \frac{3ik}{r_{i,j}^3} + \frac{3}{r_{i,j}^4}\right) + \\ & [(\boldsymbol{p}_{i,0}^* \cdot \boldsymbol{p}_{j,0})\hat{\boldsymbol{n}}_{i,j} - (\boldsymbol{p}_{i,0}^* \cdot \hat{\boldsymbol{n}}_{i,j})\hat{\boldsymbol{n}}_{i,j}(\hat{\boldsymbol{n}}_{i,j} \cdot \boldsymbol{p}_{j,0})]\left(\frac{ik^3}{r_{i,j}} - \frac{k^2}{r_{i,j}^2}\right)\} \end{aligned} \tag{1.10}$$

$\boldsymbol{r}_{i,j}$ is the displacement between the ith and jth dipole ($\boldsymbol{r}_i - \boldsymbol{r}_j$), $r_{i,j} = |\boldsymbol{r}_{i,j}|$, $\hat{\boldsymbol{n}}_{i,j} = \boldsymbol{r}_{i,j}/r_{i,j}$. What is useful about **Eq. 1.7-Eq. 1.10** is that the force can be determined regardless of shape, size, or number of particles in the system. As long as each dipole is accounted for, the optical forces on each particle can be determined by summing the forces on the dipoles which belong to it. This method can therefore be used to describe first-order and second-order optical forces.

1.2.2 Scattering and Gradient Forces

First-order optical forces can be understood as arising from two processes, scattering from the object and polarization of the object; although these two processes are clearly connected light-matter interactions. These processes do however generate behaviors which it has become common to distinguish when describing optical forces. You'll thus find descriptions of optical scattering and optical gradient forces, although they both fall generally into radiation pressure forces. Although it's not always obvious, these forces are distinguished for good reason. The physics which describes the behavior is certainly different: gradient forces are conservative and scattering forces are not for instance. Furthermore, these forces do not scale together with physical properties of the system such as particle size. Finally, their relative contributions can be manipulated by field design. Undoubtedly, these two forces are important to describe for understanding the phenomena of optical binding.

When light is scattered by an object, the magnitude and direction of the energy flux of the light is changed [23]. Due to conservation laws, this momentum transfer must be exerted onto the the particle. For small particles, ($a \ll \lambda$) where a is the radius and λ is the wavelength of light, this momentum transfer can be represented as a force:

$$\boldsymbol{F}_{scat} = \frac{n_m}{k^2 c}\frac{8}{3}\pi(ka)^6\left(\frac{m^2-1}{m^2+2}\right)^2|E|^2\hat{\boldsymbol{k}} \tag{1.11}$$

where n_m is the refractive index of the medium, $m = n_p/n_m$ is the relative refractive index, and $\hat{\boldsymbol{k}}$ is the propagation direction of the field [23]. The wavenumber, k, multiplied by the radius, a, gives the size parameter, ka, which provides a value

which compares the size of the object relative to the wavelength of the incident field.

While **Eq. 1.11** tells us the scaling within the small-particle limit, we cannot assume that this scaling is represented in larger systems. Using the CDM method, we can both validate **Eq. 1.11** for small particles but also assess the scaling for larger objects. To do this, we need to pick an initial-field. One of the more common scenarios is that of a plane electromagnetic wave,

$$\boldsymbol{E}_{inc} = E_0 e^{i\boldsymbol{k}\cdot\boldsymbol{r}} \hat{\boldsymbol{e}}_{\boldsymbol{p}} \tag{1.12}$$

with polarization direction of $\hat{\boldsymbol{e}}_{\boldsymbol{p}}$ and wave vector $\boldsymbol{k}$. This choice is particularly useful in that the component for the scattering force will be aligned with $\boldsymbol{k}$ due to the symmetry of the field and it ensured that the gradient force will have no contribution to the force. To assess the force for different ka and m, we can simply test a separate CDM simulation and record the strength of the force in the $\boldsymbol{k}$ direction. Numerically, **Fig. 1.2** shows how the force scales in terms of both ka and m. By selecting out certain relative indices, it is clear to see in **Fig. 1.2**b that strength of the scattering force scales like $(ka)^6$ while $ka \ll 1$. This relation is expected from **Eq. 1.11**. For larger spheres, we find that the force continues to increase with size but scales with $\sim ka^{3.5}$.

The gradient force arises as the object is polarized in the field and the collective dipole moment experiences a force similar to that of the force on a point dipole,

$$\boldsymbol{F}_{dipole} = (\boldsymbol{p}\cdot\boldsymbol{\nabla})\boldsymbol{E} \tag{1.13}$$

which the dipole moment $\boldsymbol{p}$ can be written in terms of $\boldsymbol{E}$,

$$\boldsymbol{p} = \alpha\boldsymbol{E} \tag{1.14}$$

where α is the polarizability which is in general complex and will be described in more detail in the following section. Following **Eq. 1.13** and **Eq. 1.14** one can derive the gradient force for a small object [23]:

$$\boldsymbol{F}_{grad} = n_m^2 \epsilon_0 \pi a^3 \left(\frac{m^2-1}{m^2+2}\right) \boldsymbol{\nabla}|E|^2 \tag{1.15}$$

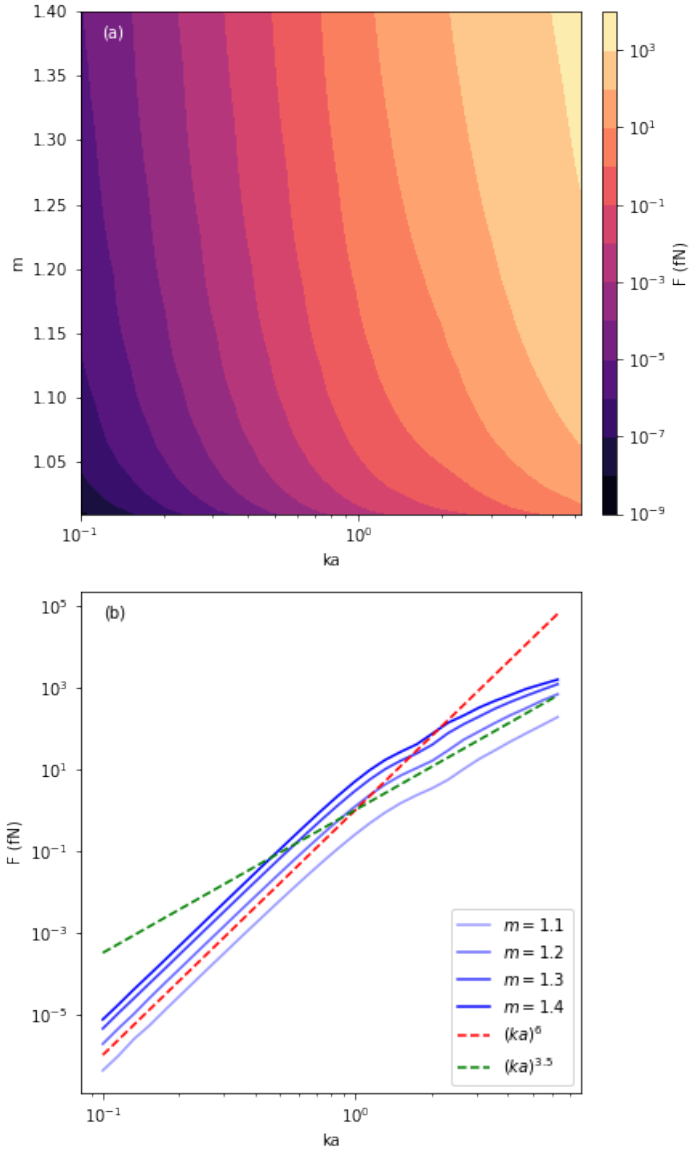

Figure 1.2: **(a)** Strength of the scattering force for a particle of size ka and relative index m. A particle is placed in plane-wave of wavelength 400nm and a field intensity of 1 mW/μm^2. **(b)** selected lines from **(a)** are plotted to illustrate the force scales with ka. **(c)** A higher resolution analysis for $ka > 1$ values.

which, as expected, depends on the gradient of the field intensity. I also note that the gradient force scales differently than the scattering force with ka and m. **Eq. 1.15** is of course another small particle approximation. To study this force numerically, we place a single particle in a standing wave at a node and compute the radiation forces that it experiences towards the plane of highest intensity. In this case, the scattering forces should be negligible as the standing wave is formed by two counter-propagating plane-waves which should cancel out first-order scattering forces. From this simulation we generate **Fig. 1.3** which provides us way to understand how the gradient force scales with respect to the particle parameters. From **Fig. 1.3**b, we can see that the gradient force scales like $(ka)^3$ for $ka \ll 1$ particles. Beyond small particles, we find that the strength of the gradient force ceases to follow a $(ka)^3$ trend. What is not shown in **Fig. 1.3**b because the absolute value of the force is plotted on a log-scale is that the force oscillates between positive and negative values depending on ka. Even though the force is no longer shares a linear relationship with $(ka)^3$ for larger particles, we observe that the average strength has a general trend which follows $\sim (ka)^2$ (**Fig. 1.3**c).

1.2.3 Complex Polarizability

In general, particles will have a polarizability which is complex. Understanding the role polarizability has on the scattering and gradient forces can help guide the understanding of why these forces scale the way they do. This section is dedicated to describing how the complex polarizability plays a role in scattering strength. The complex polarizability suggests a phase shift between the incident field and the field propagating through the scattering object. It is this shift which gives rise to strong scattering and thus scattering forces which become dominate in certain size regimes.

The complex polarizability can be written as:

$$\alpha = \frac{\alpha_0}{1 - \frac{ik^3\alpha_0}{6\pi\epsilon_0\epsilon_m}} \tag{1.16}$$

with

$$\alpha_0 = 4\pi\epsilon_0\epsilon_m a^3 \left(\frac{\epsilon_p - \epsilon_m}{\epsilon_p + 2\epsilon_m}\right) \tag{1.17}$$

an expansion of **Eq. 1.16** yields:

$$\alpha = \alpha_0 + i\frac{k^3}{6\pi\epsilon_0\epsilon_p}\alpha_0^2 + \mathcal{O}(\alpha_0^3) \tag{1.18}$$

For small particles, α_0 is small and therefore we can consider the first two terms. A slight variation to **Eq. 1.13** is to accommodate the complex contributions by writing the forces as

$$\boldsymbol{F} = \frac{1}{2}\mathrm{Re}\left[\alpha^* \boldsymbol{E}^* \boldsymbol{\nabla} \boldsymbol{E}\right] \tag{1.19}$$

for a complex field $\boldsymbol{E} = \mathrm{Re}\left[\boldsymbol{E}\right] + i\mathrm{Im}\left[\boldsymbol{E}\right]$ and complex polarizability $\alpha = \mathrm{Re}\left[\alpha\right] + i\mathrm{Im}\left[\alpha\right]$. The real terms can be factored out which include:

$$\begin{aligned}\mathrm{Re}\left[\alpha^* \boldsymbol{E}^* \boldsymbol{\nabla} \boldsymbol{E}\right] =& \mathrm{Re}\left[\alpha\right]\left(\mathrm{Re}\left[\boldsymbol{E}\right] \cdot \boldsymbol{\nabla}\mathrm{Re}\left[\boldsymbol{E}\right] + \mathrm{Re}\left[\boldsymbol{E}\right] \cdot \boldsymbol{\nabla}\mathrm{Re}\left[\boldsymbol{E}\right]\right) - \\ & \mathrm{Im}\left[\alpha\right]\left(\mathrm{Im}\left[\boldsymbol{E}\right] \cdot \boldsymbol{\nabla}\mathrm{Re}\left[\boldsymbol{E}\right] + \mathrm{Re}\left[\boldsymbol{E}\right] \cdot \boldsymbol{\nabla}\mathrm{Im}\left[\boldsymbol{E}\right]\right)\end{aligned} \tag{1.20}$$

By utilizing the dot product rule, the first two terms return the gradient force (**Eq. 1.15**). The other contributions lead to the scattering force. One simple way to observe this is to consider a plane-wave traveling in direction $\hat{\boldsymbol{z}}$. The static plane-wave can be represented as,

$$\boldsymbol{E} = E_0 e^{ikz} \hat{\boldsymbol{e_p}} \tag{1.21}$$

$$= E_0\left[\cos\left(kz\right) + i\sin\left(kz\right)\right]\hat{\boldsymbol{e_p}} \tag{1.22}$$

Therefore,

$$\boldsymbol{\nabla}\boldsymbol{E} = kE_0\left[-\sin\left(kz\right) + i\cos\left(kz\right)\right]\hat{\boldsymbol{z}} \tag{1.23}$$

and the last two terms in **Eq. 1.20** can be rewritten as

$$\mathrm{Im}\left[\alpha\right]\left(\mathrm{Im}\left[\boldsymbol{E}\right] \cdot \boldsymbol{\nabla}\mathrm{Re}\left[\boldsymbol{E}\right] + \mathrm{Re}\left[\boldsymbol{E}\right] \cdot \boldsymbol{\nabla}\mathrm{Im}\left[\boldsymbol{E}\right]\right) = k\mathrm{Im}\left[\alpha\right]|E|^2\hat{\boldsymbol{z}} \tag{1.24}$$

and finally obtaining **Eq. 1.11** by plugging in the imaginary part of α.

We can observe that the relative strength of the real and imaginary parts of α thus control the relative strength of the scattering and gradient forces. In **Fig. 1.4**, we show how the the real and imaginary parts of α depend on the size-parameter

and the relative refractive index. We find that beyond $ka = 1$ that the imaginary part of α can eventually becomes greater than the real part of α. Where exactly this happens depends on the relative refractive index of the particles.

In the application of optical traps, particles are readily able to be trapped regardless of the relative strengths of these two forces. This is because the gradient forces can be enhanced, through focusing, well beyond the relatively subtle differences caused by increased scattering strength. One surprising result that is found with optical traps is that small and large particles despite existing in different regimes show similar behaviors. For larger particles, geometric ray tracing can be used to describe how light, focused behind the center of mass of the particle to produce a trapping force which combats the forward scattering forces. This however should not be assumed to remain true for all optical forces. In particular, for optical binding forces the gradient and scattering contributions are determined by the scattering of the particle itself. This means that the gradient component of the binding force cannot simply be enhanced by means of focusing strength and consequently might compete with the scattering force component for larger particles. Furthermore, with increased scattering, which is related to $\mathrm{Im}\,[\alpha]$ we might as well consider how multiple-scattering effects become more prevalent. Unfortunately, this cannot be done analytically. I provide analysis of multiple-scattering with respect to α in a later chapter which includes simulations of multiple objects.

The scattering force and the gradient force scale differently. Primarily, we find that the scattering force increases as ka^6 while the gradient force increases as ka^3 when $ka \ll 1$. These relationships can of course be related to α. By rewriting **Eq. 1.17** as:

$$\alpha_0 = 4\pi\epsilon_0 a^3 \left(\frac{m^2-1}{m^2+2}\right) \tag{1.25}$$

we should also expect the scattering and gradient forces to scale differently with respect to m. By expanding $\left(\frac{m^2-1}{m^2+2}\right)$ about $m = 1$:

$$\left(\frac{m^2-1}{m^2+2}\right) \approx \frac{2}{3}(m-1) \tag{1.26}$$

we see that the real part of alpha should thus cause the gradient force to scale with $(m-1)$ while the imaginary part should cause the scattering force to scale with

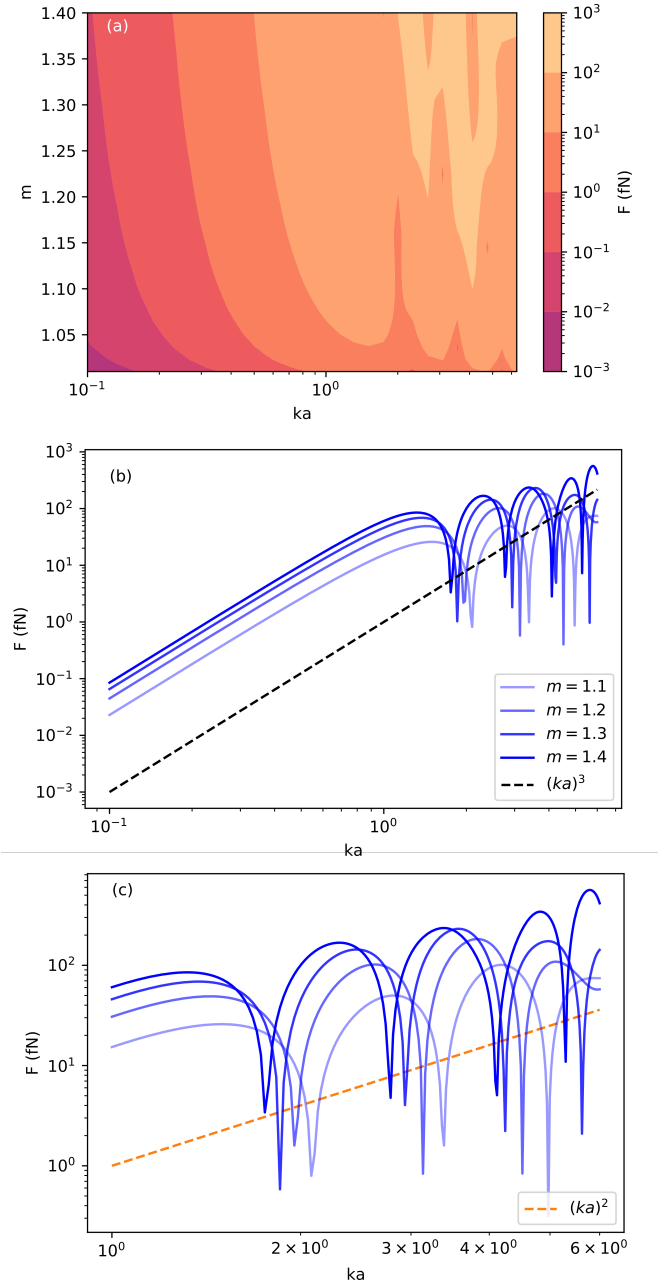

Figure 1.3: **(a-c)** Strength of the gradient force for a particle of size ka and relative index m. Here, a 1 mW/μm^2 $\lambda = 400$ nm is used. A single particle is placed at a node of a standing wave and the force applied on the particle towards the plane of highest intensity is recorded. **(b)** Gradient force scaling for select relative refractive indices for a wide range of size parameters. **(c)** Gradient force scaling for select relative refractive indices for a range of size parameters to provide more detail on the high-frequency region of **(b)**.

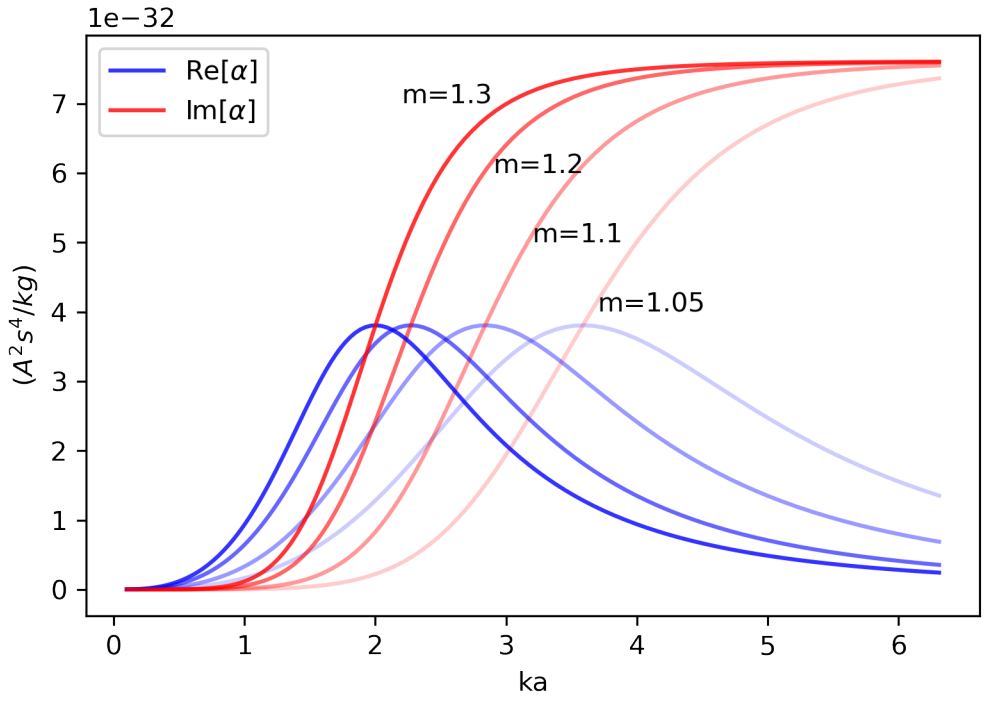

Figure 1.4: The real and imaginary parts of the complex polarizability for a range of ka.

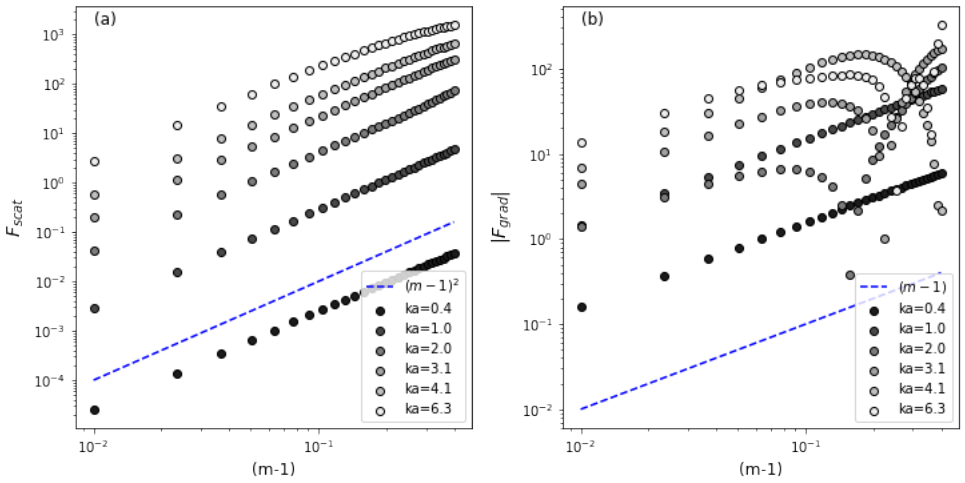

Figure 1.5: Force scaling with respect to relative refractive index for **(a)** scattering and **(b)** gradient forces. **(a)** A single sphere of size-parameter ka is placed into a $\lambda = 400$ nm, $I = 1$ mW/μm^2 single propagating plane-wave. The force in the direction of field propagation is measured and scaled relative to $(m-1)$ **(b)** A single sphere of size-parameter ka is placed into a node of a $\lambda = 400$ nm, $I = 1$ mW/μm^2 standing wave. The force in the direction towards the plane of intensity is measured.

$(m-1)^2$.

We use **Fig. 1.5**a to show that the scattering force indeed scales proportionally with $(m-1)^2$. This relationship remains true even for particle sizes $ka > 1$. For the gradient force, **Fig. 1.5**b shows a proportional scaling with $(m-1)$; however, there are strong deviations when both m and ka are large. For the gradient force, we also observe sign changes in the force, thus we've plotted only absolute value of the force on the log-scale plot.

1.3 Two-Body Optical Forces

In two-body systems, the relative positions of the two bodies can be coupled to each other. This can be understood by considering first that the optical scattering and gradient forces depend on the total field, $\boldsymbol{E}$, from the previous section and that each body contributes to $\boldsymbol{E}$ via light scattering. The same reasoning holds for many-particle systems, however the discussion for now is limited to two for

simplicity. The optical binding forces are thus proportional to how strongly the other body scatters light. In very strong scattering cases, one can imagine higher-order effects such as multiple scattering. Here, the scattered field from each object is non-negligibly re-scattered by the other at a strength that considerably alters the total field experienced by each. It remains unclear, without computing numerically, when strong multiple scattering effects are expected to be relevant.

Optical binding is a highly directional force depending heavily on the propagation vectors of the incoming light. It is thus common to consider two geometries: one in which particles are displaced perpendicularly to the axis of propagation (lateral binding) and one in which particles are displaced along the axis of propagation (longitudinal binding).

1.3.1 Lateral binding

For small particles ($ka \ll 1$) we can develop an analytical term for the optical binding force between two particles displaced perpendicularly to the field propagation. We consider a counter-propagating field along the z-axis,

$$\boldsymbol{E}_{inc} = E_0 e^{ikz}\hat{\boldsymbol{x}} + E_0 e^{-ikz}\hat{\boldsymbol{y}} \tag{1.27}$$

where $k = 2\pi/\lambda$ and two particles displaced by $\boldsymbol{R} = [Rx, 0, 0]$ in the xy-plane. Using **Eq. 1.13** and **Eq. 1.14**, we can write down a force for each of the two particles:

$$\boldsymbol{F} = \frac{1}{2}\mathrm{Re}\left[(\alpha^* \boldsymbol{E}^* \cdot \boldsymbol{\nabla})\, \boldsymbol{E}\right] \tag{1.28}$$

where α is the complex polarizability of the particles and $\boldsymbol{E}$ can be written as the sum of the incident field and the scattered field from the neighboring particle [22]:

$$\boldsymbol{E} = \overleftrightarrow{\boldsymbol{K}} \cdot \left(\boldsymbol{E}_{inc} + \overleftrightarrow{\boldsymbol{G}} \cdot \alpha \boldsymbol{E}_{inc}\right) \tag{1.29}$$

with the dyadic Green's function,

$$\overleftrightarrow{\boldsymbol{G}} = \frac{e^{ikR}}{4\pi\epsilon_0\epsilon_m R^3}[(3 - 3ikR - k^2R^2)\frac{\boldsymbol{R}\otimes\boldsymbol{R}}{R^2} + (k^2R^2 + ikR - 1)\overleftrightarrow{\boldsymbol{I}}] \tag{1.30}$$

The tensor $\overleftrightarrow{\boldsymbol{K}}$ is a term which includes multiple scattering between the two bodies and is related to the dyadic Green's function as $\overleftrightarrow{\boldsymbol{K}} = [\overleftrightarrow{\boldsymbol{I}} - \alpha^2 \overleftrightarrow{\boldsymbol{G}} \cdot \overleftrightarrow{\boldsymbol{G}}]^{-1}$. For the specified orientation:

$$G_{xx} = \frac{e^{ikR_x}}{2\pi\epsilon_0\epsilon_m}\left(\frac{1}{R_x^3} - \frac{ik}{R_x^2}\right) \tag{1.31}$$

$$G_{yy} = G_{zz} = \frac{e^{ikR_x}}{2\pi\epsilon_0\epsilon_m}\left(\frac{k^2}{R_x} + \frac{ik}{R_x^2} - \frac{1}{R_x^3}\right) \tag{1.32}$$

$K_{ii} = [1 - \alpha^2 G_{ii}^2]^{-1} \sim 1$, and $\boldsymbol{E} = [(E_0 + G_{xx}\alpha E_0), E_0+, 0]$.

Using **Eq. 1.28**, we can determine the binding force along the axis of particle separation:

$$\boldsymbol{F}_x = \frac{1}{2}\mathrm{Re}\left[\alpha^* E_i^* \boldsymbol{\nabla}_{\boldsymbol{x}} E_i + \alpha^* G_{ii} \alpha^* E_i^* \boldsymbol{\nabla}_{\boldsymbol{x}} E_i + \alpha^* E_i^* \boldsymbol{\nabla}_{\boldsymbol{x}} (G_{ii}) \alpha E_i\right] \tag{1.33}$$

with the last term being the only non-zero contribution:

$$\boldsymbol{F}_x = \frac{|\alpha|^2 |E_0|^2}{8\pi\epsilon_0\epsilon_m}\left(-\frac{k^3 \sin(kR_x)}{R_x} + \frac{2k^2\cos(kR_x)}{R_x^2} - \frac{9k\sin(kR_x)}{R_x^3} - \frac{3\cos(kR_x)}{R_x^4}\right) \tag{1.34}$$

In general, the optical binding force can include long-range oscillatory components that fall off as $1/R$. Furthermore, since α is small for nanoparticles, we ignore terms that include $\alpha^{(n>2)}$ dependence. I also note that the multiple scattering term, $K_{xx} \sim 1$ for nanoparticles and it is generally acceptable to treat it as exactly 1 within the nanoparticle limit.

Numerically, this problem can be treated without making such approximations for larger particles utilizing CDM. We can place two particles in a simulated field and measure the force on each particle due to the initial field and subsequent scattering. For reference, we include the field around a single particle placed at the origin (**Fig. 1.6**a-c). We compare this directly to the optical forces that a second particle placed within the region experiences in the simulation (**Fig. 1.6**d-f). The data is presented for particles of relative index $m = 1.2$ which is representative of polystyrene spheres in water. We also present the force-maps for three sizes ($ka = 1.0, 2.5, 4.0$). In this geometry, we show that the oscillatory form of the force is largely similar for all sizes except for the strength. We clearly show that the force is much larger for larger spheres which is not surprising considering

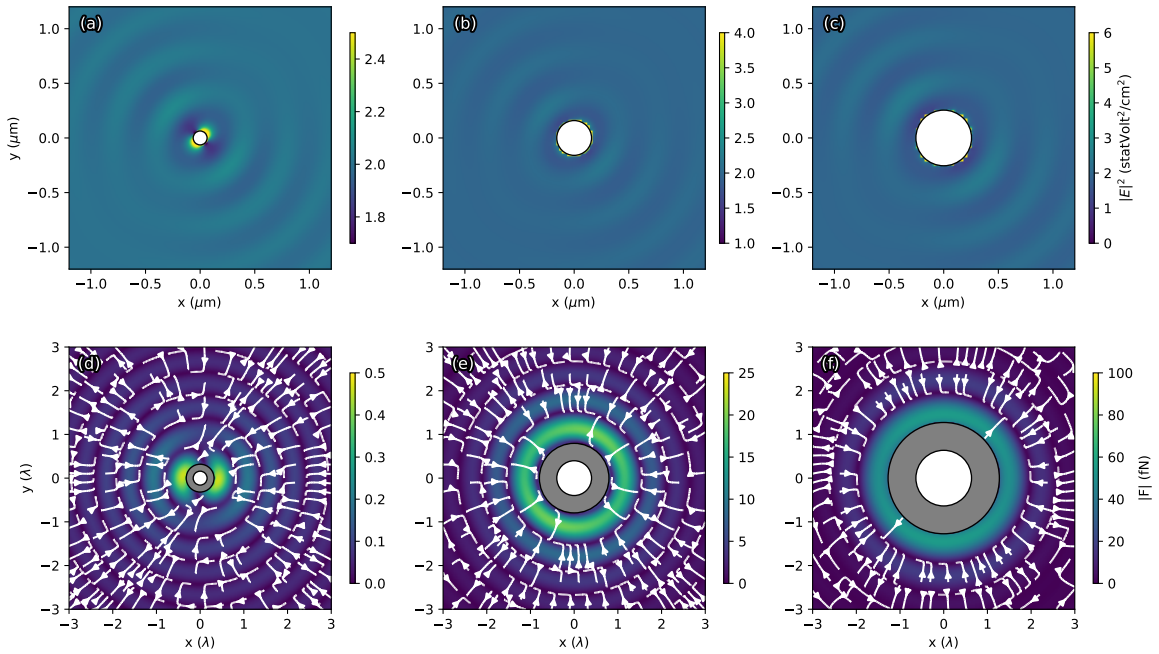

Figure 1.6: The field intensity surrounding a **(a)** $ka = 1$, **(b)** $ka = 2.5$, and **(c)** $ka = 4$ particle. The two-body force experienced by **(d)** $ka = 1$, **(e)** $ka = 2.5$, and **(f)** $ka = 4$ particles. All maps are shown in the xy-plane with a cross-polarized counter-propagating beam propagating along the z-axis.

the a^3 and a^6 dependence found for the gradient and scattering forces respectively. I also note the oscillatory nature of the force can be predicted by considering the gradient of the fields provided in **Fig. 1.5**a-c.

1.3.2 Longitudinal binding

Using a similar approach taken above, we can consider two small particles displaced along the beam propagation ($\boldsymbol{R}_1 = [0, 0, Rz]$ and $\boldsymbol{R}_2 = [0, 0, 0]$). In this case, we obtain:

$$G_{xx} = G_{yy} = \frac{e^{ikR_z}}{2\pi\epsilon_0\epsilon_m}\left(\frac{k^2}{R_z} + \frac{ik}{R_z^2} - \frac{1}{R_z^3}\right) \tag{1.35}$$

$\boldsymbol{E}_{inc,1} = [E_0 e^{ikR_z}, E_0 e^{-ikR_z}, 0]$ and $\boldsymbol{E}_{inc,2} = [E_0, E_0, 0]$. Note that it is important here that each particle is experiencing a different incident field, unlike the lateral case which afforded a symmetry in the z-position. For the force on particle 1 we

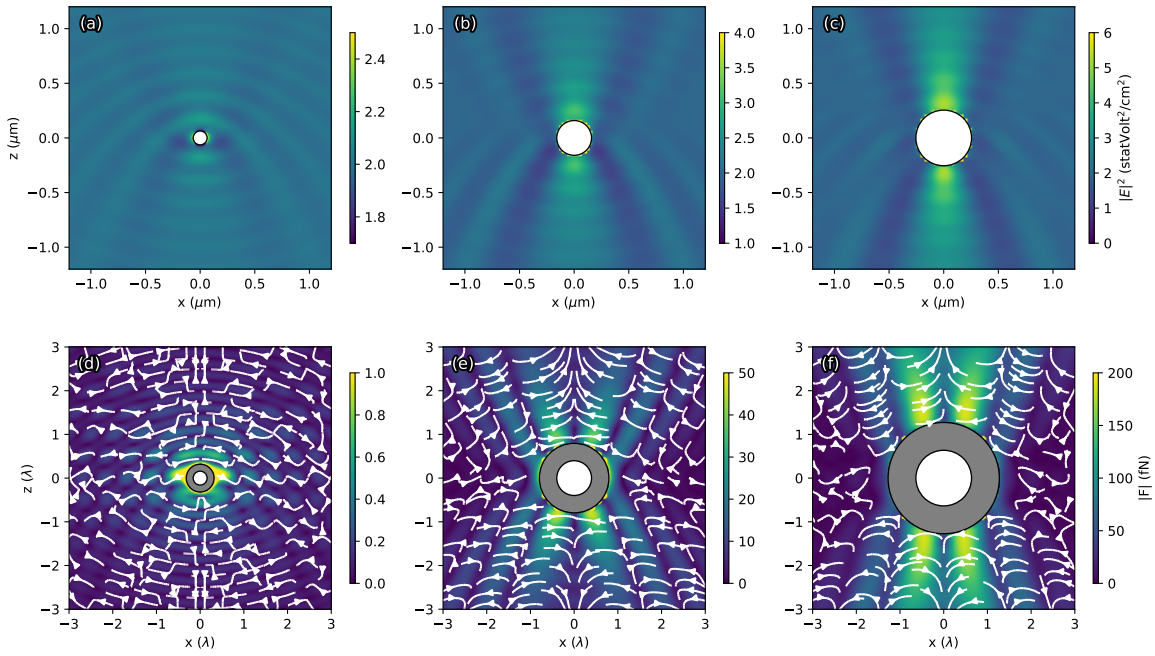

Figure 1.7: The field intensity surrounding a **(a)** $ka = 1$, **(b)** $ka = 2.5$, and **(c)** $ka = 4$ particle. The two-body force experienced by **(d)** $ka = 1$, **(e)** $ka = 2.5$, and **(f)** $ka = 4$ particles placed in a cross-polarized counter-propagating field of $\lambda = 400$ nm and $I = 1$ mW/μm^2. All maps are shown within the xz-plane with a cross-polarized counter-propagating beam propagating along the z-axis.

may utilize **Eq. 1.33** and obtain:

$$F = \frac{E_0^2}{4\pi\epsilon_0\epsilon_m}\left(-\frac{k^3|\alpha|^2\sin(2kR_z)}{R_z} + \frac{k^3(\alpha'^2 - \alpha"^2)\sin(2kR_z)}{R_z} + \frac{2k^3\alpha'\alpha"(\cos(2kR_z)+1)}{R_z}\right)$$
$$+\frac{E_0^2}{4\pi\epsilon_0\epsilon_m}\left(-\frac{2k^2|\alpha|^2\cos(2kR_z)}{R_z^2} - \frac{k^2(\alpha'^2 - \alpha"2)(\cos(2kR_z)-1)}{R_z^2} - \frac{2k^2\alpha'\alpha"\sin(2kR_z)}{R_z^2}\right) \tag{1.36}$$

Here we simplified by neglecting terms $R^{(n<-2)}$ and $\alpha^{(n>2)}$. Note the oscillatory terms which have a spatial frequency twice of the lateral binding force. We also find a term which is non-oscillatory and long-range unlike the lateral binding force. The procedures from **Eq. 1.28**-**Eq. 1.36** are only appropriate for small particles relative to the wavelength of the incident light, however we find that they describe some of the major features observed in optical binding experiments as well as other numerical methods which do not strictly utilize small particle approximations.

For a fuller picture, we again use CDM to compute the force for displacements along and off-axis from the beam propagation axis. **Fig. 1.7**a-c shows the scattered field on the xz-plane while **Fig. 1.7**d-f shows the force in the xz-plane for $ka = 1.0, 2.5, 4.0$ particles. Unlike the forces in the lateral plane, the force along the z-direction change in form for larger particles particularly along the axis of propagation. The forward scattering pattern that becomes drastically more pronounced for larger particles appears to account for these differences. The larger particles are in a sense refocusing the light field as it passes generating a trap that confines neighboring particles axially. However, an aligned particle is likely to be pushed away along the axis.

1.4 Summary

In this chapter, I introduced that optical binding forces are a combination of conservative gradient and non-conservative scattering forces. I show that the scattering forces, which dominate in longitudinal arrangements due to the propagation direction of the field, scale faster in strength than the gradient force with particle size and relative refractive index. I also show that for larger particles, the gradient

force exhibits strong and highly nonlinear response to subtle changes in the particle properties. These results that in the Mie scattering regime, optical binding forces are highly tunable. The differences between these two forces provides a complex environment. Recall that the gradient force is conservative and the scattering force is non-conservative. Tuning their relative strengths, can alter conservation properties of the system. We've shown that this tuning can be achieved by tuning ka and m.

I also highlight that optical binding forces are highly directional. In **§1.3** I provided a detailed analysis of lateral and longitudinal optical binding. This directional feature can add complexity in a self-assembled system. What is most obvious is that the lateral optical binding behaviors are similar across a large particle size range, with exception of overall strength, while particles with some degree of longitudinal displacement have strong responses to the particles relative size. This suggests that longitudinal forces are highly sensitive to size. Considering that scattering forces act strongest along the longitudinal direction and that they too have a strong sensitivity to particle size; we start to see how the roles of scattering and gradient forces will ultimately affect the interaction. Increasing the complexity even further is the fact that both laterally and longitudinally bound particles can experience multiple stable points. It is for these reasons that we consider optical binding for self-assembly; both because it is highly tunable as well as complex. In the next chapter, I discuss how we experimentally studied the self-assembly behaviors in many-body optically bound systems.

Chapter 2

Many-body Optical Binding Experiments

2.1 Introduction

Optical binding experiments date back to the work from Burns et. al. [1], where it was shown that two laterally bound dielectric spheres trapped in a beam interacted via optical binding forces. A histogram of the displacements observed over time showed a preference for displacements that were multiples of the light wavelength. This finding held clear implications for the use in organizing extended systems.

In terms of accessibility, optical binding offers an externally driven interaction. It is an interaction which can be spontaneously turned on or off along with the ability to precisely tune the strength. This would make optical binding an ideal model system to study thermodynamic phenomena such as glass-transitions. In theory, optical binding can be used to manipulate a wide range of particle sizes, including nano- and micro-scale objects. These objects are small enough to experience Brownian dynamics while large enough to be imaged and analyzed at a single-particle level. Furthermore, the length-scale which is most accessible to optical binding happens to be a scale which is relevant for optical metamaterial fabrication [24]. Photonic crystals, for instance, manipulate the propagation of

certain light wavelengths depending on the periodic spacing of material at that wavelength scale. Optical binding has already the demonstrated ability to assemble periodic lattices making it a potential tool for photonic crystal fabrication or manipulation [22]. These are our motivating concepts for which we sought to understand the possibilities and limitations of large scale optical binding systems.

In previous optical binding research, there was a number of experiments which focused on dielectric microspheres ($1 < ka < 20$) in either 2-dimensional laterally bound arrays or 1-dimensional longitudinal arrays. Each experiment a new observation of unique features of optical binding: tuning lattices by altering the light polarization [25], particles exhibiting breathing modes and center of mass motion [26], as well as the formation of particle clusters [4]. Beyond dielectric spheres, 2-dimensional lateral arrays have also been formed with Au and Ag metal nanoparticles ($ka \sim 0.6$) [27, 28].

With exception to [25] and [29], which investigate hundreds of particles, most many-body optical binding studies focus on no more than 20-particle arrays in either 1 or 2 dimensions. These limited configurations are indeed a good stepping stone into understanding what structures and behaviors can be expected from many-body optical binding. However, it remained unclear what applying a strong field to a bulk colloidal material would result in: How does stability change with system size and dimension? How much power is generally required? Do hierarchical structures form in larger systems? We found these questions most necessary to address first in a relatively simple system: identical and spherical dielectric particles in a single field. Undoubtedly, optical binding offers a number of ways to build more complexity including multiple-species systems, aspherical colloids, and multiple fields to name a few.

For optical binding, even in relatively simple systems, the experimental data remains sparse which originally might seem counter-intuitive; in theory, the requirements include a colloidal media and a coherent laser beam which are both readily available. However optical binding forces are known to be extremely weak, and thus require high intensity fields. This makes studying optical binding difficult in practice. One must consider, for example, optical damage thresholds and

constraints on imaging. One method that was utilized by Mellor et. al. [25] and Garcés-Chávez et. al. [29] to allow the observation of binding over larger areas was the utilization of evanescent waves in which the most of the beam power is restricted to near a dielectric surface. Most recently, Brzobohaty et. al. [30] presented a study of $N \sim 10000$ small dielectric spheres ($ka = .4$) in a counter-propagating beam propagating perpendicularly to the imaging path. In this study, particles were far too small to resolve details pertaining to optical binding; however the effects of the interaction can be observed in the formation of non-uniform patterns in the bulk material due to the beam.

In this chapter, I present a novel method which utilizes total internal reflection allowing for the study of hundreds of large ($ka \sim 1.6-7.1$) dielectric particles in an unconfined geometry within a high-powered optical field [31]. Within this setup, we can experimentally observe the self-assembly behavior of an assortment of colloidal particles in a counter-propagating field. Here I highlight one of the most exciting results discovered within this geometry; the formation of highly active optically bound colloidal clusters.

§2.2 will be an introduction to the design of the apparatus and techniques used to study optical binding. In **§2.3** I provide experimental results for various sizes and refractive indices. In **§2.4** I provide a detailed analysis of the behavior of the optically bound colloidal clusters.

2.2 Apparatus and experimental design

2.2.1 Estimation of power requirements

The obvious first question to ask is whether the experiment is even possible. From previous studies, we had a sense that optical powers density requirements could be quite high, but we needed to estimate exactly whether they are out of range for practical experimentation especially as we sought to scale-up the size of the experiments. There are a few measures to look into to obtain an estimate of power density requirements; however it should also be noted that, as was shown

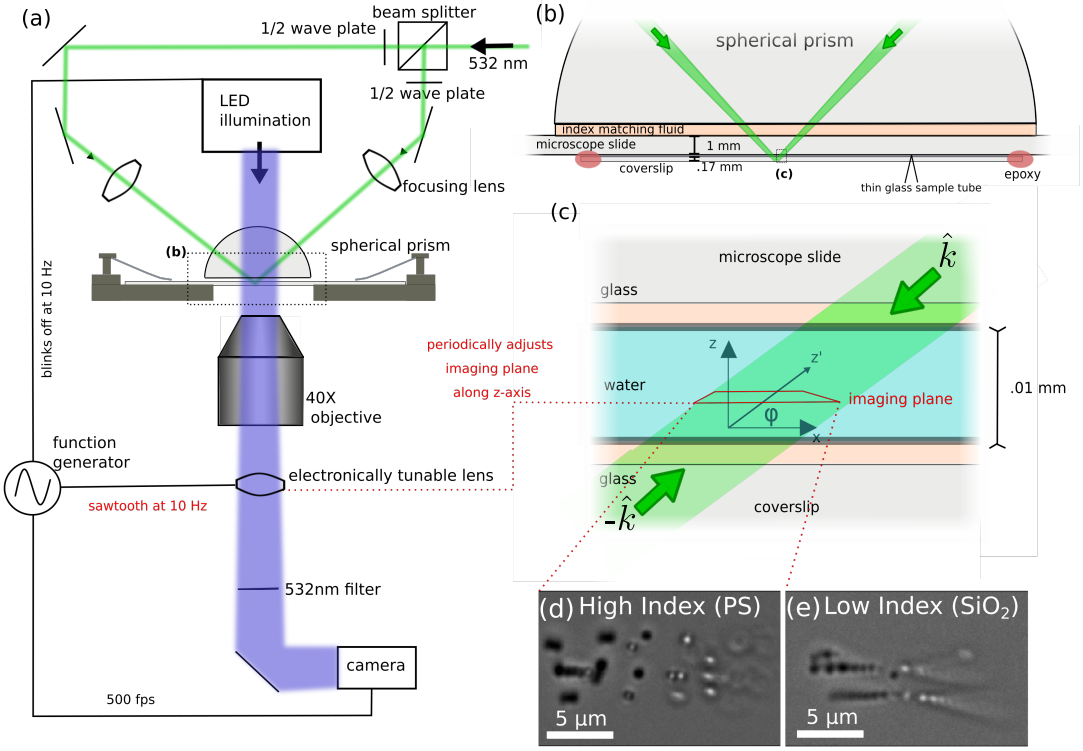

Figure 2.1: (a) Experimental setup. The laser beam is split into two paths that are aligned to counter propagate through the colloidal sample. Both beams are adjusted so that they are totally internally reflected at the bottom surface of the coverslip. The polarization and incident angle of each beam can be adjusted individually by rotating the 1/2 wave plate in each path. The camera, electronically tunable lens, and illumination source are all synchronized to a wave-function generator for the acquisition of 3-dimensional videos. (b) A closer view of the spherical prism and sample at a relatively accurate scale. Here we can observe how both beams are propagated through the various layers and are aligned such that they are counter-propagating and focused within the thin glass sample tube. (c) Depth profile of sample cell, we define z-axis as direction along the sample depth and $\hat{\boldsymbol{k}}$ as the axis corresponding to the beam propagation axis. The imaging plane is shifted along the $\hat{\boldsymbol{z}}$ axis by the electronically tunable lens. (d) Image of 500 nm polystyrene spheres in the optical field. The image is a single slice of a 3-dimensional z-stack of images. From the specific xy-plane, the different z-positions of the particles are made obvious by the distortion of particles out of focus. In general, we can observe that the particles tend to increase height as you move along the x-axis.(e) Image of 500 nm silica spheres in the optical field. The image is a single slice of a 3-dimensional z-stack of images. From the specific xy-plane, the various positions along the z-axis can be seen by the distortion of particles out of focus. In general, it is observed that the particles tend to increase height as you move along the x-axis.

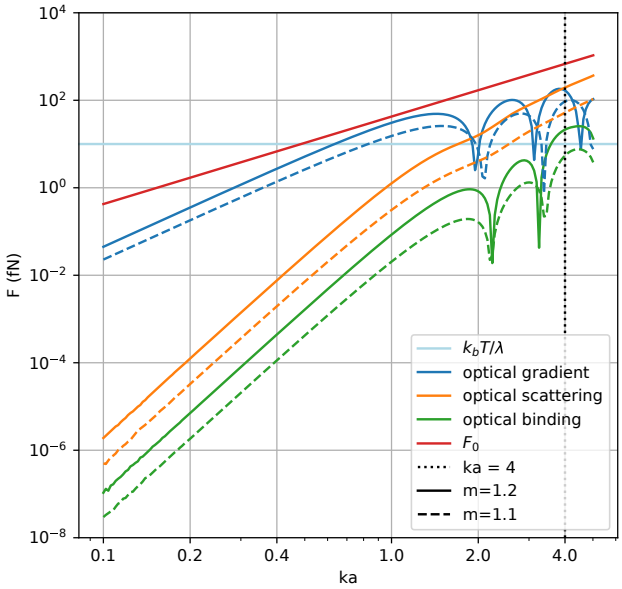

Figure 2.2: Strength of optical forces for a range of size-parameters (ka). The optical gradient force (blue) was numerically simulated by placing a single particle in a node of a standing wave, the optical scattering force (orange) was numerically simulated by placing a single particle in a propagating plane-wave. The optical binding force was obtained by placing two particles laterally in a counter-propagating field at a separation of 2λ. The reference force, F_0, is also plotted. In all simulations we assume a light intensity of 1 mW/μm^2.

in **§1.2**, the force strengths are highly sensitive to experimental parameters such as the size of the particles of interest. Of the measures, we include the first-order scattering force F_S, the first-order gradient force F_G, the lateral binding force F_B. Additionally we define a reference force, F_0, which is the total optical momentum impinging on a single particle in a plane wave of intensity I_0:

$$F_0 = \frac{I_0 \pi r^2}{c}, \tag{2.1}$$

where r is the radius of the particle and c is the speed of light. It useful to compare this to thermal excitation. For an order of magnitude estimate of how the thermal activity compares to the strength of the optical forces in the experiment, we can convert the thermal energy, k_bT, to an equivalent force by including a length scale. Given that the optical binding force has spatial oscillations with the wavelength of the incoming light, the approximate scale of the equivalent thermal force is given by $F_T \sim k_bT/\lambda \sim 10$ fN.

We performed a numerical analysis to predict suitable light intensity and particle parameters which should allow us to observe optical binding effects (**Fig. 2.2**). This plot, generated by CDM code, gives us a lot of information. For one, we observe that the optical binding force strength scales with the scattering force. This is expected as both phenomena are connected. As a second-order effect, the binding force is considerably weaker than the gradient and scattering forces. To estimate whether we will even be able observe considerable effects, we are looking for ranges in which $F_B > F_T$. I note that this analysis suggests that $F_B \ll F_T$ until $ka \gg 1$. Using a laser of $\lambda = 400$ nm and power density 1 mW/μm^2 we might expect to observe binding effects for particles of diameter $d > 200$ nm. This size requirement falls within our experimental range as we are additionally interested in resolving particles at an individual scale.

Secondly, we might also consider the role that the relative index, m, has on the ability to observe considerable binding forces. We know that $m = 1$ yields absolutely no scattering, however dielectric colloids can fall typically between $1 - 1.4$. While the entire range could be analyzed, we decided to instead focus on two major relative indices of interests. There are two materials which are readily available for purchase as mono-disperse spheres of various sizes: polystyrene and SiO_2. Because we are assessing a relatively unfamiliar force, we opted to limit ourselves to utilizing relatively familiar components which we could obtain consistently. Thus, in practice, we were able to focus our analysis with respect to a relative indices of polystyrene in water ($m = 1.2$) and SiO_2 in water ($m = 1.1$). I show both cases in **Fig. 2.2** and find that the although the SiO_2 particles experience relatively weaker optical forces they likely fall into the experimentally accessible range.

While this analysis suggests that a power density on the order of ~ 1 mW/μm^2 could be the enough to observe weak optical binding effects, we had to take careful consideration of how to design the optical pathway. For instance, if we consider covering an optical binding area of $\sim 100\pi\mu$m^2 which would require up to 0.5 W. While the simplest optical design would be to propagate the beam perpendicularly through a sample and image the dynamics from below, the objective lens would further focus the beam. This additional focusing through the lens could bring

the peak power density behind lens up to $\sim$ 800 mW/μm^2 assuming a .75 NA objective. This power density is extremely high and for obvious reasons something that we wanted to avoid. Clearly, the beam must be isolated if we wish to observe the effects of optical binding. We needed beam to be reflected at a layer between the sample and the objective lens.

One way to do this is to place a dielectric mirror between the sample and the objective. Doing so solves the issue of high-power, but introduces the issue of imaging through a thick glass provided that you can fit a mirror within the working distance of the objective. Through the addition of precision optical components and/or the fabrication of custom thin-mirrors, this scheme is theoretically possible. However, we opted to instead to convert a simple thin coverslip glass into our reflecting surface by utilizing total internal reflection.

2.2.2 Optical Setup: Total Internal Reflection

Our primary experimental apparatus is based on a custom microscope designed to observe colloidal interactions within a totally internally reflected beam. In doing so, it required us to separate the imaging coordinate frame from the beam coordinate frame. To achieve total internal reflection required the beam to be propagated at an angle, ϕ, from the bottom of the sample. This peculiar geometry was utilized as a necessary measure to protect sensitive imaging equipment. Note that, unlike an optical trap where the extremely high optical power density is experienced only at the site of interest where it is strongly focused, an optical binding setup may require similar maximum power density but for a much wider area. This demand requires a much higher optical power throughout the entire optical pathway. Not only did we expect high powers to be required to observe significant optical binding forces; but these high powers, if directed through a microscope objective would be focused further.

In the original design, there was one beam path which was weakly focused through a triangular prism. The prism sat on a microscope slide connected by index-matching fluid. The colloidal sample was placed in between the microscope

slide and a glass coverslip making it the final layer in the beam path. The beam was aligned to enter the prism at a 45° angle. It would then pass through the microscope slide at $\sim 45°$, the sample of water medium at $\sim 57°$ from the $\hat{\boldsymbol{z}}$ axis, and finally $\sim 45°$ through the coverslip. At this angle, instead of propagating through the final air interface, the beam is reflected and returned through the opposite side of the triangular prism and directed into a beam dump.

The expectation in this geometry was that scattering forces would push particles against the bottom surface of the sample while gradient forces would collect particles into the beam area. Thus this apparatus could give us a view of large scale optical binding in two dimensions. This experimental design would be very close to a scaled-up version of the original binding experiments [1], except with the incident beam not perpendicular to the surface. In testing this original design, we found that particles not only had a strong push downward towards the bottom surface of the sample, but tended to be pushed along the surface and out of the confinement area. Where we expected that the gradient forces and the downward scattering forces would be enough to trap particles at the surface, the scattering components parallel to the surface appeared to push particles out of the beam area.

The are potentially a few ways to solve this issue. To make the following discussion more clear I will describe the coordinate system. First, the lab coordinate frame is aligned with the imaging coordinate frame which is described by $\hat{\boldsymbol{x}}$, $\hat{\boldsymbol{y}}$, and $\hat{\boldsymbol{z}}$. The imaging plane is in the $\hat{\boldsymbol{x}}$-$\hat{\boldsymbol{y}}$ plane. The propagation vector of the beam, $\hat{\boldsymbol{k}}$, has both $\hat{\boldsymbol{z}}$ and $\hat{\boldsymbol{x}}$ components. The $\hat{\boldsymbol{z}}$ component pushes particles towards the bottom surface of the sample while the $\hat{\boldsymbol{x}}$ component pushes particles out of the confinement area.

Similar to optical trapping, one could focus the beam until the confinement force overcomes the scattering forces. Unfortunately, this would set a limit on the size of the optical binding region. Additionally, with strong confinement forces, it would be more difficult to separate optical binding effects from the first-order gradient forces. Because we wanted to maintain a larger binding area, we opted to instead balance the scattering forces.

We found that there were two configurations which allowed us to balance the scattering forces. The first was to introduce a second beam which propagated in the opposite direction along the $\hat{\boldsymbol{x}}$ axis but maintain the same downward component ($\hat{\boldsymbol{k}}_{\boldsymbol{x,1}} = -\hat{\boldsymbol{k}}_{\boldsymbol{x,2}}$ and $\hat{\boldsymbol{k}}_{\boldsymbol{z,1}} = \hat{\boldsymbol{k}}_{\boldsymbol{z,2}}$, where $\hat{\boldsymbol{k}}_{\boldsymbol{1}}$ and $\hat{\boldsymbol{k}}_{\boldsymbol{2}}$ are the propagation vectors of the first and second beam respectively). We considered this configuration as cross-propagating. With cross-propagating beams, we found that particles were able to be confined into a 2-dimensional lattice. By balancing each beam, the particles remain within the confinement area.

The second configuration is a more familiar counter-propagating geometry. In this configuration, a second beam is aligned with the first in the opposite direction ($\hat{\boldsymbol{k}}_{\boldsymbol{x,1}} = -\hat{\boldsymbol{k}}_{\boldsymbol{x,2}}$ and $\hat{\boldsymbol{k}}_{\boldsymbol{z,1}} = -\hat{\boldsymbol{k}}_{\boldsymbol{z,2}}$). While it manages to balance both components of the scattering force, we found that particles we no longer confined into a 2-dimensional array on the surface. In general, we found particles can be gathered instead into a 3-dimensional column that extends from the top to bottom surface of the sample. Interestingly, this geometry is the same as simulated by Ng et. al. [10]. By using counter-propagating beams with aligned polarizations, Ng et. al. showed that an array of particles could in theory be trapped into a 2-dimensional lattice away from a surface. In practice, we found that this confinement would be extremely difficult to maintain. Not only do thermal forces readily allow particles to move out of plane, but we find that small instabilities could drive particles out of lateral orientation from each other. We did find that the overall motion of the particles could be impeded by generating a standing wave with polarization alignment. In later sections, I describe quantifiable differences of colloidal behavior within the standing wave and cross-polarized counter-propagating wave. For now, it is important to note that trapping forces from the standing wave can yield considerable effects on stability but are unlikely to confine particles into a completely 2-dimensional lattice away from a surface.

We experimented with both cross-propagating and counter-propagating geometries, but shifted the main focus on the later. There have already been studies which looked at optical binding of 2-dimensional lattices on surfaces [25, 29] and thus we were most interested in a previously unexplored 3-dimensional geometry.

This geometry gives full access to explore the longitudinal and lateral binding forces and gives insight of bulk colloidal behavior to optical fields. For this reason the majority of experimental analysis in this thesis are performed with the optical designed described in **Fig. 2.1**a.

Two Gaussian beams ($\lambda = 532$ nm in vacuum, or 400 nm in water) are aligned and focused through the sample tube to generate a counter-propagating crossed polarized optical field ($w_0 = 27.0 \pm 0.3$ μm). The polarizations of each of the two beams can be adjusted individually which allows us to switch between a counter-propagating standing wave and a crossed polarized configuration. In this specific setup, a portion of beam power is redirected back towards the laser source which is removed using an optical isolator placed between the laser head and the beam splitter. The final focusing of the beam allows us to further modulate the beam power density. The orientation of the beam through the sample is at an angle of approximately $\phi_g = 45°$ through the glass layers and $\phi = 36°$ through the water. We achieve total-internal reflection at the glass-air interface at the bottom surface of the coverslip depicted in **Fig. 2.1**c.

2.2.3 3-dimensional imaging with an Electronically Tunable Lens

Since we were now working in a 3-dimensional environment, we also developed methods to collect 3-dimensional data. To do so, we used a combination of a microscope objective (40X, NA = 0.75) and an electronically tunable lens (ETL). The scanning of the ETL is synchronized with the imaging camera acquisition to capture 10 volumes per second with 50 frames per volume. By adjusting the focal length of the ETL, one can adjust the z-depth of the imaging plane shown in **Fig. 2.1**c. By driving the ETL approximately 6 % of its full range, we scan more than 10 μm which is the depth of the majority of samples. The signal output to the ETL is in the form of a periodic sawtooth pattern (driven at 10 Hz) which increases linearly for 70 % of the total period and quickly decreases linearly for the remaining 30 %. As such, the first 70 % of the period is used to create the

full volume. The 3D scanning method gave us a spatial resolution of 0.8 μm/pixel in the z-direction and a time resolution of 10 Hz which was sufficient to reliably locate particles within the volume.

Before utilizing the ETL, we did have to develop methods to calibrate it. In a bright field microscope setup an ETL can be placed in between the objective and tube lens to adjust the focal plane. This is achieved ultimately by adjusting the focal length of the lens via an applied voltage. The voltage range for the particular device is 0-5 V amounting to the total range of focal length between -500-333 mm. We utilize approximately 6 % of that total range. Relating the applied voltage to focal depth was achieved through a calibration procedure. The calibration procedure consisted of locating a fixed particle in a sample. Using the fixed object as a reference we could apply a voltage to the lens and physically translate the objective until the object was back in focus. The physical position of the objective is read out with micro-precision via the *Mad City Labs - Micro-Controller*. Collecting a set of Voltages and positions provides a linear relationship between the lens focus and the focal depth. Furthermore, the depth of the samples are known to within 1 μm. This depth can be used to validate the calibration provided there are objects located at the top and bottom surfaces of the sample.

2.2.4 Sample preparation

Colloidal samples are diluted in water ($\sim$ 0.01 w/v %) and placed into thin rectangular Borosilicate tubes (100 μm wide $\times$ 10 μm thick $\times$ 50 mm long) purchased from *VitroCom*. The samples are drawn into the small tubes through capillary forces. We performed experiments with polystyrene (relative index $m = 1.20$ [32, 33]) and silicon dioxide (relative index $m = 1.10$ [34, 33]) purchased from *microParticles GmbH* as well as *Bangs Lab*. In the experiments, the number of colloidal particles are in the range of 10-1000 particles depending on particle size and density. The tubes allow us to keep a precise sample depth of 10 ± 1μm. This tube depth is important for confining particles to a range in the z-direction. A single drop of index matching fluid is placed onto a microscope slide and the tube containing the sample is layed onto the drop. The index matching fluid is used to

remove an air gap between the microscope slide and the sample tube. An air interface will disrupt the total internal reflection pathway. A coverslip is then placed directly onto the sample tube. The addition of the coverslip is used to provide stability to the sample as the thin tubes are fragile as well as provide a flat glass surface to image through. Finally, the coverslip is glued to the microscope slide, using UV curable Epoxy (*Norland Optical Adhesive NOA61*), which seals the tube and index matching fluid. The samples are fixed onto the *Mad City Labs - RM21* microscopy base allowing for micro-precision movement of the sample in the *x-y* plane.

2.3 Observations of Self-Organization

At the outset of the experimentation, we sought to cover a wide range of particle sizes ($ka = 1.6 - 7.5$) as well as asses the differences between commonly available polystyrene ($m = 1.2$) and silica ($m = 1.1$) microspheres. The design of each experiment are similar to that described in **§2.2**, however there are a number of alterations which can be made to the optical setup. In most cases we utilize counter-propagating beams either with crossed or aligned polarization; however I also report results involving cross-propagating beams in which the scattering forces in the x-y plane are balanced by the two beams but the scattering forces in the z direction of each beam push particles against the surface. This geometry is a much less studied geometry of optical binding in 2-dimensions which is not governed completely by lateral forces. Finally, I present a special geometry which can be obtained by a slight misalignment of the counter-propagating beams to force particles into a quasi-two-dimensional plane that is free from the sample surface. It is in this highly constrained configuration within a 2-dimensional plane of longitudinal and lateral interactions which we observed the most bizarre set of behaviors. This section thus serves as a collection of mostly qualitative observations that highlight known and previously unknown aspects of the optical binding force in bulk colloidal material.

From the previous chapter, we saw that the optical binding force is a combi-

nation of second-order gradient and scattering forces. In **Fig. 2.2**, we plot the relative strength of first-order gradient and scattering forces for polystyrene and silica particles to approximate their relative contributions to the binding force. I show here that the size parameter, ka, has a strong effect on the relative balance of scattering and gradient forces, thus I draw a distinction between recent studies done on dielectric nanoparticles [30]. Note that the optical binding force is computed only for a pair of particles spaced by 2λ; for larger numbers of closely spaced particles it can be 1–2 orders of magnitude stronger. We observe that polystyrene particles, which have a higher index of refraction generally have a stronger scattering force response.

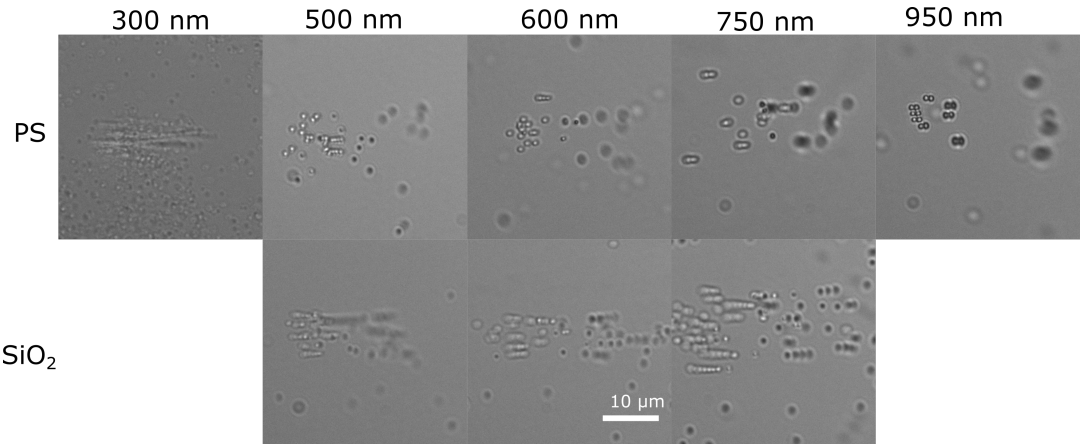

Figure 2.3: Particles in a counter-propagating field of for various sizes. In each case a power density of 2 mW/μm^2 was used.

What we observe in all cases studied is that particles will collect into the beam and extend from the bottom surface to the top surface of the sample **Fig. 2.3**. For polystyrene spheres at 300 nm, we find that multiple lines form along the beam propagation. This is due to particles self-aligning along the propagation axis. Because the beam is not confining the particle in 1-dimension, multiple rods along the axis form. At larger particle sizes, particularly, 500 nm and 600 nm, we find that particles have the tendency to either align into chains that extend from the bottom to the top of the sample –or– we find a cluster of tightly packed particles. At larger sizes, we find that particles have a tendency to form into many smaller clusters. For the silica particles, we find less differentiation between the

sizes. In most cases, we find the formation of elongated tightly packed rods.

To summarize more generally, particles will tend to align along the field propagation. Once aligned, particles either repel each other to form extended chains or collapse onto each other. If collapsed, the number of tightly bound particles appears to depend on the size of the particles and strongly depends on the relative refractive index. For instance, silica particles with a lower relative index can easily collapse into long extended rods of particles, whereas the polystyrene particles appear to have a limit. Extended observations of 500 nm polystyrene particles for instance do not yield clusters longer than five particles.

Furthermore, in all cases we find evidence of highly dynamic behaviors and instabilities. While stability increases with less particles. Indeed, we have observed optically bound structures stabilized on the order of minutes at for a small number of particles. At higher densities, instabilities drive the system into constantly active motion. On few cases, which will be highlighted in the following sections, we observe that at moderate densities, one can observe fluctuations in and out of highly stable and highly unstable behaviors.

2.3.1 Optical binding in an extended boundary

Since we observed such strong boundary effects, we sought to observe the binding along the propagation axis ($\hat{\boldsymbol{k}}$) from an alternate perspective. For this, we utilized a square sample tube and imaged the colloids perpendicular to the field propagation.

An alternative custom microscope system was designed to mitigate effects from high-powered beam and allows the in-focus observation of optical binding along the beam propagation axis. Here, two Gaussian beams ($\lambda = 400$ nm in solution) are aligned and focused perpendicularly through glass sample tube with four flat sides. The open ends of the tube a sealed off with *Norland 61* optical adhesive. Illumination and imaging are performed through the sides of the tube perpendicular to the beam propagation axis using a white light source focused onto the sample from below and a 40X Nikon objective lens from above. In this design,

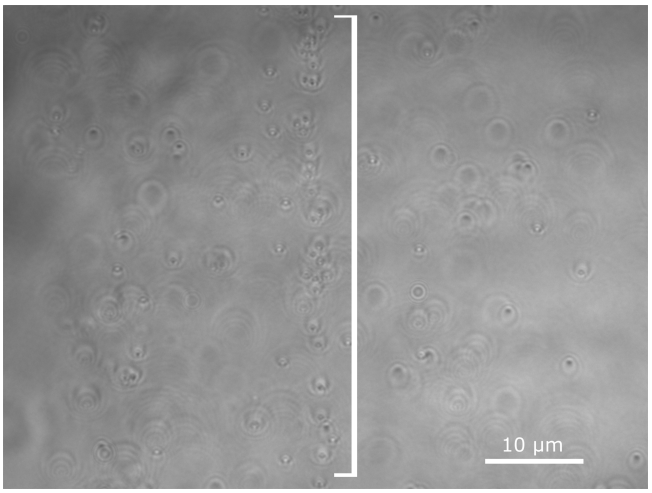

Figure 2.4: 500 nm particles collected in a counter-propagating beam. The beam is propagating along the y-axis of the image directly in the center (guided by white bar). Particles at the center of the image can be seen in an extended chain.

3-dimensional imaging was not utilized, but can in theory be achieved in the same manner as previously described for the first apparatus.

The main benefit of this design is that the beam can be propagated through the sample at a perpendicular angle. This scheme allowed us to validate that particles indeed formed chains along the propagation axis. Additional benefits of the apparatus include the ability to easily adjust the angle of beam incidence. Furthermore, the particular microscope arrangement does not require a depth scan to analyze long range longitudinal binding. This is important as we find the general tendency for particles to self-organize into longitudinal arrangements. One of the major drawbacks of this design is that it limited our ability to work within a confined boundary. We found that with the use of thin tubes ($< 30\mu$m), we observed highly correlated behaviors using the total internal reflection scheme. Furthermore, the restrictive boundary forced particles to more readily assemble into a 3-dimensional structure. Unfortunately, some of these behaviors are lost when the system is less confined. If given enough space along the propagation axis, we found that particles will tend to self-assemble into a single chain. While this is indeed an important finding, we were more interested in higher density effects. For the current apparatus, a sample required to match the boundaries

capable with the total internal reflection apparatus would be impossible to image through. In future work, the use of the completely perpendicular imaging path would be most useful in assessing optical binding at much larger scales with higher density colloidal systems.

In this orientation, on a few accounts we observed the formation of an at least one extended chain of particles **Fig. 2.4**. The collection of particles, although stable in alignment exhibited collective flows towards either direction along the beam propagation axis. While this configuration did not provide the desired observation of clear binding in 3-dimensions, it did allow us to confirm that with extended boundaries particles will still tend to align, and they can form extremely long particle chains (> 50 μm).

2.4 Active Colloidal Clusters

Of the set of experiments that were performed, polystyrene spheres of $ka = 4$ demonstrated a unique ability of switching between stable to highly active and unstable behaviors. Much of the behavior was unexplained by prior knowledge and we sought to understand where the abrupt transition into high activity arose. After further examination at various densities and lengths of time, we began to observe that the instabilities appeared to be connected to the presence of optically bound colloidal clusters of (3-5) particles. Our hypothesis was that a cluster of particles, though multiple scattering effects could greatly modify the scattering pattern such that the cluster behaves as a different type of particle – a system of identical spheres emerging into a system of spheres and clusters. These clusters, which now scatter differently, thus under non-reciprocal interactions with surrounding objects. To test this hypothesis, we decided to directly compare the polystyrene (HIP - 'High Index Particle') and silica (LIP - 'Low Index Particle') spheres of the same size. Here, although the particles are roughly the same and the two-body forces are highly similar as will be shown in **§2.4.2**, we would expect to find stronger multiple-scattering effects in the polystyrene sample which drastically alter the self-organization behavior. The following sections detail this analysis along with

methods undertook to quantify the active behavior.

2.4.1 Changes in self-organization behavior with refractive index.

Optical binding effects are immediately apparent between particles within the beam region. For instance, spatial ordering is immediately observable within the beam area – effects which can be enhanced by increasing the light intensity. The most apparent feature is the generation of multiple chains of particles aligned along the beam propagation direction (**Fig. 2.1**c). Once collected into a chain, particles within the chain can be observed to move collectively together within the beam region. The density of particles is large enough to observe the formation of multiple chains at a time.

Other features of the formed structures arise on further examination. For instance, the HIPs are found to self-organize into extended chains which extend along the sample depth–or–small clusters of typically (3-5) particles long. Both HIP structures can be observed in **Fig. 2.1**c. Unlike the HIPs, the LIPs tend to form extremely long and close packed chains of particles (rods). Two LIP rods can be observed in **Fig. 2.1**d.

2.4.2 Comparing observations to two-body forces

To understand the dominating interactions which are leading to the general behavior of both systems, we numerically generated two-body force maps for the two particle types (**Fig. 2.4**a,b). The force maps were created using a CDM based simulation, as described in **§1.2** [11, 12]. Comparing force maps for HIP ($m = 1.2$) and LIP ($m = 1.1$) particles reveals surprisingly little difference, apart from the overall strength. The strength differences can be observed in **Fig. 2.2** by comparing how the optical forces are generally stronger for HIPs. The strength can be found to scale approximately like the reflectivity of a dielectric plane, which scales like $\sim (m-1)^2$ which was discussed in the previous chapter.

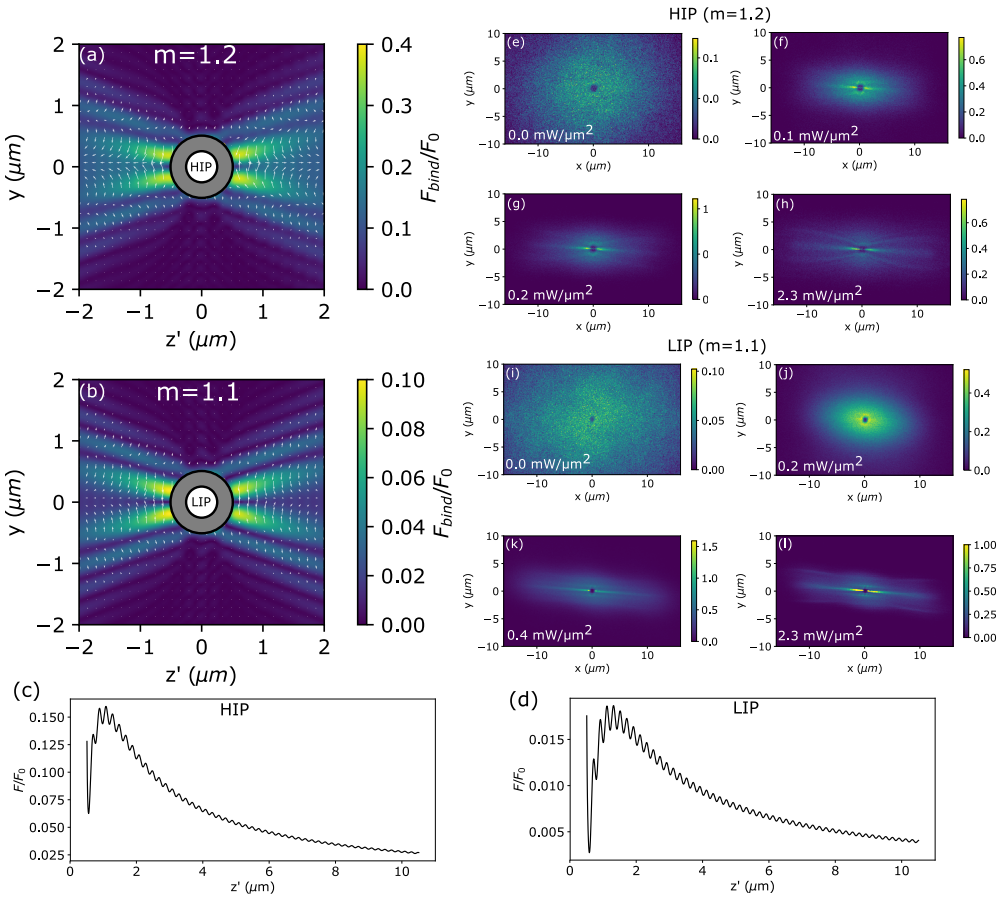

Figure 2.5: **(a,b)** Two-body force map of optical binding forces for HIPs and LIPs ($ka = 4$) placed in counter-propagating crossed-polarized plane wave ($\lambda = 0.4\mu$m in solution) propagating in the $+\hat{\boldsymbol{k}} = +z'$ and $-\hat{\boldsymbol{k}} = -z'$ direction. Maps are obtained by placing two particles in a CDM simulation and calculating the force applied on each particle at various displacements which fill the map space. The forces are provided in a unit-less scale normalized by the reference force, F_0, described by the single scattering force on a single particle of the same size and material. The direction of the arrows represent the direction of the force, while the size represents the relative strength. The white region at the center of the plots represents the particles, while the grey region around it is the excluded volume (i.e. particles placed at these separations would overlap). **(c)** The optical binding force along the axis of propagation for an extended range for two HIPs. **(d)** The optical binding force along the axis of propagation for an extended range for two LIPs. **(e-h)** 2D pair-correlation functions for HIPs in the x-y plane at various light intensities. **(i-l)** 2D pair-correlation functions for LIPs in the x-y plane at various light intensities. The color bar in the pair-correlation functions gives the 2D probability density of the particles, and has units of μm^{-2}.

Despite this, the two-body force maps can be used to describe some of the overall structures observed in the system. The long range alignment along the beam propagation for the HIPs and LIPs are qualitatively consistent with the two-body force maps (**Fig. 2.5**), which suggest strong forces can tend to pull particles onto the axis of propagation ($\hat{\boldsymbol{k}}$). The $\hat{\boldsymbol{k}}$ axis, as shown in **Fig. 2.1**b is rotated 54° from z. For comparison, we approximate the energy $F_0\lambda \sim 65k_bT$, thus the HIPs can experience $\sim 20k_bT$ of energy keeping them aligned in the $\hat{\boldsymbol{k}}$ axis in the beam at 1 mW/μm^2. The LIPs experience $\sim 5k_bT$ at 1 mW/μm^2.

The HIPs force-map shows a repulsive force between particles that are aligned along the field propagation (**Fig. 2.5**a). This fits with the observation of HIPs forming extended particle chains (**Fig. 2.1**c), rather than tightly packing. What the force-map fails to predict for the HIPs are the presence of the smaller tightly packed HIP clusters also found in the experiment. While it is expected that we observe structures that cannot be predicted from two-body optical binding interactions, here we observe an emergence of a force which is not only strongly contributing, but can act in the opposite direction of the two-body force. For the HIPs, the two-body force is repulsive along the $\hat{\boldsymbol{k}}$ axis but we observe experimentally an unexpected close-range attractive force suddenly drives particles together into small clusters.

2.4.3 Pair-correlation function

To map the time-averaged structure created by optical binding forces, we compute a 2D pair correlation function (2D PCF). Given all the 2D particle positions, $\boldsymbol{r}_i$, we can compute all relative displacements $\boldsymbol{\Delta}_{ij} = r_i - r_{j\neq i}$; the 2D pair correlation function is then the histogram of these displacements, averaged over all frames in the data set and normalized by the bin size (so that the result is expressed as a 2D density). The form of the pair-correlation function also gives an approximation for an effective potential through which the particles interact. We collected the data for the pair-correlation function by recording the positions of colloidal particles all located within the same weakly focused beam of light. The beam is fixed at a constant light intensity for a duration of 2 mins during which we collected

3-dimensional imaging data. 3-dimensional volumes were used to locate particles over the entire 10 μm in depth. However, as the optical configuration results in poor resolution in z, we discard the z-positions essentially projecting the 3-dimensional information onto a 2-dimensional plot. As such, the $\hat{\boldsymbol{k}}$ axis is projected along the x-axis. The particles were located using the *trackpy* implementation of Crocker and Grier [35, 36]. While the particle speeds and dense particle clustering made it challenging to track particles through time, we found that the algorithms were quite efficient at locating particles within a frame. We found relatively low fluctuations in the total number of particles from frame to frame suggesting that the particle locating algorithms were performing consistently. Inter-particle displacements were determined by particle locations given for each time-step, thus the frequencies of each displacement over the entire run were available.

The 2D pair-correlation function (PCF) for the HIPs suggest an increase in spatial order with the increase in light intensity **Fig. 2.5**e-h. The form of the PCF shows the dominating feature that the HIPs tend to align along the beam propagation. At higher light intensities, $I > 1$ mW/μm^2, multiple lines off-axis begin to appear. This not only suggests that particles are interacting to form long range structures, but that there are optical binding interactions occurring in multiple directions within the field. For example, at high powers there is clear evidence of preferred inter-chain transverse spacing of ~ 1 μm. This can be explained by the computed pairwise force diagrams, which have a converging force in the y direction at these separations. The two-body force maps (**Fig. 2.5**a,b) can be used to help explain the multiple off-axis lines that appear in the PCF at higher light intensities, as we can observe multiple off-axis lines in which the force arrows converge.

The 2D PCF for the LIPs are very consistent with the observation that the particles collapse into tightly bound rods (**Fig. 2.5**i-l). One feature that becomes prominent are secondary off-axis lines at higher light intensities. The secondary lines are evidence of multiple rods interacting to form a long-range regular spacing over time.

2.4.4 Volume Mean Squared Difference (VMSD)

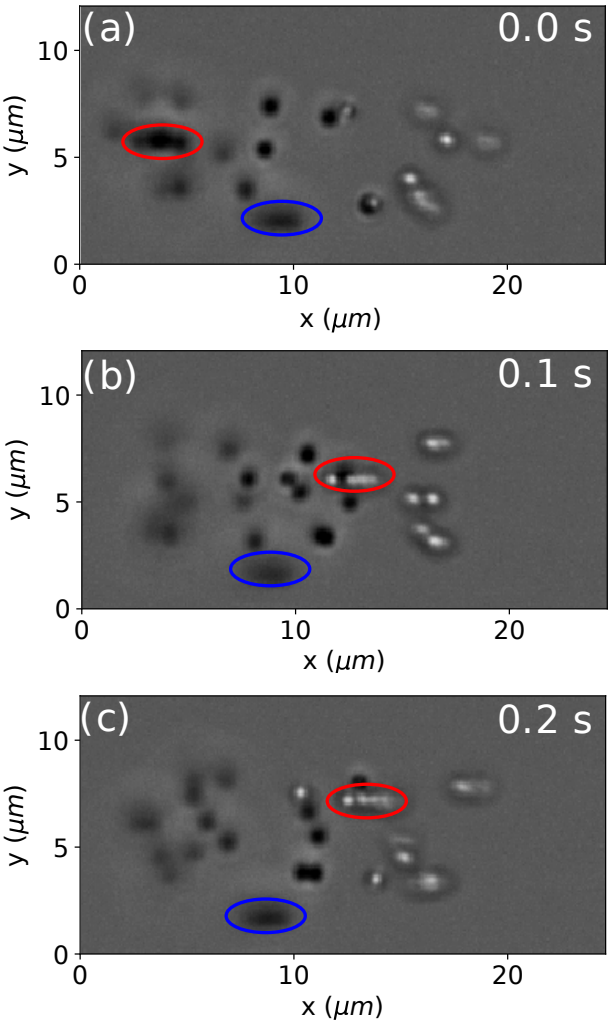

Figure 2.6: **(a-c)** Three snapshots of the optically bound HIPs over a 0.2 s duration. Two clusters are circled: (red) cluster of 5 particles ballistically moving (>80 μm/s) through the sample and (blue) isolated cluster of 4 particles remaining relatively still.

We use the mean squared displacement of particles to determine their dynamic behavior. Due to high-density particle clustering and the high velocities of clusters evidenced in **Fig. 2.6**, it is difficult to reliably track individual particles through time. This is especially true for close-packed clusters, which – as we shall show later – appear to drive motion in the HIPs. Instead of attempting to directly track the particles in time, we use a proxy for the mean squared displacement by

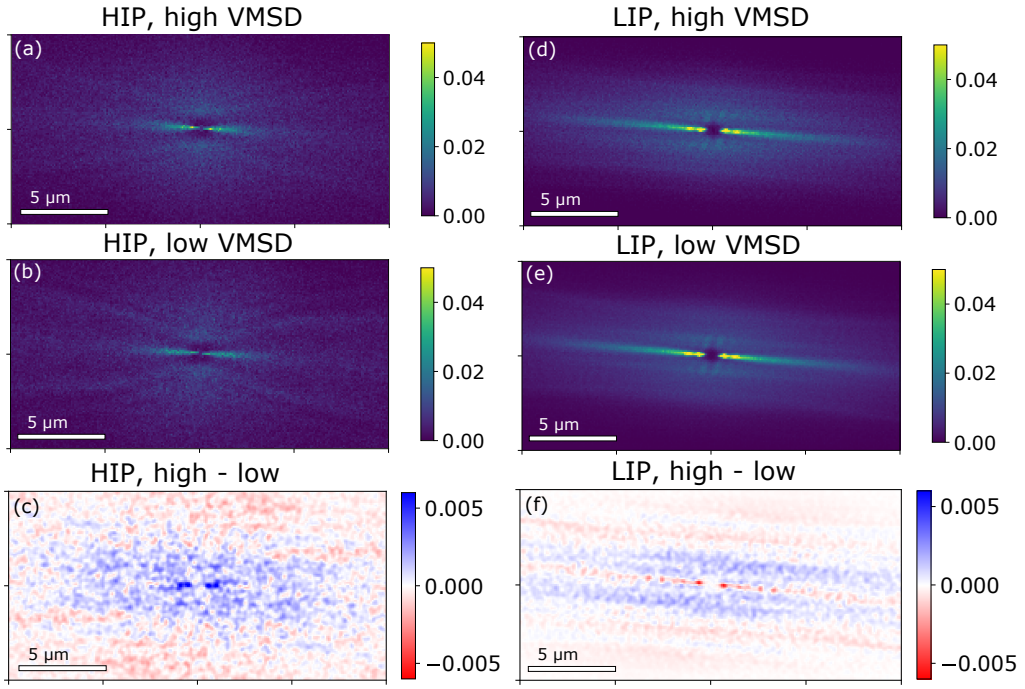

Figure 2.7: **(a)** HIP PCF for frames with higher (top 30%) VMSD values. **(b)** HIP PCF for frames with lower (bottom 30%) VMSD values. **(c)** The difference between the high VMSD and low VMSD pair-correlation functions for HIPs. **(d)** LIP PCF for frames with higher (top 30%) VMSD values. **(e)** LIP PCF for frames with lower (bottom 30%) VMSD values. **(f)** The difference between the high VMSD and low VMSD pair-correlation functions for LIPs. Displacements found more often in the higher VMSD frames are positive (blue) while displacements found more often in the lower VMSD frames are negative (red). The PCFs are normalized by dividing the 2D particle density by the number of particles.

obtaining the mean squared difference between two subsequent image volumes.

We found that the volume mean squared difference (VMSD) between subsequent frames gives us more consistent measures of motion while remaining highly correlated with the true mean squared displacement. The VMSD, Δ, is given by:

$$\Delta(t) = \frac{1}{N_p(t)} \left[\sum_{i,j,k}^{volume} \left(p_{i,j,k,t} - p_{i,j,k,t-dt}\right)^2 - \Delta_0 \right] \tag{2.2}$$

where $p_{i,j,k,t}$ is the pixel value at a given location and time, $dt = 0.1$ is the time between frames, and Δ_0 is the background VMSD caused primarily by camera noise, and is computed for when there are no moving particles in the frame. Δ is

proportional to the squared particle displacement provided the particles average motion between frames is smaller to or comparable the particle size. In practice, we normalize this value relative to one obtained by turning the optical binding laser off, in which case the particles experience only Brownian motion.

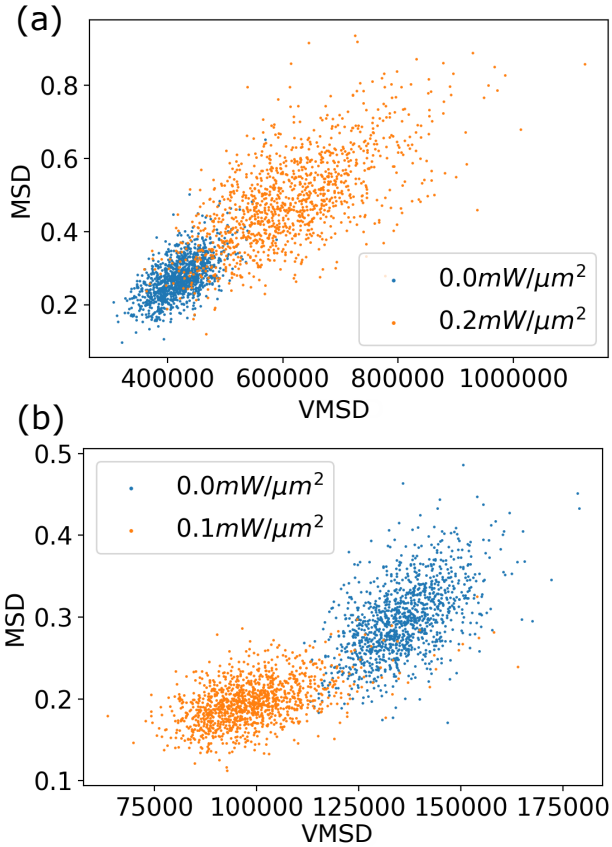

Figure 2.8: VMSD values compared to 2-dimensional mean squared displacement (MSD) in the xy-plane for (a) HIP (PS) and (b) LIP (SiO_2) particles.

The calibration of the VMSD values were performed with the use of particle tracking of diffusive particles. Although we are unable to provide an absolute estimate of speed, due to poor z-axis resolution, the strong correlation between particle speed and the VMSD value, shown in **Fig. 2.8** provided us a means to determine the relative motion for particles moving much faster in a denser environment when optically bound.. The second limitation is that the VSD value is capped at displacements that are slightly larger than the particle diameter. At the volume rate of 10 volumes/s, particles undergoing Brownian motion are moving

slow enough; however we have observed that particles undergoing optical binding forces can be propelled much faster. One way to alleviate the limitation is to record at a higher volume rate; however, it is currently unfeasible to cover the full range of possible particle speeds. This limitation is also present in traditional tracking methods. Although the motion of the fastest particles are underrepresented in the VSD values, the VMSD method still allows a maximum value to be assigned. Traditional tracking methods would not be able to assign a velocity value at all. I also note that underrepresenting the motion of the faster moving particles only acts to underrepresent the strength of the findings.

Furthermore, the VMSD values must be normalized by the number of particles in the frame. The number of particles, N_p, is estimated by the following:

$$N_p = c_0 \sum_{i,j,k}^{volume} |p_{i,j,k,t} - b_{i,j,k}| + c_1 \tag{2.3}$$

Where $b_{i,j,k}$ is belongs to a volume representing the sample devoid of particles. c_0 and c_1 are fitting parameters determined by linearly fitting the number of particles found by traditional tracking methods to $\sum_{i,j,k}^{volume} |p_{i,j,k,t} - b_{i,j,k}|$ for a system of particles undergoing Brownian motion.

The distribution average particle motion for the HIPs is provided in **Fig. 2.9**a. At lower light intensities, we find narrow distributions of the average particle motion and average values lower than what is found in a Brownian system, reflecting the fact that the particles are being confined by the optical binding forces. At higher light intensities, we find that the distributions shift to higher average values and the size of the fluctuations are greater, indicating the presence of a non-conservative driving force.

Surprisingly, comparing the pair-correlation function to the VMSD values suggests that the average motion is increasing even as the particles are becoming more ordered. This would not be expected for a conservative pair-wise force; in this case ordering will result in weaker fluctuations. We do indeed observe this for lower power levels ($<$0.4 mW/μm^2). Above these power levels, the increasing motion suggests that we are forming collections of particles which experience additional non-conservative forces from the optical field.

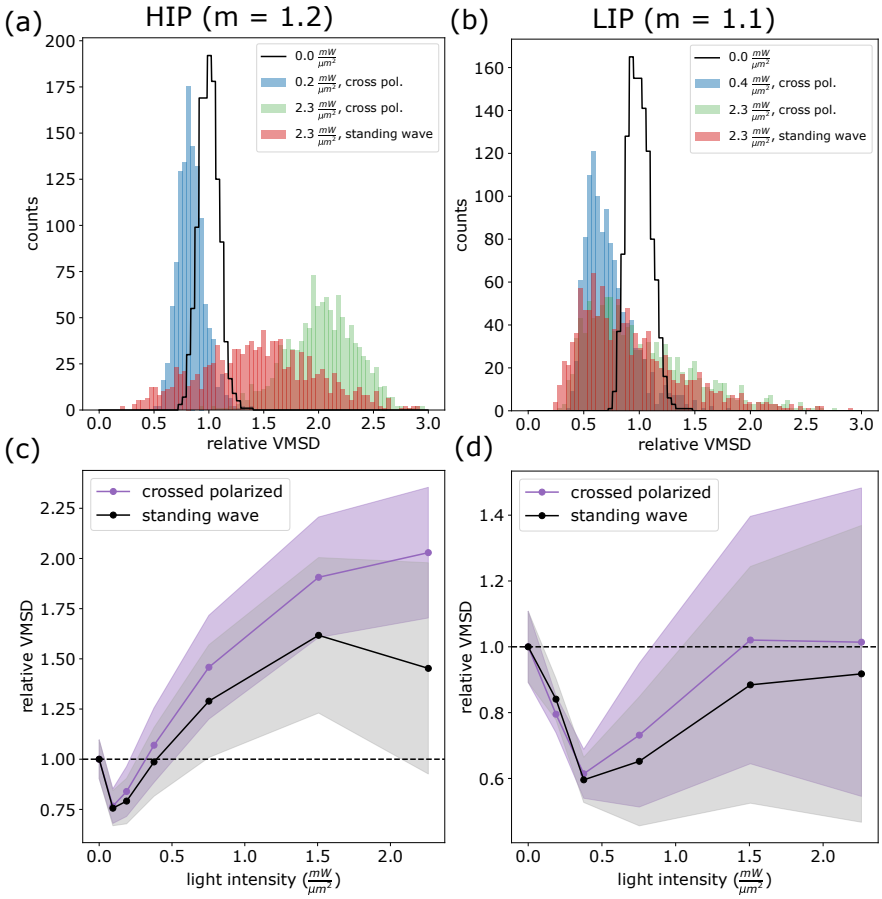

Figure 2.9: **(a)** Distribution of relative VMSD values over 2 min duration for various intensities. For the high light intensity case (2.3 mW/μm^2) we share a comparative distribution of VMSD values for the same system in a counter-propagating standing wave. **(b)** The variation of VMSD value over 2 minutes for various light intensities. The shaded regions represent the standard deviation in the relative VMSD values. Values over the dotted line represent the average motion of the particles greater than what would be observed when the optical binding light is turned off (i.e. purely Brownian motion). **(c)** Distribution of relative VMSD values over 2 min duration for various light intensities. For the higher light intensity case (2.3 mW/μm^2) we share a comparative distribution of VMSD values for the same system in a counter-propagating standing wave. **(d)** The variation of VMSD value over 2 minutes for various light intensities. The shaded regions represent the variation in the relative VMSD values. Values over the dotted line represent the average motion of the particles greater than what would be observed in a purely diffusive system.

We found that the behavior can be altered by aligning the polarizations of the counter-propagating beams to generate a standing wave pattern. In this config-

uration, the optical binding area includes multiple planes of high light intensity perpendicular the the propagation axis and separated by $\lambda/2$. While the overall average motion is suppressed in the standing wave, the system is still observed to fluctuate strongly between low average motion ($\sim 0.5 \times$ Brownian motion) and high average motion ($\sim 2.5 \times$ Brownian motion). At the same light intensities to the previous configuration, the standing wave had the effect of dramatically suppressing the overall motion.

Using the same range of intensities, the same analysis was done for the LIP system (**Fig. 2.9**b,d). At lower light intensities, we find narrow distributions of the average particle motion and mean values lower than what is found in a Brownian system. At higher light intensities, the average values do not exceed what is found in the Brownian system; however the distributions are far less Gaussian. The distribution suggests that the average motion is low with occasional rare events that lead to high motion. The LIPs in the standing wave do not show significant differences than particles in the cross-polarized counter-propagating beam.

Comparing the dynamic behavior between the HIPs and LIPs, there are clear differences between the two systems. The optical binding force when increased is shown to significantly increase the average kinetic energy of the system of HIPs. This implies that optical binding is a source of non-conservative motion that is especially present in the HIP case. We believe that non-conservative second-order scattering forces, expected to be stronger for the HIPs, is contributing to the higher overall motion. The LIPS are instead dominated by second-order gradient forces thus pack into the rod structures until density limitations require the formation of new rods. Where the standing-wave generates first-order gradient forces which compete with the second-order scattering forces to suppress the overall motion, the same standing-wave does not show much of an effect on the LIPs which are already dominated by gradient forces.

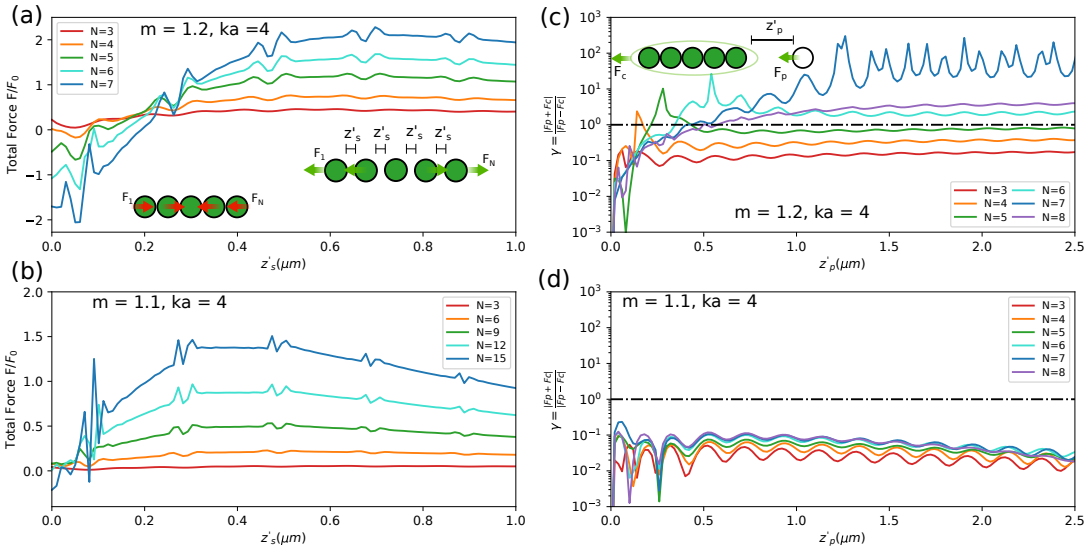

Figure 2.10: (a,b) 1-dimensional simulation of forces on particle chains. Particles are placed into a equidistant configuration aligned with the beam axis of propagation ($\hat{\boldsymbol{k}} = \hat{\boldsymbol{z}}$') with inter-particle distance, z_s'. At each inter-particle spacing, the total outward force is calculated. A positive force represents a net-force pushing particles away from each other while a negative force represents a net-force in which particles are attracted. We performed the simulation for (a) HIPs (m=1.2, ka = 4) and (b) LIPs (m=1.1, ka = 4) for various cluster sizes (N) (c,d) 1-dimensional simulation of forces between clusters and neighboring particles. A cluster of N touching spheres is aligned along the axis of propagation with a single particle and the absolute sum over the absolute difference of force on the cluster and the force on the particle are plotted for various particle-cluster spacings, z_p'. Simulations were performed for (c) HIP (m = 1.2, ka = 4) and (d) LIP (m = 1.1, ka = 4) particles.

2.4.5 Pair-correlation function difference

We see clear dynamic differences between the HIPs and LIPs; in particular, the HIPs are observed to experience higher average kinetic motion at high powers and a wider range of fluctuations of that behavior. In each case, we can use the fact that the kinetic motion does fluctuate to subset the data into high motion frames and low motion frames. Doing so gives us a method to compare particle configurations which may be correlated with driving instability in the system. To do so, we sort frames from a single video by the VMSD value which represents the average kinetic motion. We can use each subset of frames to generate PCFs for

the top 30% and the bottom 30% VMSD values. Because of the wide distribution of VMSD values, we focus on particles in a high powered (2.3 mW/μm^2) standing wave.

Comparing the PCFs for the high VMSD frames (**Fig. 2.7**a) versus the low VMSD frames (**Fig. 2.7**b) for the HIPs shows subtle differences. Primarily, we find more defined features for the low VMSD PCF. This suggest that the system fluctuates between slower moving ordered states to faster moving disordered states. Indeed, we observe sudden collapses and regeneration into order states in these optically bound systems.

Secondly, we observe that there is a higher distribution of particles in close proximity for the faster moving system. We illuminate this subtle difference by subtracting the low VMSD PCF from the high VMSD PCF shown in **Fig. 2.7**c. We propose that multiple scattering effects which are stronger when particles are at close-range could be driving the collapse of stability and increase in average kinetic motion of this system.

For the LIPs, we find that the high VMSD PCF (**Fig. 2.7**d) versus the low VMSD PCF (**Fig. 2.7**e) are both structurally similar. Not until taking the difference between the two as shown in **Fig. 2.7**f, do we see that there are subtle differences. For the low VMSD PCF, we observe that particles tend to be distributed among multiple lines: a single line that passes the origin and multiple off-axis lines. These lines are evidence of the self-organization into multiple rods. The center line represent displacements between particles that belong to the same rod and the off-axis lines represent displacements between particles that are located in neighboring rods. Interestingly, the differences between the high and low PCFs suggest that inter-rod distance may play a role in the average kinetic motion of this system. For instance, one can observe in **Fig. 2.7**f that the the first off-axis line is closer to the center line for the higher VMSD frames.

Comparing the HIPs and the LIPs is useful for understanding how multiple scattering is effecting these systems at different scales. For the HIPs, where scattering is much stronger, we find that the presence of small clusters are generally correlated with higher kinetic motion and less structural order of the overall sys-

tem. We propose that HIP clusters can be treated as an emergent species which can alter the system dynamics. On the other hand, the LIPs can generate much larger stable structures before the system fluctuates dynamically.

2.4.6 Pathway to cluster formation

The two-body force maps cannot describe how a cluster or rod forms; in fact, the two-body force maps suggest a weak repulsive force among particles that are aligned along the beam propagation. As a result, we believe the cluster formation can only be explained by considering a complete N-body force which we compute using the CDM.

We find numerically that when the separation between aligned particles is sufficiently large ($\gtrsim 0.25\mu$m) the total force is always repulsive for HIP chains and increases in strength with the number of particles (**Fig. 2.10**a). This suggests that a chain of particles aligned along the propagation axis should remain spread apart. This is consistent with some of the structures found in the experiment: the lower density HIP chains are often found extending from the lower to upper boundary of the sample. The strong repulsion at long range could also act as a barrier to cluster formation at very high light intensity and low particle density. The trend is similar for LIP chains μm (**Fig. 2.10**b).

At smaller distances, we observe a decrease in repulsive strength for all HIP chains. For HIP chains of more than 3 particles, we observe an overall change in sign of the force (**Fig. 2.10**a). This result suggests that the two-body repulsive force (**Fig. 2.5**a) dominates as long as the particles are far away; however, when many HIPs become in close range, N-body forces are strong enough to overcome two-body repulsion and switch the sign of the force entirely.

The same analysis of the LIP chains of particles shows a similar reduction of the repulsive force at shorter distances; however, an attractive force does not appear until the number of particles exceeds $N = 14$ (**Fig. 2.10**b). The initial reduction of the force, even at small N, is indicative of the presence of non-pairwise forces; however the effects are clearly weaker in comparison to the HIPs.

The numerical results provide a potential pathway to the previously unexpected formation of clusters. The results also highlight the unique nature of the N-body optical binding forces. These effects are shown to be comparatively much stronger for the HIPs. This supports the hypothesis that a major factor driving the differences in behavior between the HIP and LIP systems is a stronger presence of N-body forces due to the higher scattering strength of HIPs.

2.4.7 Non-conservative forces on clusters

We simulated the effects of a particle cluster as it grows in size and interacts with neighboring particles. We simulate a simplified configuration of N-particle closed packed cluster in line with a single lone particle at varying distance. We then compute the total force on the clustered particles, F_c, as well as the force on the lone particle, F_p. To compare the relative presence of conservative and non-conservative forces, we use the following quantity:

$$\gamma = \frac{|F_c + F_p|}{|F_c - F_p|} \tag{2.4}$$

If the forces are equal and opposite – indicating a conservative interaction – we will obtain $\gamma = 0$. In contrast, if the system is equal but in the same direction, this would be indicative of a system which would be driven ($\gamma \to \infty$).

Observing γ for the interaction between the HIP cluster and particle, we find that the value increases exponentially as the cluster size increases from 2-6 particles (**Fig. 2.10**c). At $\gamma > 1$ the force between the cluster and the particle are in the same direction, while for $\gamma \gg 1$ the forces are highly non-conservative.

For HIPs, there are configurations which could lead to uni-directional interactions first appearing for clusters of size 4. For clusters of sizes > 5 particles, $\gamma > 1$ at long ranges. This result is in good agreement with our observations of driven HIP clusters. At certain cluster sizes, non-conservative forces appear to allow clusters of particles to propel in an otherwise symmetric initial field. Despite the particles being identical in the simulation, the cluster-particle interaction adds an asymmetry which can drive the system into unidirectional motion in some

cases. Here we study a limited set of configurations due to their common observable presence in the experimental data; however, we expect there are a number of alternative configurations that can also exhibit highly propelled motion. We expect that these strongly non-conservative interactions are cause for the increased average motion in the high light intensity binding experiments (**Fig. 2.9**a,b).

For a similar set of cluster sizes in the LIP case, we find $\gamma < 0.1$ regardless of cluster size (**Fig. 2.10**d). Indeed, we observed in the experiments that LIPs can build themselves into extremely long rods without exhibiting strongly non-conservative responses at small cluster sizes, as we found for the HIPs. It is likely that non-conservative forces won't have a strong presence for LIPs until they've assembled into elongated rods for which we do observe fluctuations in the VMSD values.

2.5 Summary

In this chapter, I presented an experimental method which allows for the study of 3-dimensional and 2-dimensional optical binding of many particles. This experimental approach is a leap from previous experimental accounts which have been typically limited in array size. Within this geometry, we can in study particles interacting in all directions including lateral and longitudinal orientations. For most of the cases in our study, the longitudinal orientation becomes more relevant as the collective self-organizations tend to align particles along the axis of propagation.

I presented a detailed description of the primary apparatus of which was used for the majority of the experiments as well as alternative orientations and methods. Using this apparatus and technique, we performed optical binding experiments for a various sizes and densities. Some of which are presented in this chapter include polystyrene and silica microspheres which range from $ka \sim 1 - 7$. Among these results, which include self-organized lattices on a glass substrate, self-organized particle chains and clusters in 3-dimensions inside a thin sample cell $10 - 20\mu$m, and the formation of elongated particle chains in thicker samples. The bulk of these findings involve complex behavior that can not be predicted from two-body

interactions alone.

Finally I focused attention on a specific case of active colloidal clusters. In comparing low to high index particles – whose two-body interaction is nearly identical apart from overall strength – already demonstrates differences that may arise from N-body interactions. Our results stress how the relative strength of gradient and scattering forces play a role in these systems. For instance, $ka \ll 1$ particles have been shown to experience interesting conservative interactions on complex potential landscapes; however exploring larger ka affords the capability of controlling non-negligible contributions of non-conservative binding forces. It is at this size regime that we are able to find considerable differences between the LIPs and HIPs. In particular, the lower index particles form close packed (or nearly closed packed) chains, while the higher index particles are aligned with the beam, but usually spaced out by several particle diameters. More strikingly, the dynamic behavior of these particles demonstrates effects that can only be explained by considering non-conservative N-body interactions. This is most dramatically demonstrated by the temporary formation of close-packed clusters of 4-5 high index particles, which appear to drive an instability of the system as a whole.

Our results suggest that although optical binding can be used to guide the self-organization of colloidal particles, the effects of N-body forces are critical for the assembly of many-particle systems when their scattering strength is sufficiently strong. Notably, this is distinct from nano-particle assembly with optical binding, in which pairwise forces are generally a good approximation [9]. Potentially, this more complex force landscape offers new possibilities: with proper system design these forces could be used to promote or evade specific configurations or produce driven arrangements with dynamic behavior.

Unfortunately, predicting the behavior of large scale optically bound systems remains a difficult task without a quick and accurate method of computing the forces for a fully coupled N-body system. Efforts on this front can be aided by further experimentation which can validate assumptions regarding N-body and non-conservative effects over a larger parameter space than the current study. In the next chapter, the focus returns to numerical methods in the hopes to generate

a model that can help predict these dynamic behaviors.

Chapter 3

Dynamic Simulations of Many-Body Optical Binding Interactions

3.1 Introduction

The ability to simulate dynamic optical binding effects is important for future research on the subject of optically bound self-assembly. Experimentally, it is difficult to span the available parameter space. Optical binding interactions can be sensitive to a number of parameters including ones inherent to the particles, the medium, and the binding field.

Furthermore, it is hard to systematically generate consistent environments to isolate what mechanism is driving the behaviors. For instance, if we wish to adjust the relative refractive index of polystyrene in water by adjusting the refractive index of the medium, we might have also then inadvertently adjusted the damping conditions. Another example of experimental difficulty, which we directly experienced resided in simply maintaining the same number of particles. I also note that initial conditions might play a considerable role in the dynamics which unfold. This is because the potential landscape for optical binding–insofar as you can represent it as a potentential–is uniquely complex. We saw an example of this in the

previous chapter, in that there is a high amount of fluctuation in systems which differ only in configuration of the particles. A molecular dynamics type simulation could at-least afford us the control to define the initial conditions or keep certain parameters fixed.

Simulations can also be used to make predictions of experimental designs which have yet to be developed. For instance, it might be worth exploring multiple wavelengths of light. Experimentally, this would require the integration of different optical equipment optimized for an alternative field wavelength. This could be a costly approach without the motivation that an additional field will indeed generate useful self-organized structures or behaviors.

Because experimentation is remains relatively difficult optical binding is a relatively unexplored phenomenon. We have only scratched the surface of understanding these relatively simple systems. For example, in the previous chapter we were able to correlate the formation of clusters with increased activity; but there can be a huge number of alternative configurations which become driven. Consider further the added complexity of multi-species colloidal samples, non-spherical colloidal particles, and the use of multiple light sources with different wavelengths. These are just a few of the many areas that remain uncharted in experimental optical binding research which a good model can help motivate.

A few molecular dynamic simulations of optical binding forces have been achieved in the past. One notable is the work of [10] which was achieved using Mie Scattering Theory to study the dynamic self-organization of optically bound dielectric spheres. Most recently, this model was utilized to study the stability dynamics of much larger collections of particles [8]. These studies alone were able to elucidate fascinating dynamic properties of optical binding in various media. One of highlighted results are the formations of stable and quasi-stable arrays in laterally bound configurations. Neither of these simulations include thermal noise nor are they designed to easily integrate optical binding forces within a soft-matter environment.

For our purposes, we sought to utilize the Coupled Dipole Method. CDM offers the freedom to study beyond identical spheres and is generally easier to

make intuitive decisions on approximations. The CDM method is ultimately built upon the work of [11] and [20] and has been used in the study of optical binding in previous computational works [37, 5, 38].

In this chapter, I attempt to understand the underlying mechanisms behind the optical binding force. We wish to untangle effects due to non-conservative forces, multiple scattering, and non-pairwise forces. The common thread between these various phenomena is that all become more important with an increase in scattering strength. Using simulations, we attempt to give a sense of when these forces become relevant and what effects they could have on optically bound systems.

Finally, I focus on the coupling of CDM to a molecular dynamics simulation which includes hard-sphere interactions, thermal noise, and other external forces. The thermal noise and realistic damping make this simulation particularly suited for colloidal self-organization studies. Unlike previous dynamic optical binding tools, we use unique simulation techniques to accommodate thermal fluctuations. We use this model to simulate interactions between small collections of particles and show how tuning parameters change the behavior. I present a promising method which is similar to CDM but can be much less computationally expensive. This involves the method of fundamental solutions (MFS). I show that this method can be utilized as a solution for optical scattering. While it remains undeveloped for optical binding, I share methods used to study another field scattering phenomenon we refer to as acoustic binding. To that end, I give a brief outlook on the similarity of these interactions and what there similarities in dynamics suggest about field driven self-organization in general.

3.2 Multiple-scattering

When two scattering bodies are near each other, the scattered field from one can ultimately be re-scattered by the other. This event can occur multiple times weakening in succession until it becomes negligible. In terms of optical forces, these multiple scattering effects can add small contributions to the force. Using numerical approaches, we can assess where within in the parameter space multiple

scattering is strongest. The reason why multiple scattering is important is that it gives a good sense of when and why N-body forces might become relevant. In many-body systems, N-body forces can generate highly correlated and complex behaviors. The connection between multiple-scattering and N-body forces can be drawn by the following consideration. Strong multiple-scattering suggests that feedback interference is relevant, thus it can be expected many-particle systems will experience similar feedback interference between neighboring particles.

From previous experimentation reported in **§2.3** and **§2.4**, we observed hints of highly correlated behaviors, such as collective motion. Furthermore, in **§2.4** I showed that pairwise forces weren't enough to describe the observed behaviors. We expect that these behaviors are due to feedback mechanisms, such as scattering interference, which act to strongly alter the binding interaction. We found this particularly true of particles aligned along the beam propagation. Thus we also consider how inter-particle distances and orientations play a role in multiple scattering effects. I focus attention on the lateral and longitudinal orientations described in **§1.2**.

So how exactly can we measure multiple-scattering strength? We consider that the CDM code is an iterative method of computing the total field. The initial field, updates the dipole moments and the dipole moments update the field. We can thus relate the number of iterations required to converge to the multiple scattering strength. The degree of convergence is compared for a range of ka and m values. For each point in the parameter space, (ka,m), two particles are placed into a crossed-polarized counter-propagating field and displaced along a lateral axis or a longitudinal axis. At each displacement, the dipole moments are computed after each iteration of the scattering code and compared for convergence to the previous iteration. We average the convergence value, given by:

$$C = \frac{\sqrt{\langle P_i - P_{i-1} \rangle^2}}{\sqrt{\langle P_i \rangle^2}} \tag{3.1}$$

over a range of displacements from d to $d + 3\mu$m, where d is the particle diameter. The results are provided in **Fig. 3.1**. We find that for larger particles multiple

scattering becomes more prevalent. This is not surprising as we know that scattering strength also increases. We also compared the effects of orientation and show that multiple scattering tends to be stronger in the longitudinal configuration.

For two bodies, these multiple-scattering forces can play add to the force, but in a symmetric configuration, effects will tend to cancel out for each object. In asymmetric configurations, multiple scattering can lead to non-pairwise interactions. By considering three bodies, we can imagine that the field scattering interaction between two bodies can easily be manipulated by the position of a third body through multiple scattering effects. In the following section, we look into optical binding for such systems.

3.3 Non-pairwise forces

The optical binding force described so far in the previous sections can be extended to many-particle systems. Theoretically, this can be done by modifying the total optical field to include contributions from each scattering body. For small spheres, one can utilize **Eq. 1.28** to obtain an equation for the force on a single particle from the scattering of N neighboring particles. On the other hand CDM can be used which takes into account multiple scattering effects and particles that fall within sizes that are not restricted to being much smaller than the light wavelength. The presence of multiple scattering can effect fundamental characteristics of the interaction for systems of more than two particles. For instance, consider how the interaction between two objects might be effected by the presence of a third. Through multiple scattering, the scattered field from the third object could ultimately act as field source which mediates additional interactions between the two objects. This additional interaction would be considered a three-body contribution as the force would thus be dependent on the positions of all three bodies in this system.

An important question to ask is: are the forces pairwise? That is, can the force on any object be determined by the sum of two-body forces? The answer to this question tells us a lot about the physics of the entire system. In particular, a

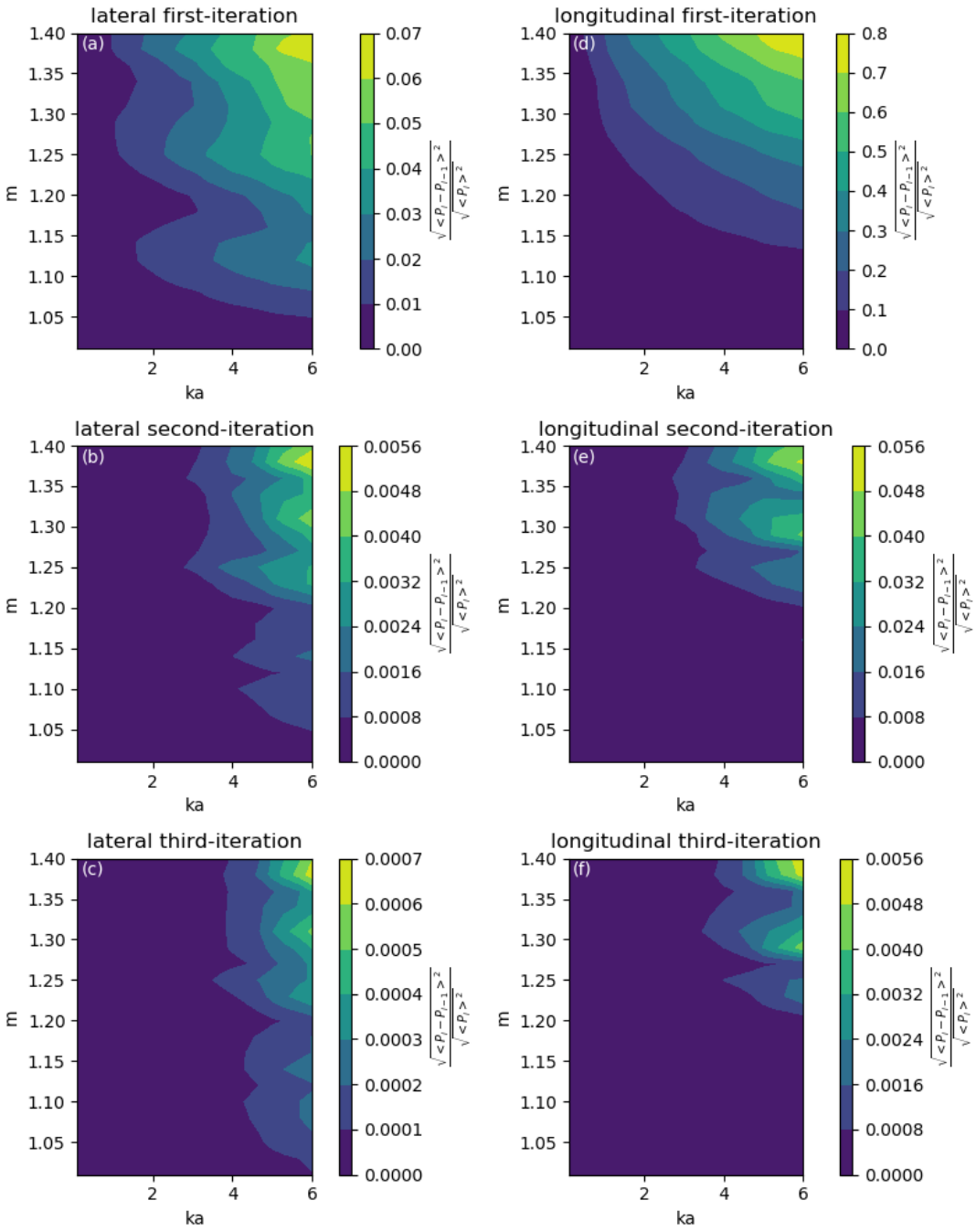

Figure 3.1: Measurement of convergence for subsequent scattering events. Two particles are placed in a CDM simulation. The particles are placed within a $\lambda =$ 400nm and $I = 1$ mW/μm^2 crossed-polarized counter-propagating field in either a **(a-c)** lateral or **(d-f)** longitudinal configuration. The convergence values are determined by taking the root mean squared difference of the dipole moments. The same analysis is performed for a range of inter-particle displacements up to 3 μm and the convergence is averaged over the entire range.

three-body force has a potential to disrupt the stability of a system.

Theoretically, the pairwise and three-body forces can be differentiated by examining how many positions are coupled in the force equation. A pairwise force on a particle from N bodies may generally take the following form:

$$\boldsymbol{F_2} = \sum_{j \neq i}^{N-1} \boldsymbol{F_2}(r_i, r_j) \tag{3.2}$$

where $\boldsymbol{F_2}$ is the total pair-wise force on the ith particle. On the other-hand, a three-body force would have the form:

$$\boldsymbol{F_3} = \sum_{j \neq i}^{N-1} \sum_{k \neq i,j}^{N-2} \boldsymbol{F_3}(r_i, r_j, r_k) \tag{3.3}$$

For optical binding, we can generally write:

$$\boldsymbol{F}_{total} = \boldsymbol{F_1} + \boldsymbol{F_2} + \boldsymbol{F_3} + ...\boldsymbol{F_N} \tag{3.4}$$

The first term are contributions that may arise from first-order optical forces due to the incident field. The second term are the contributions due to pairwise forces and the third term due to three-body forces. Numerically, one can determine the strength of the non-pairwise forces if you can determine $\boldsymbol{F}_{total}$, $\boldsymbol{F_1}$, and $\boldsymbol{F_2}$.

Using CDM, it is quite simple to determine each of these forces. Considering three particles at $(\boldsymbol{r}_0, \boldsymbol{r}_1, \boldsymbol{r}_2)$, we can run a simulation with a particle placed at $\boldsymbol{r}_0$ to determine F_0, two simulations with particles placed at $(\boldsymbol{r}_0, \boldsymbol{r}_1)$ and $(\boldsymbol{r}_0, \boldsymbol{r}_2)$ to determine $\boldsymbol{F}_{0,1} + \boldsymbol{F}_0$ and $\boldsymbol{F}_{0,2} + \boldsymbol{F}_0$ respectively and place particles at $(\boldsymbol{r}_0, \boldsymbol{r}_1, \boldsymbol{r}_2)$ to determine $\boldsymbol{F_{total,0}}$. We can then determine the three-body contribution on particle at $\boldsymbol{r}_0$ by:

$$\boldsymbol{F}_{0,1,2} = \boldsymbol{F}_{total,0} - \boldsymbol{F}_0 - (\boldsymbol{F}_{0,1} + \boldsymbol{F}_0) - (\boldsymbol{F}_{0,2} + \boldsymbol{F}_0) + 2\boldsymbol{F}_0 \tag{3.5}$$

The extra $2\boldsymbol{F}_0$ accounts for the two simulations which add an extra single body contribution each.

We can assess the three body force for a lateral and longitudinal case for simplicity. Starting with the lateral case, we place three particles along the x-axis

with a cross-polarized counter-propagating beam along the z-axis. The particle locations are ($\boldsymbol{r}_0 = [0,0,0]$, $\boldsymbol{r}_1 = [r_{0,1}+d,0,0]$, $\boldsymbol{r}_2 = [r_{0,1}+r_{1,2}+2d,0,0]$) where $r_{i,j}+d$ is the center-center distance between particles i and j and d is the diameter of the particles. To determine the three body force on the particle located at the origin requires four separate simulations: (1) single particle located at the origin ($\boldsymbol{r_0}$), (2) two particles at $\boldsymbol{r_0}$ and $\boldsymbol{r_1}$, (3) two particles at $\boldsymbol{r_0}$ and $\boldsymbol{r_2}$, and (4) three particles at $\boldsymbol{r_0}$, $\boldsymbol{r_1}$, and $\boldsymbol{r_2}$.

Fig. 3.2 shows a comparison between using the total force versus the pairwise approximation for $ka = 1, 2.5, 4$. For the full force (**Fig. 3.2**a-c), we can observe a complex relationship between the three particles. Most importantly, I note that the force is sensitive to the positions of both particles and can oscillate in stability from long range contributions from $\boldsymbol{r_1}$ and $\boldsymbol{r_2}$. Consider, for instance **Fig. 3.2**a with $r_{0,1} = 0.2\mu$m how the force oscillates between positive and negative as $r_{1,2}$ changes.

Fig. 3.2d-f shows that the pairwise forces are an extremely good approximation even at close range for this orientation. Not until taking the difference between the two forces can you observe what the three-body contribution looks like (**Fig. 3.3**). Taking the average strength of the difference divided by the average strength of the force, we obtain an 0.9% three-body contribution for $ka = 1$, a 3.7% contribution for $ka = 2.5$, and a 21.2% contribution for $ka = 4$. Despite the contribution being large, it doesn't do much to fundamentally change the form of the force for $ka = 4$ within this specific configuration. Looking closely at **Fig. 3.2**c,f, we can observe a slight shift in phase along the x-axis between the two plots.

For the longitudinal case, we can perform the same analysis for particles that are aligned along the z-axis. **Fig. 3.4** shows the difference between the full force calculation and a pairwise approximation. In this configuration, unlike the lateral case $ka = 2.5$ and $ka = 4$ show noticeable differences in the force. **Fig. 3.5** we observe the three-body contributions for longitudinal binding. For the various sizes, $ka = 1, 2.5, 4$, we find that the average contribution is $3.1\%, 10.7\%$, and 15.1% respectively. More importantly however is that this force appears to be doing more than altering the phase of the oscillatory behavior. For the $ka = 2.5$

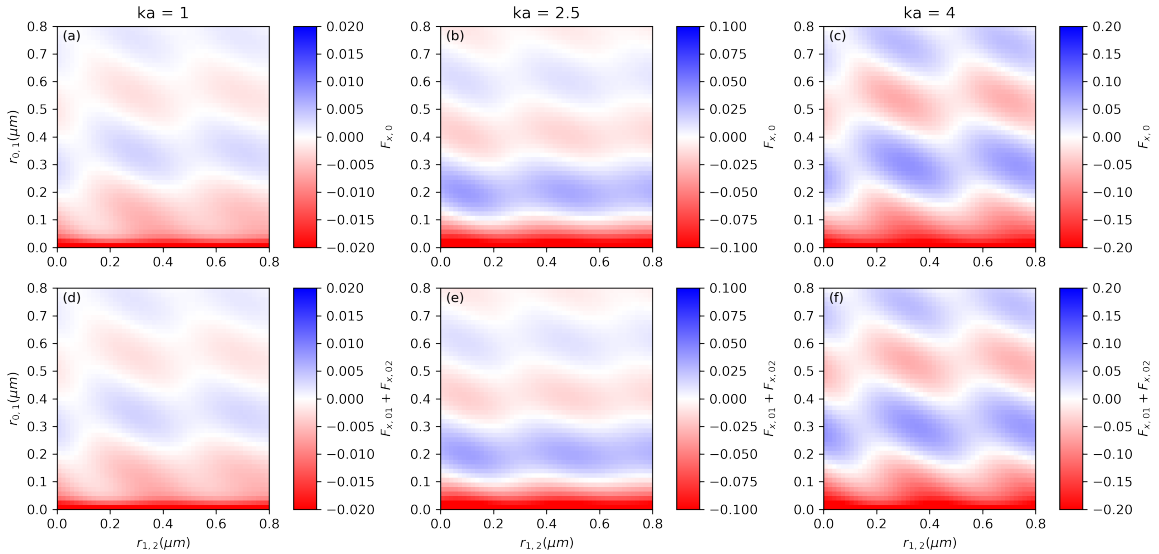

Figure 3.2: Three particles are placed along x-axis perpendicular to cross polarized counter-propagating beam along the z-axis. The full force on a single particle of size **(a)** $ka = 1$, **(b)** $ka = 2.5$, and **(c)** $ka = 4$. The pairwise approximation of **(d)** $ka = 1$, **(e)** $ka = 2.5$, and **(f)** $ka = 4$. $r_{i,j}$ is the distance between particle i and j displaced perpendicularly to the field propagation.

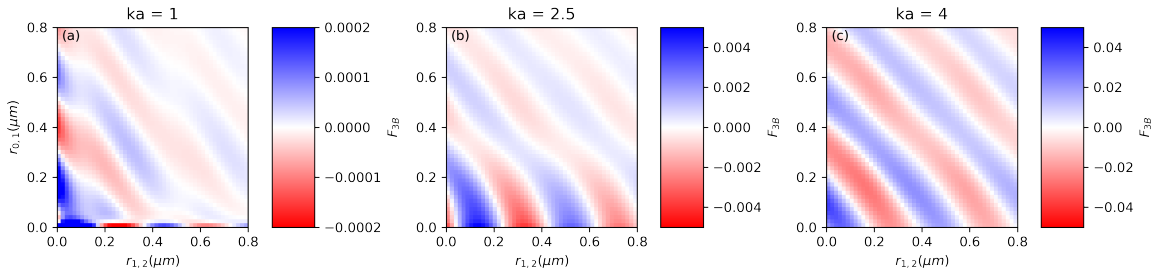

Figure 3.3: The three-body force on a single particle of size **(a)** $ka = 1$, **(b)** $ka = 2.5$, and **(c)** $ka = 4$. $r_{i,j}$ is the distance between particle i and j displaced perpendicularly to the field propagation.

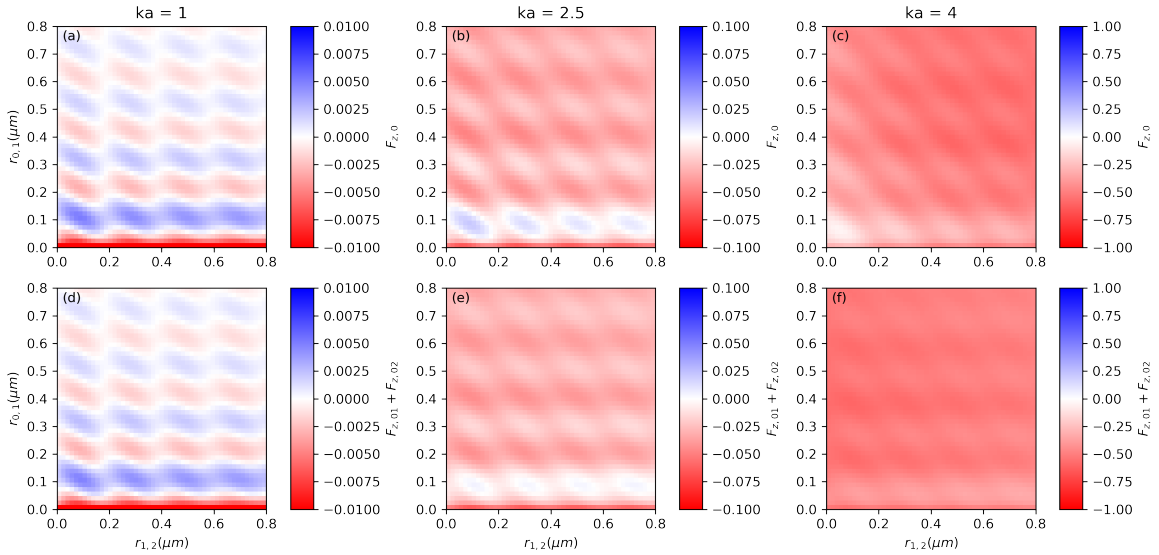

Figure 3.4: Three particles are placed along x-axis perpendicular to cross polarized counter-propagating beam along the z-axis. The full force on a single particle of size **(a)** $ka = 1$, **(b)** $ka = 2.5$, and **(c)** $ka = 4$. The pairwise approximation of **(d)** $ka = 1$, **(e)** $ka = 2.5$, and **(f)** $ka = 4$. $r_{i,j}$ is the distance between particle i and j displaced parallel to the field propagation.

and especially the $ka = 4$ case, we see that the three-body force introduces a positive force when particles are close which does not appear in the pair-wise approximation. We can see that this positive force alters **Fig. 3.4**f to be slightly less negative when particles are in close-range (**Fig. 3.4**c). This is a very important finding in that it illustrates that there are indeed significant many-body forces at larger particle sizes and that in the longitudinal orientation, the many-body force can strongly disrupt the expected behavior from a pairwise approximation. In certain configurations the pairwise force might predict repulsion where the three-body force is actually acting to keep particles bound together. In the following chapter, we experimentally observe the effects of these short-range forces through the formation of longitudinally bound clusters.

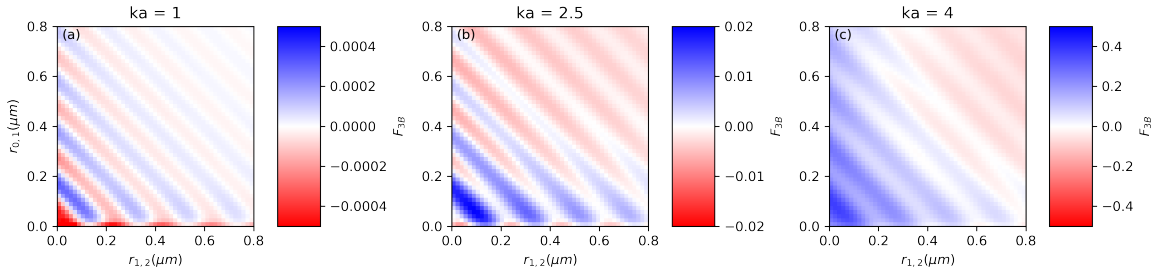

Figure 3.5: The three-body force on a single particle of size **(a)** $ka = 1$, **(b)** $ka = 2.5$, and **(c)** $ka = 4$. $r_{i,j}$ is the distance between particle i and j displaced parallel to the field propagation.

3.4 Determination of when three-body forces become relevant

So far, I have shown that the optical binding force is a combination of conservative gradient forces and non-conservative scattering forces, that the two body force is long range can have multiple stable points, and that there can be significant non-pairwise binding forces. I have also shown that the contributions can be easily tuned based upon the properties of the particles, the light, and the geometry. Using fairly simple numerical techniques, we can understand a great deal about the optical binding force; however the configuration space has proven still to be too large to generalize the behavior. The previous analysis remains too costly to explore optical binding at a higher resolution.

A simple approach involves a stochastic sampling of three-body configurations. By collecting a large enough sample of, one can determine the general strength of three-body forces without exploring the entire configuration space which scales in dimension like $\sim 3N$ for N particles. We can tune one parameter such as ka and measure how well the pairwise approximation fits the total force. By obtaining a fit of the pairwise approximation versus the total force for a number of randomly chosen configurations, one can determine by the value of the slope and the correlation number the accuracy of the pairwise force. **Fig. 3.6** shows how the slope and correlation number for various values of ka. What is interesting from this data is that it suggests that in general the two-body approximation is a fairly good

approximation until $ka \gg 1$. By plotting the values for each randomly selected configuration, we see that the fitness two-body approximation is strongly dependent on the specific configuration. In many cases the error can range in orders of magnitude. This validates our intuition that many-body behaviors are driven by how a specific orientation of particles interact with the light field. However, from **Fig. 3.5** the longitudinal case, we observed much larger three-body contributions. We thus performed a second set of randomly chosen configurations with the restriction that the three particles reside along the axis of the field propagation. **Fig. 3.6** shows that the pairwise approximation performs generally more poorly for these longitudinally aligned particles. The presence of three-body forces having such a strong dependence on this specific longitudinal orientation would be an inexplicable finding if not for the strong scattering component which also acts along this axis.

Unlike pairwise forces between identical particles, three body forces can be non-reciprocal and thus generate net forces which can lead to driven motion. While so far the focus has been on three particles and we haven't yet stumbled upon strong driven forces, I note that many-body systems interacting via three-body forces or even N-body forces can indeed exhibit emergent properties.

3.5 Discrete Dipole Approximation Coupled Molecular Dynamics

Coupling scattering code to a molecular dynamics simulation is an essential step in characterizing the self-assembly behavior of optically bound systems. In typical molecular dynamics simulations one can rely on a potential function as an inter-particle interaction term. Unfortunately, writing down an optical binding potential would cause the loss of interesting physics. Primarily, writing the optical binding force as a potential would neglect relevant non-conservative contributions which we have shown to be be important in the Mie regime. Aside from non-conservative forces, it also remains unclear how to represent many-body forces which also appear to become relevant in the Mie regime. Without the ability to

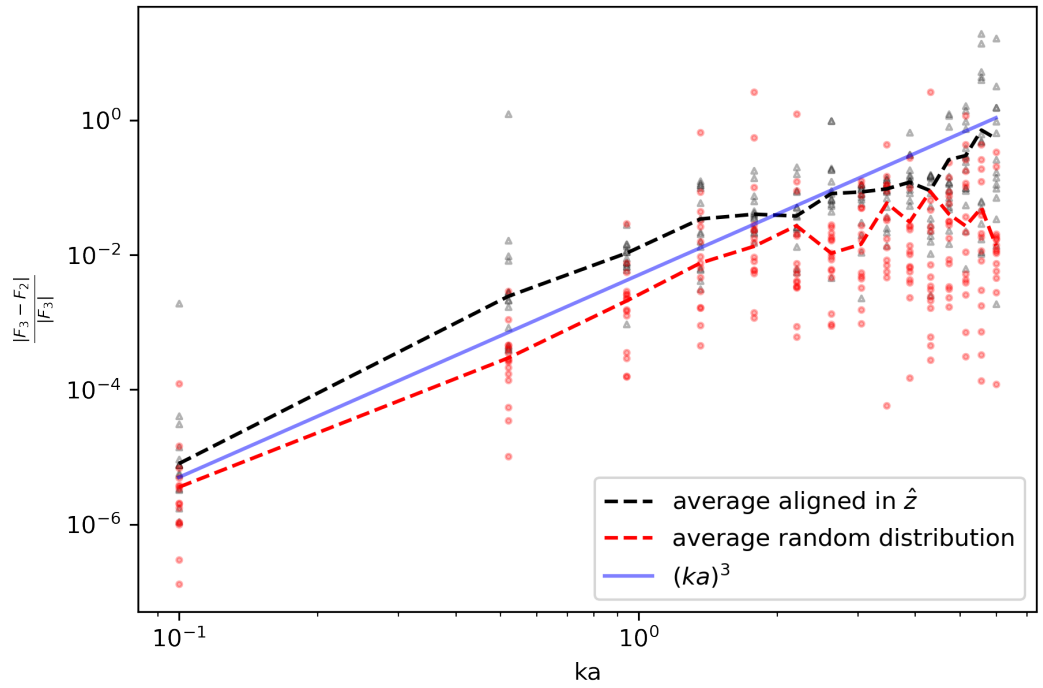

Figure 3.6: The error associated approximating the total force, F_3, with a two-body approximation, F_2, for various randomly distributed configurations. One set of random configurations (black) were done for particles which were confined along the $\hat{\boldsymbol{z}}$-axis and the other set (red), were randomly placed in 3-dimensions. For this analysis, we focused on particles with a relative refractive index of $m = 1.2$ and altered the size parameter ka

reduce optical binding to a potential nor an analytical forces which can be applied to many body systems, there is not a clear way around the necessity of computing the entire field at each time step. This process is by far the most computationally expensive portion of the simulation. The Discrete Dipole Approximation (DDA) utilizes a finite array of polarizable points in a volume to approximate an object. Starting with the incident field, one can calculate the polarization at each dipole,

$$\boldsymbol{P}_0(r) = \alpha \boldsymbol{E}_{inc}(r) \tag{3.6}$$

with,

$$\boldsymbol{E}_{inc}(r) = \boldsymbol{E}_0(r) + \sum_i \overleftrightarrow{\boldsymbol{G}}_i(r, r_i) \cdot \boldsymbol{P}_i(r_i) \tag{3.7}$$

where $\overleftrightarrow{\boldsymbol{G}}$ is the dyadic Green's function which appeared in **§1.2**. Each subsequent scattered field and polarization can be iteratively solved.

The effective size of the dipole depends on the overall scale of the system and is determined primarily by the dipole density. Traditionally, 10 dipoles/wavelength have been found to be an appropriate approximation. In certain cases, we find that the simulations converge with less. For reference, a particle of size 500 nm in diameter in a 400 nm field, the approximate size used in the analysis in **§2.4** would thus require ~ 1000 dipoles for each particle. However, simply doubling the size of the particles requires 8000 dipoles. In terms of time resolved simulations, this iterative solution would have to be performed at each time-step. An average simulation of two optically bound particles using 1000 dipoles is $\approx .5$s while 2000 dipole simulation is ≈ 2. In general we find that the computation time of each step scales with the total number of dipoles squared. For this reason, it can get extremely costly to run simulations for many-particle systems.

Beyond the calculation of the total field, the force on each dipole can also be determined by taking the total sum of the forces on each dipole,

$$\boldsymbol{F} = \sum_i^{n_{dipoles}} \boldsymbol{P}_i \cdot \boldsymbol{\nabla} \boldsymbol{E}_i \tag{3.8}$$

For the other contributions to the equation of motion, we require a force that will keep particles from overlapping and we require a drag coefficient. Using the

assumption that the particles are in a relatively high friction environment like water, we can write down the equation of motion:

$$\Delta \boldsymbol{x} = \frac{D}{k_b T} \boldsymbol{F}_{O.B.} \Delta t + \Delta \boldsymbol{x}_{P.F.H.S} \tag{3.9}$$

$F_{O.B.}$ is the binding force, D is the drag coefficient, k_b the Boltzmann constant, and T room temperature. The second term is the Potential Free Hard-Sphere given by [39],

$$\Delta \boldsymbol{x}_{P.F.H.S} = \begin{cases} -\kappa(d-r)\hat{\boldsymbol{r}}, r < d \\ 0, \qquad\qquad\qquad \text{otherwise} \end{cases} \tag{3.10}$$

which displaces particles proportionally to their overlap distance. a value of $\kappa = 0.5$ ensures that the particles of diameter, d, will be set back to contact distance. It is more typical to find a soft-sphere potential in use; however the scattering code cannot support any amount overlap. In practice, we add a padding of 1-2% to the diameter to ensure that dipoles are not touching.

While the $\boldsymbol{F}_{P.F.H.S}$ solves the overlap issue with a straight-forward way to separate a pair of overlapped particles, at high densities, we may not be able to resolve each overlap in one pass. Consider, for instance, the the hard sphere force separates two particles from touching, but generates a new overlap in the process. Thus, in the code we iteratively scan the system for overlapping particles. The code is designed to raise error if there remains overlapping objects before the next time-step in the simulation. With appropriate choice of padding and sufficiently small time steps, we find that the overlaps can be avoided in practice.

Additionally, we can include thermal motion:

$$\Delta \boldsymbol{x}_T = \sqrt{2D\Delta t}\boldsymbol{R}_{norm} \tag{3.11}$$

where $\boldsymbol{R}_{norm}$ is a random vector selected from a normal distribution centered at zero. **Eq. 3.11** can be added to **Eq. 3.9** The choice of Δt is usually dependent upon the maximum displacement which can be obtained by **Eq. 3.11**. The maximum displacement certainly should be much less than the radius of a single particle. The same criteria should be met for the optical binding contribution; however, unlike the thermal contribution, there is not a straight forward method

to determine what the maximum binding force *is*. Therefore, we base Δt purely on the thermal noise and adjust if errors arise due to large optical binding forces. Again, thermal motion is random, thus there is a high chance of particles randomly overlapping. As an additional measure to avoid overlap as much as possible, we perform the random motion and if overlapping occurs after the time-step, we simply generate another random distribution. To avoid complications at high densities, an arbitrary number of iterations are applied in this manner.

One concern with this procedure is that there could be a bias added when throwing out random distributions which break the simulation by causing overlap. In this case however, the only bias is against random selections that cause overlap and, in a sense, simply acts as a Psuedo-Hard-Sphere interaction. It is otherwise ensured that all positions outside of overlapping regions remain unbiased by this process.

By utilizing the steps above, we have at the least a very good method to model small systems for short time periods. While the model is computationally costly, it does not rely on approximations which remove fundamental aspects of the optical binding interaction. In a very fundamental way, we retain the computation of the field and directly compute optical forces on the system of particles. Furthermore, in this current development, it is relatively straightforward to explore non-spherical objects which is a largely undeveloped area in optical binding studies. In the following section, I have focused on small scale simulations of spherical dielectric particles.

3.6 Many-body Optical Binding Simulations

3.6.1 Lateral 2-body

The simplest and most studied configuration in optical binding are two laterally bound particles. In this configuration, we expect to find particles bind into stable displacements which correspond to the wavelength of light. By simulating thermal noise, we should be able to observe that particles exhibit multistability.

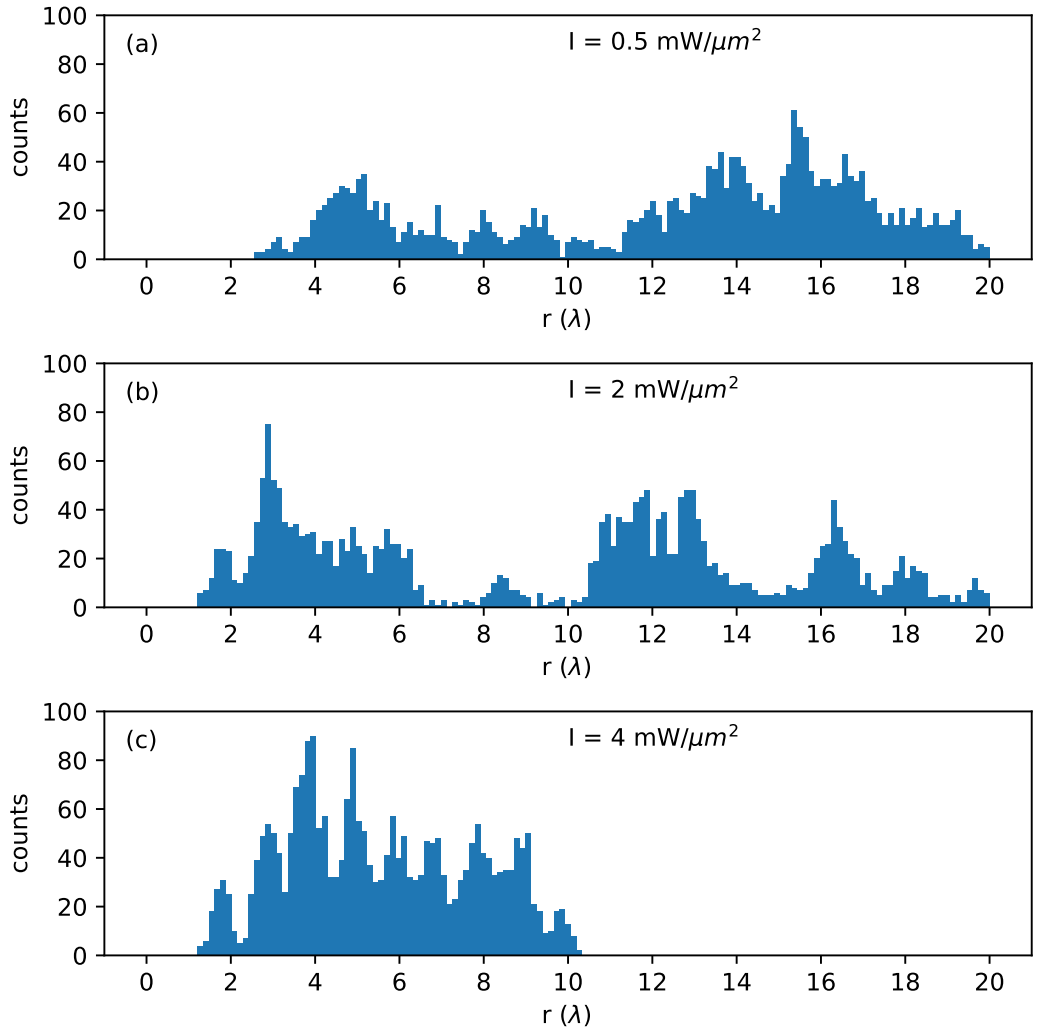

Figure 3.7: The distribution of inter-particle separations for two 500 nm polystyrene spheres placed in a 400 nm cross-polarized counter-propagating field of intensity **(a)** $I = 0.5$ mW/μm^2, **(b)** $I = 2$ mW/μm^2, and **(c)** $I = 4$ mW/μm^2

.

Furthermore, by adjusting the field intensity, we should be able to determine when the binding force is expected to overcome thermal effects. For the first analysis, we place two particles in a crossed-polarized counter-propagating field. The field is set to propagate along the z-axis. To ensure particles remain laterally displaced, we restrict their motion in z but allow them to move around freely within the xy-plane. In the presence of thermal noise, we can observe how the two particles interact. **Fig. 3.7** shows the distribution of particle displacements over a 5 second interaction for various power densities. In just a short time period, we can observe clear signs of optical binding with $I > 2$ mW/μm^2. The particles in the simulations reported here are of size parameter $ka = 4$ and relative index $m = 1.2$. These values are set to coincide with the 500 nm polystyrene spheres presented in **Chapter 2**. In **Fig. 3.7**c, we observe the signs of a periodic multi-stable configurations with λ spacing. These results, coincide with what is expected in two-body lateral binding.

3.6.2 2-body along a lateral and longitudinal axis

Longitudinal binding has typically been observed experimentally in 1-dimension [26, 4, 40]. In **§2.3**, we observed a system undergoing both longitudinal and lateral binding forces and found that longitudinal effects tend to dominate with $ka > 1$ particles. Computationally, we can simulate particles interacting with both lateral and longitudinal binding forces. For the longitudinal 2-body, we restricted particles to the xz-plane with the counter-propagating field propagating along the z-axis. At the specific size range of interests, we know that the forces along the propagation direction for two-bodies will tend to be repulsive, we also add a boundary of 20 μm similar in dimension to the thin sample tube utilized in the experimental collection described in the previous chapter. Furthermore, since the interaction is not symmetric in the plane, instead of collecting a 1-dimensional radial distribution as was done in the lateral case above, we opt for generating a 2-dimensional histogram of displacements.

In, **Fig. 3.8** we can observe that the thermally active colloidal spheres of $ka = 4$ and $m = 1.2$ interact such that preferred displacements are non-uniform

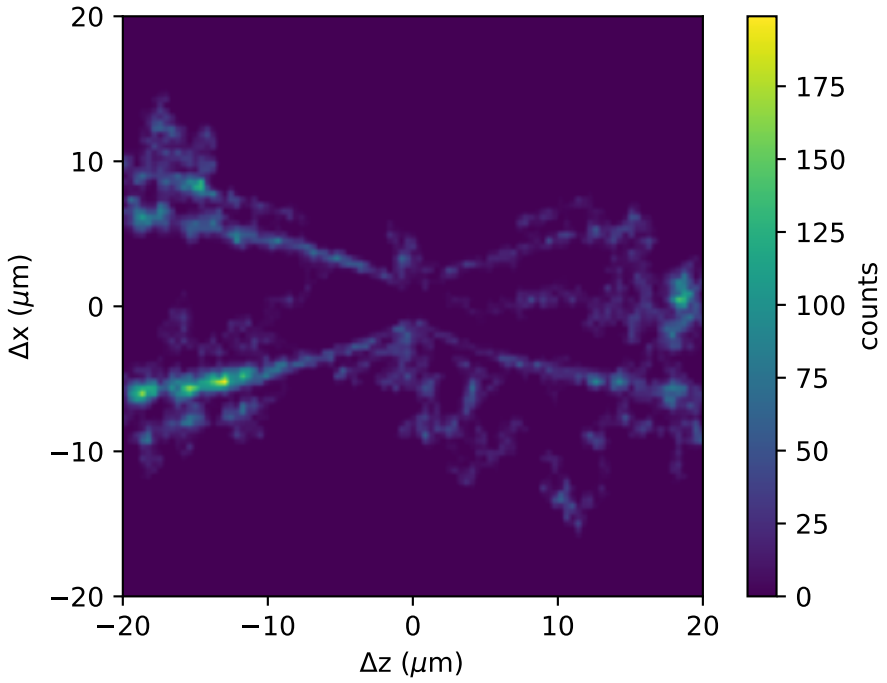

Figure 3.8: 2-dimensional histogram of displacements between the particles confined to the xz-plane of a counter-propagating beam propagating in the z-direction. The beam wavelength is 400 nm and power set to 2 mW/μm^2.

and match the scattering pattern of a single particle. With a small amount of randomly initiated simulations (20 runs of 5 seconds each) we can observe strong evidence of optical binding. A similar plot was generated with experimental data of many particles in **§2.4**. While there is evidence of the two particles aligning along the beam propagation, it is much weaker than what would be expected in the binding experiments. One likely explanation is that since the particles were seeded randomly, they have a higher chance of starting far from the aligned axis than they do already near alignment. Thus, starting far from the axis of propagation, the other off-axis optical binding forces are strong enough to keep particles from reaching alignment. In the experiments, we start with a density high enough such that particles are already near the axis of propagation and chain can begin to form. When multiple chains of particles form, we notice a similar barrier which eventually keeps chains apart.

3.6.3 Lateral 3-body

Similar to the static simulation approaches in **§3.4** where we initiated the particles in random configurations, we begin the dynamic simulations in a similar fashion. Optical binding forces are highly dependent on the initial configuration and the configuration space is far too large to explore completely. Therefore, we can generate a random set of three-body configurations and observe a few of the dynamic pathways to get a sense of what behaviors are possible. What we are looking for in particular, are signs of stability and activity. Do particles assemble into static, drifting, rotating, or quasi-stable structures? For the first cases, we focus on the lateral orientation. Furthermore, we run these simulations without thermal noise. Not including thermal forces in this section helps us determine the precise role that optical binding forces are playing.

In this computational process, we randomly orient three particles on the xy-plane inside a counter-propagating field propagating along the z-axis. We let the particles interact for 0.5 seconds and record positions, center of mass, and moment of inertia. Since all particles are identical, we treat the masses as equal to 1 (a.u.). From the position data, we also track the velocity and the squared velocity

of each particle. In a non-active system, as particles interact, we should expect that the total squared velocity of each particle would decrease; however in this field driven system, where particles can borrow momentum from the light field, we track the total squared velocity to determine what direction it is going. For comparison, we repeated this analysis for three sizes ($ka = 1, 2.5, 4$) and two relative refractive indices at each size ($m = 1.1, 1.2$) Utilizing the same set of initial random configurations for consistency, we can directly compare how the dynamic evolution changes with size and relative index.

For the smaller particles ($ka = 1, 2.5$), we did not find clear evidence of driven clusters. Thus, I present results on the case in which we explicitly found the presence of driven clusters using this analysis. To tie this analysis to the bigger discussion on the effects of relative refractive index and scattering strength, I compare the results for $ka = 4$ sized particles with a relative refractive index of $m = 1.1$ (**Fig. 3.9**) and $m = 1.2$ (**Fig. 3.10**). Starting with the low-index particles (LIPs), we found that particles quickly interacted to form stable clusters (**Fig. 3.9**). When stable, we find that generally the particles don't move collectively (ex. '6c' and '2f' from **Fig. 3.9**). Certain, systems failed to stabilize in the short time of the simulation; in these systems, we find that the particles within the system tend to have different velocities indicative of a system still out of equilibrium.

The higher-index particles (HIPs) exhibit a more diverse set of behaviors amongst the clusters. In this case, HIPs can form static structures (ex. '5d' and '2f' from **Fig. 3.10**) as well as structures which exhibit collective motion (ex. '3f','1b', and '5e' from **Fig. 3.10**). Again, to distinguish from systems in which particles are moving collectively is that .

In both cases, we observed that particles that are not initially in a stable state will reorient themselves relatively quickly into a more stable orientation. Because, we did not want to under-represent the speed of low-index clusters due to the fact that optical binding forces are expected to be $\frac{(1.2-1)^2}{(1.1-1)^2} = 4$ times weaker and the speed should be proportional to the force, we multiplied the velocities by a factor of 4.

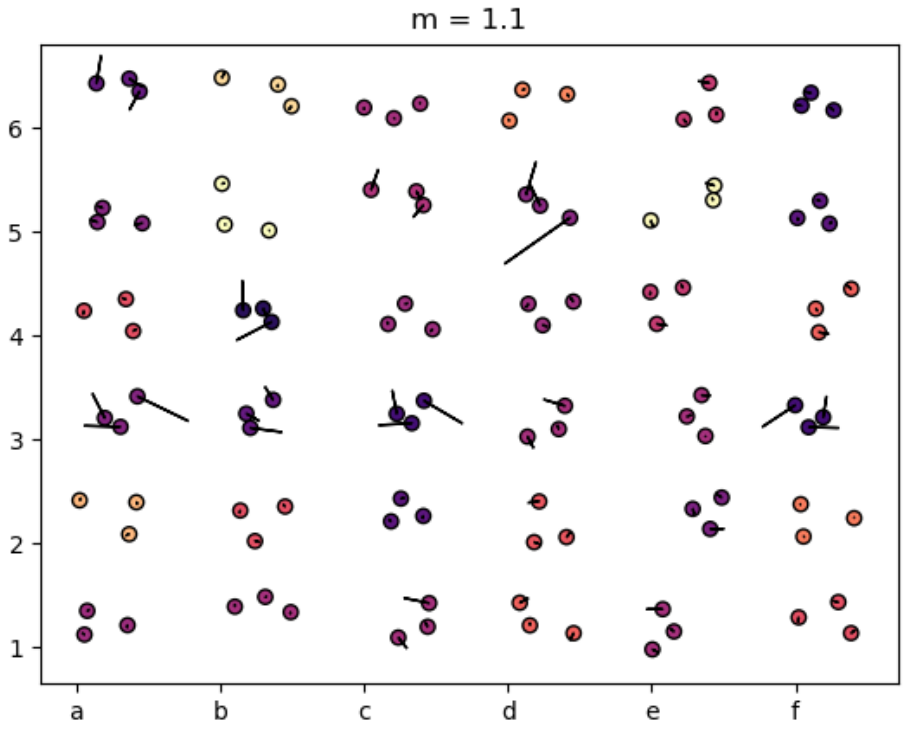

Figure 3.9: Collection of three-body simulations. Each cluster of particles are shown after 0.5 seconds of interacting through optical binding forces and particle positions are initiated at random. Particles of size $ka = 4$ are confined to the xy-plane perpendicular to the propagation of a crossed-polarized counter-propagating beam of $\lambda = 400$ nm and $I = 2$ mW/μm^2. For each particle, the velocity is represented by an arrow. The color of the cluster is designed to signify the total moment of inertia such that clusters of similar structure can be easily identified. The title of each cluster is provided by the axis labels (for example: the cluster on the top left is '6a').

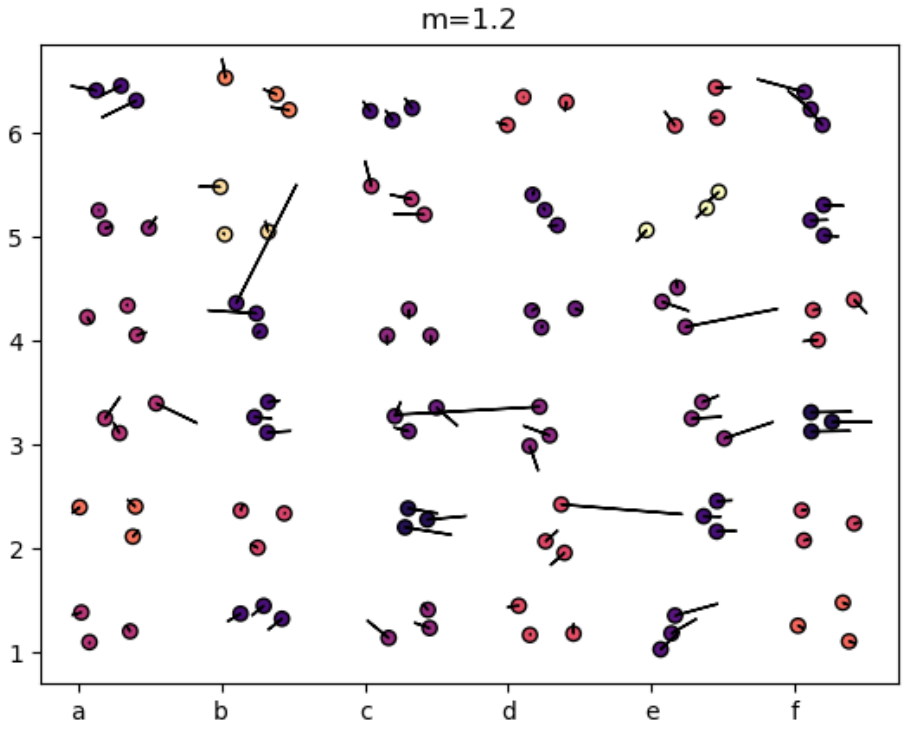

Figure 3.10: Collection of three-body simulations. Each cluster of particles are shown after 0.5 seconds of interacting through optical binding forces and particle positions are initiated at random. Particles of size $ka = 4$ are confined to the xy-plane perpendicular to the propagation of a crossed-polarized counter-propagating beam of $\lambda = 400$ nm and $I = 2$ mW/μm^2. For each particle, the velocity is represented by an arrow. The color of the cluster is designed to signify the total moment of inertia such that clusters of similar structure can be easily identified. The title of each cluster is provided by the axis labels (for example: the cluster on the top left is '6a').

3.7 Active clusters

The previous section gave us a hint of where to look for driven clusters. These clusters we denote as driven are systems of particles in which the relative displacements are stable but the system remains out of equilibrium. Previous numerical studies of optical binding have found such configurations in non-thermal systems [10]. Namely they observed instances of drifting equilibrium structures. These observations raise multiple questions: What do the presence of driven clusters do to the overall stability of larger systems? Can optical binding be used to form an active material? Can any of these driven behaviors be tuned?

In this section I highlight one such active cluster of three particles which shows how the driven behavior can be tuned. For a system of three particles, the number of stable active clusters that can be formed remains unknown as the possible configuration space is extremely large. This remains even more true as the number of particles increase. Furthermore, in the presence of thermal noise, the multistability associated with optical binding might represent a competing source of instability [38]. Thus, for this section I remove thermal noise to focus on instabilities driven purely by non-conservative optical binding forces.

Searching for driven clusters is a problem on it's own. Other than asymmetry, we do not have a good sense of what makes one optically bound cluster more active than another. However, using the technique described in the previous section, we can test multiple random configurations until we find one which exhibits driven behaviors. For this discussion, I focus in the lateral configuration; although, in theory, the same analysis can be applied in 3-dimensions (we have yet to discover a 3-dimensional structure in equilibrium without the use of a boundary). I also limit our current discussion to particles with $ka = 4$ which is consistent with much of the analysis presented within this thesis.

The first numerical simulation was performed by placing three particles in a configuration that was discovered near a drifting equilibrium. In **Fig. 3.11**a, I show the cluster of three particles which exhibiting drifting equilibrium in the direction coinciding with the polarization of the counter-propagating beam. Over

the 2-second simulation, the velocity of the cluster settles to a constant value. As can be determined by the plot, the cluster moves at $\sim 1\mu$m/s. The beam intensity used in this simulation is 2 mW/μm^2, but the cluster speed should also be controlled proportionally to the intensity of the field. We find that the direction of motion can be controlled by the polarization of the beam. For example, we observe the same system under a counter-propagating field polarized in the $\hat{\boldsymbol{y}}$ direction. Here, the clusters motion is virtually stopped. We have examined this particular cluster at various orientations, and find that the cluster will tend to rotate towards the polarization axis. Here we observe a way to externally control the direction of a stable bounded cluster. In **Fig. 3.11**c and **Fig. 3.11**d we visualize the field and show how the distribution of scattered light differs when the incident polarization is rotated by 90°.

In the second numerical analysis on the tunability of the active cluster, we look at the dynamic behavior for various values relative refractive index. We choose a range from 1.05 - 1.25 and initialize the configuration of particles at the same positions and run a 2 second simulation. By fixing the force at 2 mW/μm^2, we find that the equilibrium structure and the drifting behavior remains a consistent feature despite the relative refractive index. The main difference that is found is that the speed of the cluster increases **Fig. 3.12**a. Some proportion of that increase is expected to be due to the fact that the force strength tends to scale linearly with relative refractive index. In Chapter 1, I showed that the strength scales with $(m-1)^2$. To compare these systems more directly, we should adjust the intensity of the field such that the scattering forces are equally strong. We can effectively achieve this adjustment by dividing the speeds, which scale linearly with the force, by $(m-1)^2$. I present this corresponding plot in **Fig. 3.12**b

This analysis shows that the speed and direction of active clusters can be tuned by various means. By adjusting the polarization, for instance, we find that the equilibrium structure can be rotated and directed along the polarization. In the lateral orientation, we find that driven behaviors are observable for a large range of m.

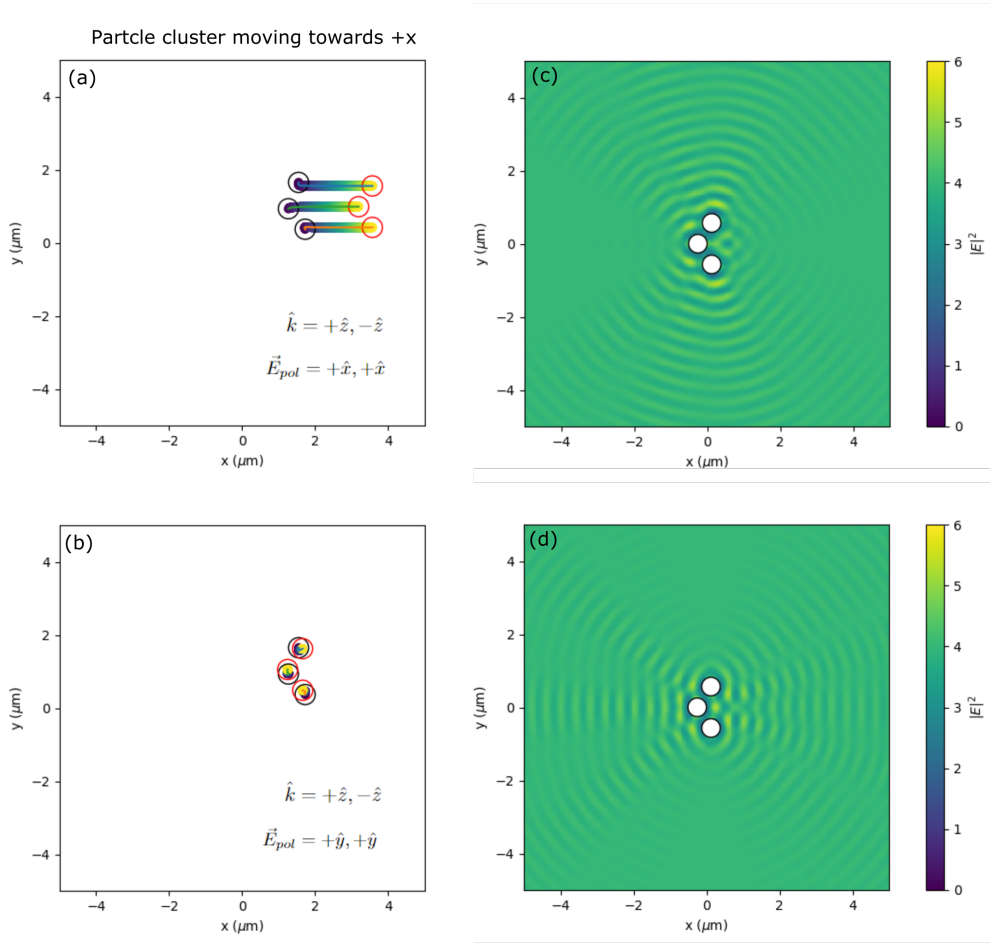

Figure 3.11: Cluster responding to field polarization. **(a,b)** Stable cluster trajectory in counter-propagating field with polarization in **(a)** $\hat{\boldsymbol{x}}$ direction versus polarization in the **(b)** $\hat{\boldsymbol{y}}$ direction. **(c,d)** the total field intensity surrounding the clusters in the xy-plane for **(c)** $\hat{\boldsymbol{x}}$ polarized and **(d)** $\hat{\boldsymbol{y}}$ polarized field. In both cases, the wavelength of the field is set to 400 nm with a power density of 2 mW/μm^2

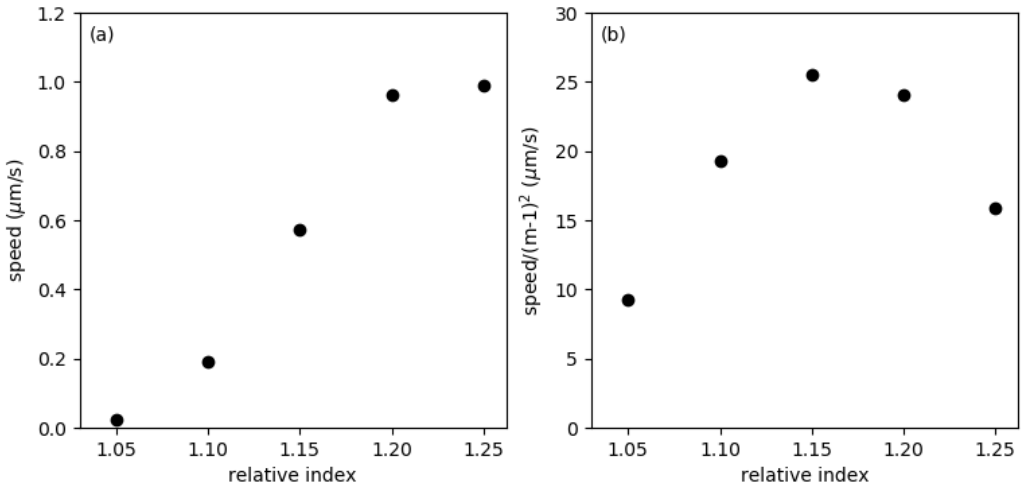

Figure 3.12: Three-body cluster speed for various values of relative refractive index. **(a)** using a fixed force strength the speeds are compared for particles of different relative refractive index. **(b)** The speeds are normalized by $(m-1)^2$ to account for speed increase due to stronger scattering forces.

3.8 Method of fundamental solutions

In the previous sections of this chapter we've utilized DDA coupled with molecular dynamics to study a limited set of many-body optical binding configurations. This has so far only been a small bit of the vast behaviors that are possible with optical binding forces. Unfortunately, computational costs remain the largest barriers towards taking longer simulations with more particles. Much of the cost is due to the fact that scattering calculations must be made, and this is mostly unavoidable. However, some of the cost with DDA involve the number of dipoles required to fill the volume of the object. In this section, I introduce a method which can provide the scattering calculation with the use of scattering points placed on the particle surface [41]. While this method has yet to be developed for the dynamic simulation of optical binding interactions, I describe in this section the use of this computational technique on a similar scalar field scattering phenomena. The development of this computational technique for vector fields remains a goal for future work.

The method of fundamental solutions (MFS) is a product of Huygen's principle. This principle states that all points in a wavefront can be treated as a point source

of a spherically expanding wave. A total field can thus be represented as a sum of appropriately weighted fundamental solutions. Taking an arbitrarily shaped object and appropriate number and placement of source points placed along (very-near) the surface of that object can generate a approximation of the total field. The fundamental solution of the point source can be represented as

$$g(r, r') = \frac{e^{ik|r-r'|}}{4\pi|r-r'|} \tag{3.12}$$

which is defined everywhere, except $r = r'$. These leads to a theoretical requirement that to describe a field in a certain domain, the source points must be placed outside of it. In practice, this means that to describe the field everywhere around a particle, the source points are to be placed inside of the particle; likewise, to compute the field inside of a particle, one can place source points just outside of the particle.

Numerically, one can choose a set of evaluation points to solve for the weights in the equations, $(r_j, j = 1, ..N)$. Using the boundary conditions specific to the problem, one can generate a system of equations.

3.9 Acoustic Binding (MFS)

While we have yet to develop a molecular dynamics simulation utilizing MFS for optical binding forces; in this section, I briefly share work done on a comparative force known as acoustic binding. Like optical binding, acoustic binding is a field driven inter-particle force due to the scattering of acoustic fields. Despite the fact that acoustic binding and optical binding are relevant effects at different length scales, optical binding in the nm and μm scale and acoustic binding in the mm scale, they share many similarities. One of the major similarities between these forces are the dependence on the wavelength of the incident optical or acoustic field and the dependence of on the size parameter. Similarities additionally include the presence of non-conservative and conservative forces as well as multiple scattering effects including many-body interactions. To highlight the similarities between the two forces, we can look at how there respective force maps compare for various

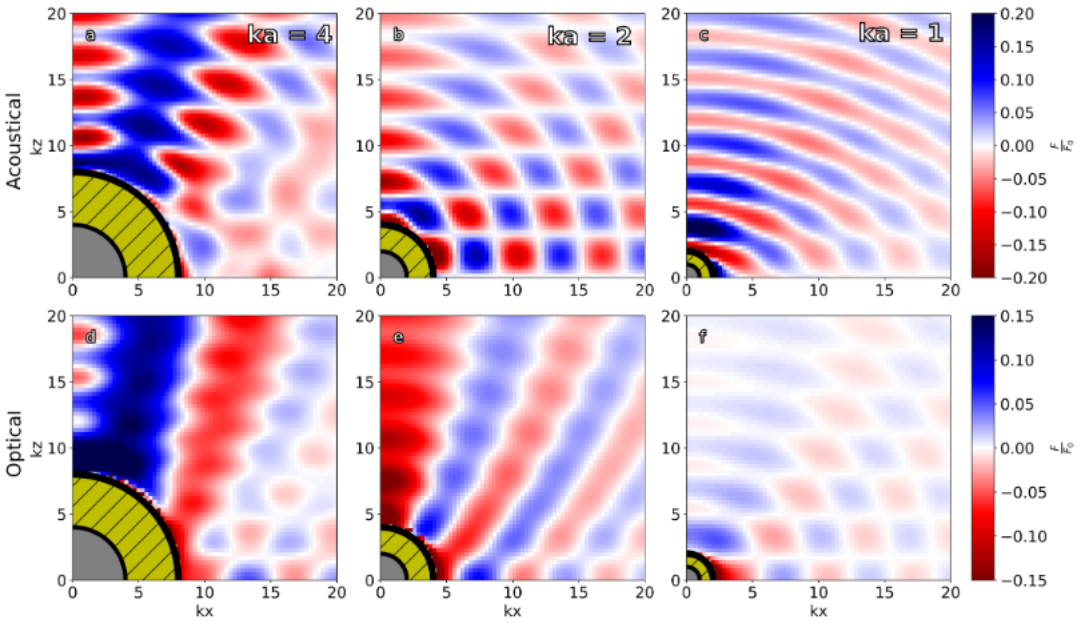

Figure 3.13: Radial force maps. Acoustic two-body force maps for **(a)** $ka = 4$, **(b)** $ka = 2$, and **(c)** $ka = 1$ particles. Optical binding forces compared for **(d)** $ka = 4$, **(e)** $ka = 2$, and **(f)** $ka = 1$ particles.

sizes **Fig. 3.13**. The calculation of the force maps for optical binding was done using traditional CDM methods while the force maps for acoustic binding was achieved using MFS. In both the acoustic and optical binding force maps, particles are placed into a counter-propagating standing wave. Furthermore, the fields are propagating along the $\hat{\boldsymbol{z}}$ direction. In comparing both cases, we observe similarities which include oscillatory behaviors in lateral and longitudinal directions.

One of the major differences between the two forces is that optical binding is generated by a vector field and acoustic binding is generated by a scalar field. Despite the similarities in **Fig. 3.13**, I also note that the acoustic binding was computed on spheres which satisfied a 'sound-hard' condition. This condition is a good approximation for solid spheres in air. This condition states that the field does not penetrate the spheres and translates more directly to a conducting sphere in optical binding.

The ability to use MFS for acoustic binding allows us to gain insight on the dynamic capabilities of field-driven self-assembled systems. One of the most in-

teresting results of the computational study was the discovery of driven clusters. Similar to what was able to be observed with optical binding, we found the self-organization of particles into drifting and rotating structures. This study was limited to small clusters ($N = 5$); however the use of a MFS based simulation allowed us to generate and classify an assortment of colloidal clusters which exhibited a variety of active behaviors. Like the similarities in the static force maps between acoustic and optical binding, we also find both forces have the capability to generate active behaviors in materials. The MFS results for acoustic binding showed the formation of particle clusters which exhibit drifting equilibrium states as well as rotational motion. Although acoustic binding it is clearly a different phenomenon than optical binding, the computational results seemed to overlap with the many-body and non-conservative effects which we were simultaneously attempting to address with optical binding. Using MFS for acoustic binding gave us a window to further understand the behaviors we were seeing in experiments. Furthermore, once we were able to develop the CDM based dynamic simulations, we directly found comparable formations of active clusters as those reported by Clair et. al. [42]. This study highlights dynamics that are inherent in systems driven by field scattering and provides motivation to develop MFS methods for optical binding.

3.10 Dielectric Sphere (MFS)

Electromagnetic scattering from dielectric objects can be approximated using MFS methods [43]. This section addresses a single dielectric sphere in a plane wave, and thus should serve only as a first step approach towards an optical binding solution. In this section I share how the problem can be formulated in theory but further development remains out of scope for this thesis.

Starting with an electromagnetic plane wave in medium:

$$\boldsymbol{E} = E_0 e^{ik^+ r_z} \hat{\boldsymbol{x}} \tag{3.13}$$

propagating through a sphere of radius, a. The field scattered by the sphere can

be determined by a sum of fundamental solutions:

$$\boldsymbol{E}^s(r) = \sum_j^N \overleftrightarrow{\boldsymbol{G}}^+(r, r_j^+) \cdot \boldsymbol{c_j} \tag{3.14}$$

while the field inside of the sphere is

$$\boldsymbol{E}^-(r) = \sum_j^N \overleftrightarrow{\boldsymbol{G}}^-(r, r_j^-) \cdot \boldsymbol{d_j} \tag{3.15}$$

with the dyadic Green's function $\overleftrightarrow{\boldsymbol{G}}$. $\boldsymbol{c_j}$ and $\boldsymbol{d_j}$ are constant vector quantities which remain to be solved. $r_j^{\pm}$ are the locations of N source points which are located outside of the domain being evaluated. Thus r_j^+ are all placed inside of the sphere and r_j^- are placed outside of the sphere.

In order to solve for the unknown vectors known conditions at the surface of the sphere can be used. Primarily,

$$\hat{\boldsymbol{n}} \times \boldsymbol{E}^s(r) - \hat{\boldsymbol{n}} \times \boldsymbol{E}^-(r) = \boldsymbol{f}(r) \tag{3.16}$$

$$\hat{\boldsymbol{n}} \times (\boldsymbol{\nabla} \times \boldsymbol{E}^s(r)) - \frac{\epsilon^- k^{-2}}{\epsilon^+ k^{+2}} \hat{\boldsymbol{n}} \times (\boldsymbol{\nabla} \times \boldsymbol{E}^-(r)) = \boldsymbol{F}(r) \tag{3.17}$$

$\epsilon^{\pm}$ represents the dielectric constant of the material outside (+) and inside (-) the sphere boundary. By combining **Eq. 3.14**,**Eq. 3.15** and **Eq. 3.16**,**Eq. 3.17**, we can also write that

$$\sum_j^N (\hat{\boldsymbol{n}} \times \overleftrightarrow{\boldsymbol{G}}^+(r, r_j^+) \cdot \boldsymbol{c}_j - \hat{\boldsymbol{n}} \times \overleftrightarrow{\boldsymbol{G}}^-(r, r_j^-) \cdot \boldsymbol{d}_j) = \boldsymbol{f}(r) \tag{3.18}$$

$$\sum_j^N (\hat{\boldsymbol{n}} \times (\boldsymbol{\nabla} \times \overleftrightarrow{\boldsymbol{G}}^+(r, r_j^+) \cdot \boldsymbol{c}_j - \frac{\epsilon^- k^{-2}}{\epsilon^+ k^{+2}} \hat{\boldsymbol{n}} \times (\boldsymbol{\nabla} \times \overleftrightarrow{\boldsymbol{G}}^-(r, r_j^-) \cdot \boldsymbol{d}_j) = \boldsymbol{F}(r) \tag{3.19}$$

By evaluating at $r_i, i = 1..M$ evaluation points on the sphere, an approximation can be determined as long as $M = N$. **Eq. 3.18** and **Eq. 3.19** could then be solved as a system of linear equations. Applying this technique to multiple objects would require updating the sum to include scattering contributions of the source points located inside the other particles.

This method can be utilized for non-spherical objects and be easily adapted to study metallic objects as well. Although the methods are slightly more complex,

the ability to obtain the scattered field with less source points than DDA is a great benefit to computational cost. Currently computational cost is the biggest obstacle to studying larger many-body systems. The biggest difference between DDA and MFS is that the scattering units must be placed throughout the entire volume of the object for DDA while MFS requires only scatterers near the surface. This remains a proposed method for electromagnetic scattering.

3.11 Summary

The next steps in optical binding are going to depend on a combination of experimental observations and computational analysis. What I have shown in this chapter is that there is a large configuration space for optical binding. Where you are in this space, whether it be inter-particle orientation, distance, or particle size, particle refractive index can strongly effect the dynamics of the system. I also showed that the dynamics of these optical binding systems can be highly active. To understand these effects more generally, and to provide a guide for future experimental systems, a good computational tool for molecular dynamics must be developed.

In **§3.5**, I present such a tool by integrating DDA code to a molecular dynamics type simulation. Furthermore, I show how the capability to include thermal noise can return results that are aligned with observations. For feasible use of this model for larger particles, we remain limited to $N < 10$ particles. Despite this limitation, we were already able to find evidence of self-organization into driven clusters of just three particles. This result shows us that the current model can already help us map out when we should expect strong active effects in experiments. Furthermore, by simply controlling the thermal noise we can begin to understand the various mechanisms.

Finally I proposed a method which can be utilized to move the model closer towards assessing larger systems. I discussed how this method shows promising results for the acoustic equivalent of optical binding. Surprisingly, we find that acoustic and optical binding are both very similar and both exhibit active clus-

tering. Assessing these features, particularly in much bigger groups are the next stages with dynamic modeling of these systems. This chapter is meant to serve as the first steps towards that goal.

Chapter 4

Conclusion

The work presented in this thesis explored the optical binding forces as a self-organizing tool for colloidal matter. I sought to learn what optically bound structures could be built and how would these structures behave. In **Chapter 1**, I analyzed scattering and gradient forces, which are in some combination inherently present in optical binding, and showed not only that their relative strengths can play a role in self-organization behaviors but also that they can be tuned by altering parameters specific to the optical and physical properties of the colloids, field, and surrounding medium. I show that the scattering force which is generally weaker for small particles dominates for larger particles and higher relative refractive indices. Additionally, I aimed to highlight how important inter-particle orientation is. I show that the force is analytically different depending on lateral and longitudinal displacements. I also show that longitudinal optical binding forces tend to be more sensitive to changes in particle size.

In **Chapter 2**, with the design of a novel experimental apparatus, we observed the interaction of particles. While previous studies focused on lateral or longitudinal configurations: our design allowed us to observe particles in 3-dimensions interacting in both orientations simultaneously. This effort allowed us to observe new self-organization behaviors including the formation of multiple colloidal chains, multiple rods, and multiple active clusters. By comparing high-index and low-index particles I presented a detailed analysis which correlated scattering strength

to high activity dynamic behaviors as well as correlated activity with the formation of high-density particle clusters. Using numerical simulations of optical binding forces, I additionally show that non-pairwise effects can drive particle clustering and that asymmetric particle clustering can generate non-conservative and non-reciprocal interactions.

Finally, in **Chapter 3** I used numerical simulations to understand where non-pairwise forces come from and what types of effects they can have. I showed that multiple-scattering becomes non-negligible when larger higher-index particles interact through scattering. For a system of three particles, I measured the three-body force and show that, in the longitudinal orientation, it can fundamentally change the binding interaction. For a more generalized measure, I also looked at the error associated with making a two-body approximation for a range of particle sizes. This analysis, showed that the two-body forces were much less accurate as particle sizes increase and that the difference is highly dependent on the specific orientation of the system. As for more dynamic information, we developed a model for optical binding which couples scattering code with a molecular dynamics simulation. We used this code to generate two-body optical binding interactions which include thermodynamic fluctuations. Furthermore, we used this code to analyze active clusters. We found in the lateral configuration, three-body optically bound systems can form a large number of stable structures and that some of these structures exhibit high activity after formation. We find that formation of active clusters is more common for larger high-index particles, which agrees with our experimental findings.

The next steps in this work is to assess how to gain more control over the optical binding experiments. What we uncovered in this thesis is that optically bound self-organization is an extremely sensitive and leads to unexpected behavior. While this is generally good news for generating complex behaviors, we really need to prove that we can eventually use tools to design the structures that we want. This may include tools which can enhance or reduce particle clustering for instance. Our work suggests that removing particle clustering may enhance stability.

Future steps may also include generating different active systems. I showed

that certain clusters and orientations could lead to collective linear and rotational motions. If there was a way, possibly through functionalizing particle surfaces, to lock particles into specific configurations, it could be possible to generate an entire system of active optically bound objects.

As the systems we study become increasingly more complex and larger in scale, the next steps in the study of optical binding would also include the optimization of computational methods. So far, numerical analysis is the only practical method to untangle the observed behaviors and to make predictions of self-organization. In this thesis, although we relied heavily on the Coupled Dipole Method to understand what we were observing, we propose the use of the method of fundamental solutions as an eventual replacement. In this case, the benefit is the promise of utilizing less scattering points, which can have a huge impact of the total number of particles that can be simulated. So far, studying > 10 large particles is unfeasible in our current development, which currently does not allow us to fully simulate the many-particle systems which we have focused on experimentally.

While there remains a lot of future work to be done in characterizing optical binding forces, I hope that the work in this thesis can serve as a guide for how to think about inter-particle forces driven by field scattering. Undoubtedly, I shared the rich complexity which can be involved with such interactions: directional, multi-stable, non-conservative, non-pairwise, and non-linear. While it is this complexity which makes optical binding so difficult to study, it is the same complexity which makes it so *worth* studying. The ability to harness and manipulate these various aspects of optical binding forces could ultimately help us design new static and dynamic materials.

Bibliography

[1] Michael M. Burns, Jean-Marc Fournier, and Jene A. Golovchenko. Optical binding. *Physical Review Letters*, 63(12):1233–1236, September 1989.

[2] A. Ashkin, J. M. Dziedzic, J. E. Bjorkholm, and Steven Chu. Observation of a single-beam gradient force optical trap for dielectric particles. *Optics Letters*, 11(5):288–290, May 1986.

[3] T. Thirunamachandran. Intermolecular interactions in the presence of an intense radiation field. *Molecular Physics*, 40(2):393–399, June 1980.

[4] Wolfgang Singer, Manfred Frick, Stefan Bernet, and Monika Ritsch-Marte. Self-organized array of regularly spaced microbeads in a fiber-optical trap. *JOSA B*, 20(7):1568–1574, July 2003.

[5] V. Karásek, T. Čižmár, O. Brzobohatý, P. Zemánek, V. Garcés-Chávez, and K. Dholakia. Long-Range One-Dimensional Longitudinal Optical Binding. *Physical Review Letters*, 101(14):143601, October 2008.

[6] Xiao Li, Hongxia Zheng, Chi Hong Yuen, Junjie Du, Jun Chen, Zhifang Lin, and Jack Ng. Quantitative study of conservative gradient force and non-conservative scattering force exerted on a spherical particle in optical tweezers. *Optics Express*, 29(16):25377, August 2021.

[7] Craig F. Bohren and Donald R. Huffman. *Absorption and Scattering of Light by Small Particles*. Wiley, 1 edition, April 1998.

[8] Xiao Li, Yineng Liu, Zhifang Lin, Jack Ng, and C. T. Chan. Non-Hermitian physics for optical manipulation uncovers inherent instability of large clusters. *Nature Communications*, 12(1):6597, November 2021.

[9] Kayn A. Forbes, David S. Bradshaw, and David L. Andrews. Optical binding of nanoparticles. *Nanophotonics*, 9(1):1–17, January 2020.

[10] Jack Ng, Z. F. Lin, C. T. Chan, and Ping Sheng. Photonic clusters formed by dielectric microspheres: Numerical simulations. *Physical Review B*, 72(8):085130, August 2005.

[11] Bruce T. Draine and Piotr J. Flatau. Discrete-Dipole Approximation For Scattering Calculations. *JOSA A*, 11(4):1491–1499, April 1994.

[12] A. G. Hoekstra, M. Frijlink, L. B. F. M. Waters, and P. M. A. Sloot. Radiation forces in the discrete-dipole approximation. *JOSA A*, 18(8):1944–1953, August 2001.

[13] Colin Robert McInnes. Solar radiation pressure. In Colin Robert McInnes, editor, *Solar Sailing: Technology, Dynamics and Mission Applications*, Astronomy and Planetary Sciences, pages 32–55. Springer, London, 1999.

[14] James Clerk Maxwell. *A Treatise on Electricity and Magnetism*. Clarendon, 1904. Google-Books-ID: t5vCDCXPUswC.

[15] E. F. Nichols and G. F. Hull. The Pressure Due to Radiation. (Second Paper.). *Physical Review (Series I)*, 17(1):26–50, July 1903.

[16] A. Ashkin. Acceleration and Trapping of Particles by Radiation Pressure. *Physical Review Letters*, 24(4):156–159, January 1970.

[17] Jeffrey R. Moffitt, Yann R. Chemla, Steven B. Smith, and Carlos Bustamante. Recent Advances in Optical Tweezers. *Annual Review of Biochemistry*, 77(1):205–228, June 2008.

[18] Furqan M Fazal and Steven M Block. Optical tweezers study life under tension. *Nature Photonics*, 5(6):318–321, June 2011.

[19] David J. Griffiths. *Introduction to Electrodynamics*. Cambridge University Press, 4 edition, June 2017.

[20] Edward M. Purcell and Carlton R. Pennypacker. Scattering and Absorption of Light by Nonspherical Dielectric Grains. *The Astrophysical Journal*, 186:705, December 1973.

[21] Stefano Sacanna, Mark Korpics, Kelvin Rodriguez, Laura Colón-Meléndez, Seung-Hyun Kim, David J. Pine, and Gi-Ra Yi. Shaping colloids for self-assembly. *Nature Communications*, 4(1):1688, June 2013.

[22] Kishan Dholakia and Pavel Zemánek. Colloquium: Gripped by light: Optical binding. *Reviews of Modern Physics*, 82(2):1767–1791, June 2010.

[23] Yasahiro Harada and Toshimitsu Asakura. Radiation forces on a dielectric sphere in the Rayleigh scattering regime. *Optics Communications*, 124(5-6):529–541, March 1996.

[24] Yongmin Liu and Xiang Zhang. Metamaterials: a new frontier of science and technology. *Chemical Society Reviews*, 40(5):2494, 2011.

[25] Christopher D. Mellor, Thomas A. Fennerty, and Colin D. Bain. Polarization effects in optically bound particle arrays. *Optics Express*, 14(21):10079–10088, October 2006.

[26] S. A. Tatarkova, A. E. Carruthers, and K. Dholakia. One-Dimensional Optically Bound Arrays of Microscopic Particles. *Physical Review Letters*, 89(28):283901, December 2002.

[27] Patrick McCormack, Fei Han, and Zijie Yan. Self-Organization of Metal Nanoparticles in Light: Electrodynamics–Molecular Dynamics Simulations and Optical Binding Experiments. *The Journal of Physical Chemistry Letters*, 9(3):545–549, February 2018.

[28] Fan Nan and Zijie Yan. Light-Driven Self-Healing of Nanoparticle-Based Metamolecules. *Angewandte Chemie International Edition*, 58(15):4917–4922, April 2019.

[29] V. Garcés-Chávez, K. Dholakia, and G. C. Spalding. Extended-area optically induced organization of microparticles on a surface. *Applied Physics Letters*, 86(3):031106, January 2005.

[30] Oto Brzobohatý, Lukáš Chvátal, Martin Šiler, and Pavel Zemánek. Complex colloidal structures with non-linear optical properties formed in an optical trap. *Optics Express*, 28(25):37700, December 2020.

[31] Dominique J. Davenport and Dustin Kleckner. Formation of colloidal chains and driven clusters with optical binding. *Soft Matter*, 18(23):4464–4474, 2022.

[32] Xiaoning Zhang, Jun Qiu, Jun Qiu, Jun Qiu, Xingcan Li, Xingcan Li, Junming Zhao, Junming Zhao, Linhua Liu, and Linhua Liu. Complex refractive indices measurements of polymers in visible and near-infrared bands. *Applied Optics*, 59(8):2337–2344, March 2020.

[33] G. M. Hale and M. R. Querry. Optical Constants of Water in the 200-nm to 200-microm Wavelength Region. *Applied Optics*, 12(3):555–563, March 1973.

[34] I. H. Malitson. Interspecimen Comparison of the Refractive Index of Fused Silica*,†. *JOSA*, 55(10):1205–1209, October 1965.

[35] John C. Crocker and David G. Grier. Methods of Digital Video Microscopy for Colloidal Studies. *Journal of Colloid and Interface Science*, 179(1):298–310, April 1996.

[36] Dan Allan, Thomas Caswell, Nathan Keim, and Casper van der Wel. trackpy: Trackpy v0.3.0, November 2015.

[37] V. Karásek, K. Dholakia, and P. Zemánek. Analysis of optical binding in one dimension. *Applied Physics B*, 84(1):149–156, July 2006.

[38] Justo Rodríguez, Luciana C. Dávila Romero, and David L. Andrews. Optical binding in nanoparticle assembly: Potential energy landscapes. *Physical Review A*, 78(4):043805, October 2008.

[39] D.M. Heyes and J.R. Melrose. Brownian dynamics simulations of model hard-sphere suspensions. *Journal of Non-Newtonian Fluid Mechanics*, 46(1):1–28, January 1993.

[40] V Karásek, O Brzobohatý, and P Zemánek. Longitudinal optical binding of several spherical particles studied by the coupled dipole method. *Journal of Optics A: Pure and Applied Optics*, 11(3):034009, March 2009.

[41] Graeme Fairweather, Andreas Karageorghis, and P.A. Martin. The method of fundamental solutions for scattering and radiation problems. *Engineering Analysis with Boundary Elements*, 27(7):759–769, July 2003.

[42] Nicholas St. Clair, Dominique Davenport, Arnold D. Kim, and Dustin Kleckner. Dynamics of Acoustically Bound Particles. 2021.

[43] E. S. Athanasiadou and I. Arkoudis. The method of fundamental solutions for scattering of electromagnetic waves by a chiral object. *Applicable Analysis*, pages 1–20, March 2022.